Application of electrical fields on textile-reinforced mortar interlayers for leakage detection and prevention of chloride-induced corrosion damages

Von der Fakultät für Bauingenieurwesen der
Rheinisch-Westfälischen Technischen Hochschule Aachen
zur Erlangung des akademischen Grades einer Doktorin der Ingenieurwissenschaften
genehmigte Dissertation

vorgelegt von

Carla Driessen-Ohlenforst, geb. Driessen

Berichter: Universitätsprofessor Dr.-Ing. Michael Raupach
Universitätsprofessor Dr.-Ing. Wolfgang Breit

Tag der mündlichen Prüfung: 13.05.2022

Preface

This doctoral thesis is submitted to the RWTH Aachen University for the degree of Dr.-Ing. (Doctor of Engineering). The research was conducted at the Institute of Building Materials Research (ibac) in Aachen, Germany. The supervisor of the thesis has been Professor Michael Raupach.

The research project “Konzeptionierung und Validierung des Monitoring- und pKKS-Systems für SMART-DECK” for the framework of this Ph.D. thesis started in September 2014, and the thesis was submitted in 2022. The BMBF sponsored the project, and the project executing organization was “VDI Technologiezentrum GmbH (VDITZ)”. The thesis consists of an extended summary, the description of the theoretical background, four appended papers (three published in international scientific journals, one published in a book series with selected papers from an international RILEM Ph.D. Workshop) and an overall discussion of the results as well as an outlook.
The author, Carla Driessen-Ohlenforst, declares that the thesis and the work presented in it are her own and have been generated by her as the result of original research while in candidature for the degree of Dr.-Ing. at RWTH Aachen University. The thesis contains no material previously submitted for a degree at this university or any other institution.

Carla Driessen-Ohlenforst

Acknowledgment

First, I would like to thank Professor Michael Raupach for giving me the chance to write this thesis and always taking the time for discussions helping with his expertise and ideas on the research topics and the textual preparation. I also want to thank him for the open working atmosphere in the institute and the numerous opportunities for conferences and papers.
I would also like to thank Prof. Dr.-Ing. Wolfgang Breit for reviewing this thesis.

Many thanks go to all my colleagues at the Institute of Building Materials Research for the outstanding good working atmosphere and the professional and personal conversations and time spent together. Mainly I want to thank Dr. Christian Helm, the head of my working group, for always having advice and his contagious dedication to the topic. Special thanks go to Markus Zander and all the student assistants without whom the laboratory work would not have been possible. Also, many thanks to Winfried Keutgen for developing the measuring technique and Dr. Joachim Hannawald for the theoretical support regarding the modelling approaches.

Finally, I want to thank my family and friends for the encouragement in my work and the diversion in the hours without. Especially my parents for their belief in me, the opportunity to always follow my interests, and their support in every way. I want to thank my husband Markus for his support from the beginning of my studies to the writing of this thesis and my daughter Lilia for the sweetest diversion.

Summary

The service life of bridges is often threatened by an insufficient shear force capacity in the transverse direction and by leakages in the sealing layer, which lead to chloride ingress and, therefore, corrosion damages. A thin, multifunctional interlayer of textile reinforced concrete called SMART-DECK was developed to prevent expensive repair work and traffic obstructions. This interlayer provides four functions: full-surface moisture monitoring in real-time, a chloride barrier, preventive cathodic corrosion protection, and increased shear force capacity. If leakage occurs, the cathodic corrosion protection can be switched on to protect the reinforcement from corrosion damage. The renewing of the damaged bridge deck sealing must not be carried out immediately but can be postponed over the years, e.g., to periods with little traffic. Large-scale humidity monitoring is implemented by measuring the electrolytic resistance between two carbon meshes embedded in mortar. The electrolyte resistance is measured using an alternating current. Decreasing values in the measured electrolyte resistance indicate water ingress through leakages in a surface-applied membrane. Through numerical simulations, the theoretical size of a detectable leakage area is calculated, which depends on the geometry of the leakages, the electrolyte resistance of the mortar in wet and dry conditions, the position of the leakage, and other boundary conditions. If leakage is detected, an electrical field between the carbon meshes is built, called the “electrochemical chloride barrier” and suppresses the ingress of chlorides into the concrete. The negatively charged chloride ions are held on the upper carbon mesh that is polarized as an anode to prevent chloride-induced corrosion on the reinforcement. The question of which voltages and electrical field strengths are necessary to avoid critical chloride contents at the reinforcing steel is investigated. Laboratory tests showed that even voltages of fewer than 2 Volts reduce chloride ions behind the anode compared to reference probes. Furthermore, an unexpected effect was observed: higher voltages increase chloride ions again after passing a local minimum for specific depths of the reference probes. Analytical and numerical investigations elucidate this effect and, since the destructing test method in the laboratory did not allow research of the time dependency, determine its behavior and the overall behavior of the chloride concentration in the probes over time. It has been investigated whether the voltages to implement an electrochemical chloride barrier are smaller than they have to be for joint preventive cathodic protection. One advantage of this chloride barrier is that the anodic polarization of the carbon meshes can be reduced due to the lower current densities. Different voltages, electrical field strengths, anode materials, and anode arrangements were investigated.

I. Table of Contents

II. List of Papers

This thesis includes four published papers. The papers are listed below and inserted in chapters 4-6.

I) Driessen, C.; Raupach, M.: Numerical Simulation for the Detection of Leakages in Bridge Deck Membranes Through Resistivity Measurements. Cham: Springer, 2019. - In Service Life and Durability of Reinforced Concrete. Selected Papers of the 8th International RILEM Ph.D. Workshop, Marne-la-Vallee, France, September 21.-27, 2016, (Andrade, C.; Gulikers, J.; Marie-Victoire, E. (Eds.)), S. 57-69 ISBN 978-3-319-90235-7

II) Driessen-Ohlenforst, C.: SMART-DECK: Multifunctional Carbon-Reinforced Concrete Interlayer for Bridges. Dedicated to Professor Dr.-Ing. Michael Raupach on the Occasion of his 60th Birthday. In: Materials and Corrosion 71 (2020), Nr. 5, S. 786-796

III) Carla Driessen-Ohlenforst, Michael Raupach: Application of electrical fields to reduce chloride ingress into concrete structures, Magazine of Concrete Research, Volume 74, pp. 1–27 Published online: November 22, 2021 https://doi.org/10.1680/jmacr.21.00020

IV) Carla Driessen-Ohlenforst, Michael Raupach: Analytical and Numerical Investigation of an Electrochemical Chloride Barrier for Reinforced Concrete Structures. Academic Editor: Alessandro P. Fantilli, Materials 2021, 14(21), 6728; https://doi.org/10.3390/ma14216728, Received: 5 October 2021 / Revised: 1 November 2021 / Accepted: 4 November 2021 / Published: 8 November 2021 (This article belongs to the Special Issue Reinforced Concrete Structures for Durability and Corrosion Resistance)

III. List of Figures and Tables

Tables

IV. List of Symbols and Abbreviations

Symbol	Unit	Description
A	m²	Cross-sectional area of the mortar specimen
b	K	Temperature coefficient
B	m²	Area of the core face
C	F	Capacitance
c	mol/m3	Concentration of chloride ions in mortar
c_0	mol/m³	Concentration of chloride ions in NaCl solution
c_i^j	mol/m³	Discretized solution for the concentration
D_{eff}	m²/s	Diffusion coefficient
dt	s	Time increment in solution grid
dx	m	Spatial increment in solution grids
E	V/m	Electrical field strength
E’	V/m	Real component of electrical field strength
E’’	V/m	Imaginary component of electrical field strength
F	(A*s)/mol	Faraday constant
f	Hz	Ordinary frequency
f_{net}	-	Fitting factor for the migration speed
h	m	Film coefficient
i	A/m²	Current density
I	A	Current
I’	Vs/m²	Real component of magnetic field
I’’	Vs/m²	Imaginary component of magnetic field
J	mol/(m²s)	Molecular flow
$J`_c$	kg/(m²s)	Convective flux of chloride ions
J_m	m/s	Flux of moisture in concrete
k	m	Geometry factor
L	m or H	Length or Inductance
L_{net1}	m	Depth of the first net of the E-field
L_{net2}	m	Depth of the second net of the E-field
m	kg	Mass

M	kg/mol	Molar mass
R	J/(mol*K)	Gas constant
R_{el}	Ω	Electrolytic resistance
$R_{measured}$	Ω	Resistance between the plates
$R_{p,A}$	Ω	Polarization resistance of the anode
$R_{p,C}$	Ω	Polarization resistance of the cathode
σ	1/Ω	Electrical conductivity
t	s	Time
T	K	Absolute temperature
u	M.-%	Moisture content referred to the mass of mortar
U	V	Potential difference
U_{Inst}	V	Instant-Off-Potential
u_m	m/s	Average mass-related speed
U_{On}	V	On-Potential
V	V	Potential
v_{eff}	m/s	Effective speed of the NaCl ions
x	m	Position along the depth of the probe
z	-	Ion valence
Z	Ω	Impedance
Z'	Ω	Real component of impedance
Z''	Ω	Imaginary component of impedance
ε_0	-	Electrical field constant
ε_r	-	Relative permittivity
ρ	Ωm	Resistivity
ϕ	V	Electrical potential
ω	rad/s	Radial frequency

Abbreviation	**Description**
AC	Alternating Current
AC/DC	Alternating Current / Direct Current
AR	Alkali-Resistant
CFRP	Carbon-Fibre-Reinforced Polymer

CP	Cathodic Protection
ECE	Electro-chemical Chloride Extraction
EIS	Electrochemical Impedance Spectroscopy
FEM	Finite Element Method
ICCP	Impressed Current Cathodic Protection
IR	Current-Resistance
ISO	International Standardiziation Organization
MMO	Mixed Metal Oxide
NHE	Normal Hydrogen Electrode
SBR	Styrene-Butadiene Rubber
SEM	Scanning Electron Microscope
TRC	Textile Reinforced Concrete

1 Introduction

1.1 Motivation

The maintenance and repair of (reinforced) concrete structures lead to great economic and structural efforts worldwide. The maintenance costs over all buildings can be estimated to be about 20 billion $ per year, with a considerable part of these costs spent on concrete structures. (Raupach et al., 2006) Especially infrastructure buildings like bridges are threatened by corrosion damages due to chloride ingress and lead to high maintenance costs. The damages are often detected at first when already a high degree of damage is reached due to the temporal intervals of bridge inspections and the existing monitoring options, which work only discretely at the point of installation. (Raupach et al., 2013) Monitoring a complete construction would need many sensors, which is not an economical solution.

Nowadays, it is not common to use systems for cathodic corrosion protection on lanes and bridges because of cost concerns: primarily because the sealing has to be removed to install the anodes and the established impressed current anodes are expensive. In the context of a research project, a thin carbon-reinforced mortar interlayer was developed, which provides four functions: an all-over real-time humidity monitoring, a chloride barrier, preventive cathodic corrosion protection, and strengthening reinforcement of bridges with an insufficient load-bearing capacity. This work focuses on the first, second, and third functions. The interlayer consists of a newly developed mortar and two layers of carbon textile reinforcement. Between those layers, the electrical resistivity is measured. When the sealing starts to leak, and water permeates into the interlayer, a drop in the measured electrical resistivity is detected in real-time. All relevant data are transmitted via the internet and are presented in a simple form e.g., in a color scheme, to show the sealing condition. When damage in the sealing is detected, the electrochemical chloride barrier can be switched on. The upper carbon layer is polarized as an anode that holds the negatively charged chloride ions. Thus the maintenance measures of the bridge deck sealing can be postponed to periods with less traffic or to that point of time when a renewing of the sealing is planned anyway. (Driessen & Raupach, 2015a)

This work has two primary intentions. Firstly, the question under which boundary conditions and with which material components full-surface monitoring of intruding water is possible should be answered. Secondly, it will be shown under which circumstances the knowledge drawn from the full-surface monitoring can help to implement an electrochemical chloride barrier so that the ingress of chlorides into the concrete to the reinforcement can be prevented in the first place.

1.2 State of the Art and Need for Research

Regarding the full surface moisture monitoring, it has to be emphasized that monitoring a full surface in real-time using alternating current between two technical carbon layers in mortar is a completely new concept. For example, for a sensor monitoring the humidity distribution of the concrete, the Multiring-Electrode can be named. It measures the distribution of the electrical resistivity of the concrete, which can be converted to water-content profiles after calibration with the concrete. (Raupach et al., 2013) This allows to evaluate possible corrosion rates of different types of corrosion, especially the corrosion rate, which is directly dependent on the electrical resistance of the concrete. (Warkus & Raupach, 2010) As for the Multiring-Electrodes for the full-surface monitoring, it is necessary to examine the properties of the mortar relating to electrical resistivity and humidity to develop a well-working monitoring system. To receive a finely graduated humidity monitoring, the mortar must have a high sensitivity for humidity, which means that the mortar should have a wide range in resistivity values at different points of moisture content. To reach these objectives, a suitable pore structure has to be found. (Driessen & Raupach, 2015b)

In this context, capillary pores with low constrictivity and tortuosity could help to achieve the intended properties. (Reichling et al., 2012) Another challenge in measuring a greater surface is the influence of the leakage position in the measuring field on the measured resistivity drop. For questions like this, numerical simulations provide a good option.

Although cathodic protection is often used nowadays and specified in an ISO standard (*DIN EN ISO 12696*, o. J.), the opportunity to start the protection at the moment of the possible threat caused by intruding chloride-contaminated water is new due to the full-surface monitoring. So, the question will be solved whether commonly used voltages for cathodic prevention are sufficient or can even be reduced if the aim is to prevent chloride ingress from the beginning so that an electrochemical chloride barrier is implemented. By now, other scientific investigations focus on protecting the steel despite chlorides or removing chlorides already in the concrete. (Eichler et al., 2010) Therefore, usually, voltages of a minimum of 2 Volts are used. Additionally, the method of Electrochemical Chloride Extraction (ECE) has to be differentiated from the intended function in this work. First, higher voltages are standard for electrochemical chloride extraction, and lower voltage ranges are usually not examined. Furthermore, the chloride ions are already in the concrete. Last, it has to be mentioned that due to the anode system, which is placed on top of the structure, the migration direction is unidirectional from the steel to the anode system, whereas in the case of the electrochemical barrier, the flux direction changes in the structure for different regarded areas.

So, in this work, different approaches are used to investigate the balance of forces between diffusion, migration, and convection of the intruding chlorides.

2 Theoretical Background

This chapter briefly describes the theoretical backgrounds necessary for the investigations regarding the full-surface monitoring and the electrochemical chloride barrier.

2.1 Corrosion of Steel in Concrete

In the alkaline pore solution of concrete with Ph-values of 12.5 to 13.5, the steel reinforcement forms an ultrathin (<10 nm) protective iron oxide (Fe_3O_4/Fe_2O_3) or -if exposed to air-hydroxide ($Fe(OH)_3$) film. This passive layer decreases the dissolution rate of steel to negligible levels. (Poursaee, 2016)

Only after a local loss of this passive layer, the depassivation, either due to the loss of the alkaline environment through carbonation or due to intruding chlorides, the corrosion of steel in concrete is possible. In the case of chloride-induced corrosion, usually, galvanic cells are formed.

Chloride-induced Corrosion

Nowadays, mainly deicing salts and marine salts are the primary sources of chlorides threatening the reinforcement. Chlorides destroy the passive layer locally. The number of chlorides necessary for the deterioration of the passive layer is still discussed. It is supposed to be in a range of 0.1 % to 2.1 % by mass of binder. (Deutscher Ausschuss für Stahlbeton e. V., 2015; Kosalla, 2018)

Areas with an affected passive layer (active areas) show a lower electrical potential than passive areas on the steel.

This potential difference leads to the active corrosion with an anodic and a cathodic reaction:

$$\mathrm{Fe} \rightarrow \mathrm{Fe}^{2+} + 2\mathrm{e}^{-} \qquad 2.1$$

$$2\mathrm{e}^{-} + \mathrm{H_2O} + \frac{1}{2}\mathrm{O_2} \rightarrow 2\mathrm{OH}^{-} \qquad 2.2$$

The electrons released at the anode react at the cathode under the consumption of water and oxygen to OH−-ions. The OH−-ions migrate to the anode and complete the galvanic cell. At the anode, the OH−-ions react with Fe2+ to form iron oxides or iron hydroxides, s. Figure 2.1. In the case of chloride-induced corrosion, anode and cathode can be separated even among meters. The corrosion rate usually exceeds the corrosion rate of uniform corrosion due to carbonation and can lead to severe mass loss of the steel. (Kaesche, o. J.)

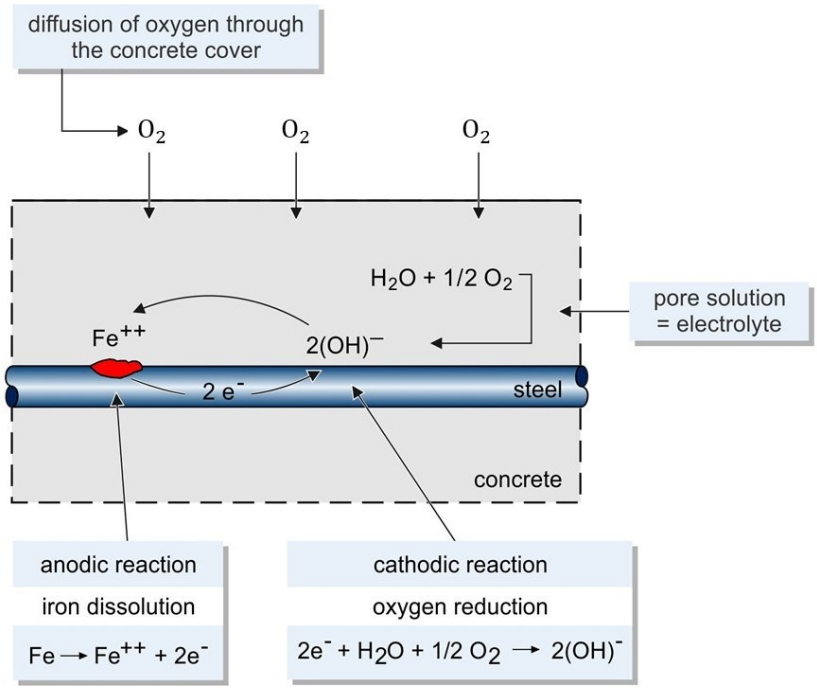

Figure 2.1 Galvanic cell

Further information on the formation of macrocells can be found e.g. in (Raupach, 1992)

The corrosion process can be compared to an electrical circuit, which contains different resistances: first, the electrolytic resistance of the surrounding concrete and then the polarization resistances resulting from the charge transfer between electrolyte and steel. The corrosion current stands in direct relation to the steel mass loss according to Faraday's law, see e.g. (Warkus et al., 2006):

$$m = \frac{M * i * t * A}{z * F} \qquad 2.3$$

With:

- m: Mass loss [kg]
- M: Molar mass [kg/mol]
- i: Current density [A/m^2]
- t: Time [s]
- A: Electrode surface area [m^2]
- z: Valency [–]
- F: Faraday's constant [C/mol]

Taking the mentioned resistances into account, the corrosion current of the macro element can be expressed as:

$$I_{corr} = \frac{U}{R_{p,A} + R_{p,C} + R_{el}} \quad 2.4$$

With:

- I_{corr}: Corrosion current [A]
- U: Driving voltage [V]
- $R_{p,A}$: Polarization resistance of the anode [Ω]
- $R_{p,C}$: Polarization resistance of the cathode [Ω]
- R_{el}: Electrolytic resistance [Ω]

R_{steel}, the resistance of the steel is not taken into account because it is negligibly small. Suppose one of the resistances becomes extremely high. In that case, no significant corrosion rates are possible, e.g., if the concrete is extremely dry, the high electrolytic resistance becomes the controlling factor, see e.g. (Warkus et al., 2006).

2.2 Chloride Ingress into the Concrete

There are different transport mechanisms for chloride ingress into concrete, namely diffusion, migration, and convection with flowing water, accompanied by physical and chemical bonding. (Torres-Luque et al., 2014; Wang et al., 2005)

Chlorides exist in concrete in two different ways: free and bound. It is the common understanding that only free chloride ions in the pore solution in concrete are movable. (Luping et al., 2012)

2.2.1 Chloride Diffusion

Diffusion is the movement of ions under a chemical potential from a high concentration to an area of low concentration. For chloride transport, it has to be mentioned that only free chloride ions in a solution could contribute to chemical potential. (Zeng & Song, 2013)

In the pore system of concrete, the chloride ion transport for non-steady-state conditions can best be described by Fick's Second Law, s. Eq. 2.5. (Bu et al., 2014; Jensen et al., 1999) If other mechanisms are neglected, it predicts the chloride concentration depending on depth and time for a diffusion-controlled transport.

$$\frac{\partial c}{\partial t} = -\frac{\partial J}{\partial x} = -\frac{\partial}{\partial x}\left(D \cdot \frac{\partial c}{\partial x}\right) \quad 2.5$$

Under the assumption of a constant D i.e., a constant chloride-binding capacity, Eq. 2.5 is simplified as a common expression of Fick's second law (Luping et al., 2012):

$$\frac{\partial c}{\partial t} = -\frac{\partial J}{\partial x} = -D \cdot \frac{\partial^2 x}{\partial x^2} \qquad 2.6$$

The diffusion coefficient is not a physical parameter but a system parameter in this case. This parameter shows the mobility or speed of the chloride ions in a medium. For chlorides in water-saturated concrete, the diffusion coefficient is in the magnitude of the order of 1e-12 m²/s. In aqueous solutions, D is about 1e-5 m²/s because the diffusion can take effect in a less porous system. (Zimmermann, 2000)
Luping notes that for non-steady state diffusion, the diffusion coefficient should not be constant but depends on the free chloride concentration. The oversimplification of a constant diffusion coefficient is the main reason for the large range of differences between the diffusion coefficients found in the literature. (Tang, 1996)

2.2.2 Chloride Migration

"Migration is the movement of a charged substance under the action of an electrical field. As in diffusion, only free chloride ions in a solution can contribute to the flow of migration." (Luping et al., 2012)

In the case of an electrical potential gradient, the ions move along a specific direction of the gradient, depending on the valence of the ions, at an average velocity:

$$v = u \cdot \frac{\partial \Phi}{\partial x} \qquad 2.7$$

Where ϕ is the electrical potential and u the ion mobility, which is defined through the Nernst-Einstein-equation and is connected to the diffusion coefficient:

$$u = D \cdot \frac{z \cdot F}{R \cdot T} \qquad 2.8$$

With:

z: Ion valence [-]
F: Faraday constant [(A*s)/mol]
R: Gas constant [J/(mol*K)]

T: Absolute temperature [K]

ϕ: Electrical potential [V]

Accordingly, the flux of chloride ions resulting from an electrical field can be expressed as:

$$J = c * v = c * D * \frac{z * F}{R * T} * \frac{\partial \Phi}{\partial x} \quad 2.9$$

Finally, under the assumption of a constant electrical field.

$$\frac{\partial \Phi}{\partial x} = \frac{U}{L} = E \quad 2.10$$

With:

U: Potential difference [V]

E: Electrical field strength [V/m]

L: Length [m]

the flux becomes (Luping et al., 2012):

$$J = c * v = c * D * \frac{z * F}{R * T} * E \quad 2.11$$

2.2.3 Chloride Convection

Chloride convection is the movement of chloride ions due to the movement of the water in which they are dissolved. While diffusion models describe the transport of chlorides well for water-saturated conditions of the concrete, in cases where the concrete is exposed to wetting and drying of the surface, e.g., reinforced concrete highway structures, the transport of chlorides due to water ingress into concrete also -needs to be taken into account. (Bastidas-Arteaga et al., 2011) Mathematically the transport process can be described by the product of the moisture flux and the chloride concentration

$$J_c = c * J_m \quad 2.12$$

where J_c is the convective flux of chloride ions [kg/m^2·s] and J_m is the flux of moisture in concrete [m/s]. (Martın-Pérez, 1999)

2.2.4 Combined Chloride Transport

The combined transport can be expressed by the Nernst-Planck-equation extended by the convection term (Nikonenko et al., 2009)

$$J = -D \cdot \frac{\partial c}{\partial x} + c * J_m + c * D * \frac{z * F}{R * T} * E \qquad 2.13$$

However, it is hardly possible to use a single equation to describe the complex chloride transport processes in concrete adequately. So, numerical approaches are a better way to model the transport processes of chlorides. (Luping et al., 2012; P. T. Nguyen et al., 2017; Nilsson, 2006)

2.3 Electrochemical Rehabilitation Methods

2.3.1 Cathodic Protection

The first application of cathodic protection applied to concrete structures heavily contaminated with chlorides was mentioned in the late 1950s. (Stratfull, 1957) The application of the technique to protect bridge decks contaminated by deicing salts started in 1973 in North America. (Stratfull, 1974) As soon as suitable hardware like anodes, overlays, reference, and electrodes were developed, in the 1980s, the development of new meshed anodes based on mixed metal oxide activated titanium and the development of carbon-containing paints led to applications such as bridge decks, slabs, marine constructions or garages. (Bertolini et al., 1998)

The main principle behind cathodic protection is a shift of the steel potential in a negative (cathodic) direction to stop the anodic dissolution of iron. This is achieved by rectifier installations or cell formation by contact with sacrificial metals (e.g., sacrificial anodes). (Baeckmann et al., 1997)

In the case of sacrificial/galvanic anodes, the corrosion potential of the anode material is lower than that of the active steel areas. So, the active and passive areas get a cathodic polarization. The potential of active and passive areas aligns, leading to the direct inhibition of the anodic reaction to a reduced corrosion rate. There are two main disadvantages of galvanic protection: they are not adjustable due to the fixed potential difference of the electrode materials and, secondly, the consumption of the anode material, which leads to limited service life. So nowadays, nearly only impressed current anodes are used. The only difference in contrast to galvanic protection is that the anode material not necessarily needs to have lower corrosion potentials than the steel reinforcement but must be stable under anodic polarization. A rectifier

adjusts the required potential difference. In this case, the primary anodic reaction is not a metal dissolution but an oxygen evolution:

$$4\ OH^- \rightarrow 2\ H_2O + O2 + 4e^- \qquad 2.14$$

The most used material for impressed current anodes is the mixed metal oxide (MMO) coated titanium. They can be regarded as inert, and service lifetimes of about 50 to 200 years are mentioned in the literature. (Müller & Holtzhauer, 1992) The latest research investigates the durability of polymer impregnated carbon meshes as anode material which can also be chemically inert in the potential range up to 2200 mV vs. NHE. (Asgharzadeh, 2019) Both materials are often used in the form of meshes. Figure 2.2 gives a schematic impression of cathodic protection (CP) application.

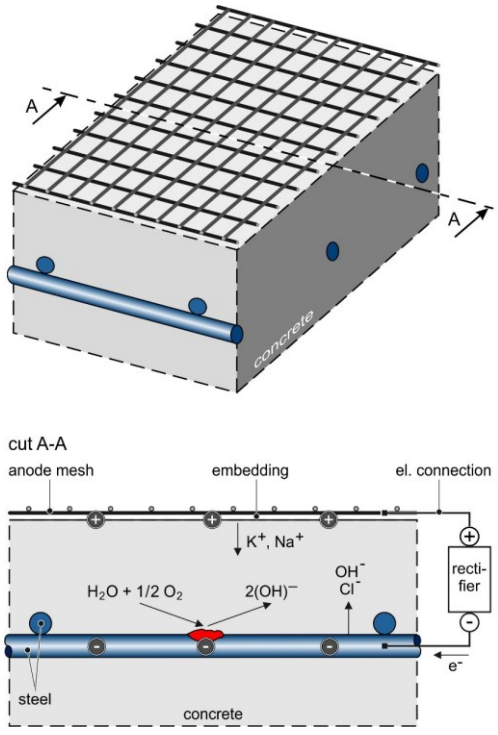

Figure 2.2 cathodic protection of steel in concrete

2.3.2 Cathodic Prevention

In the case of using cathodic protection to new structures, the technique is called cathodic prevention. It is based on the strong influence of the steel potential on the critical chloride content. With current densities in the range from 1 to 2 mA/ m^2, a decrease in the potential of about a minimum of 100-200 mV is achieved, leading to an increase in the critical chloride content, which is higher than one order of magnitude. (Bertolini et al., 1998)

Through the prevention, current hydroxide ions are produced at the steel surface and cause the chloride ions to move toward the anode away from the steel. Cathodic prevention can prevent the initiation of a new pit, but existing pitting can propagate. So cathodic prevention has to be started before corrosion initiates and must be maintained throughout the structure's service lifetime. If pitting corrosion has been initiated, the prevention current is not sufficient anymore, and cathodic protection current would be required, s. Figure 2.3. The application of cathodic prevention for prestressed steel will eliminate the risk of hydrogen evolution because a lower current is required to prevent the initiation of pitting corrosion. (Cheaitani & Laurila, 2012)

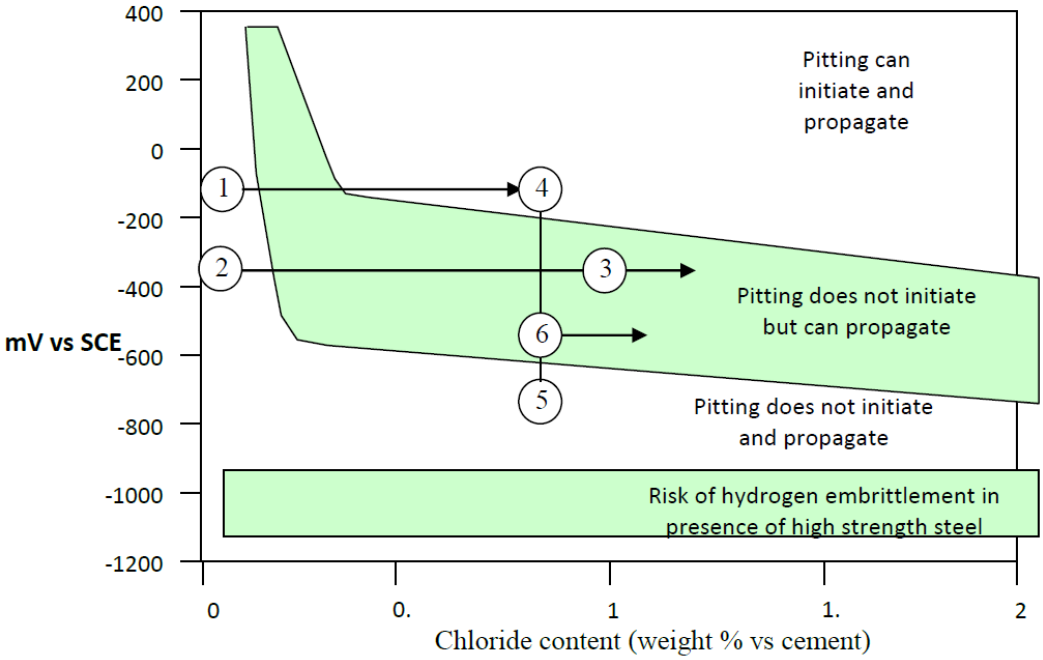

Figure 2.3 Graph showing cathodic prevention: (1→2→3→); cathodic protection restoring passivity (1→4→5→); and cathodic protection reducing corrosion rate (1→4→6→) (Cheaitani & Laurila, 2012; Pedeferri, 1996)

2.3.3 Electrochemical Chloride Extraction

In the case of electrochemical chloride extraction (ECE), a potential gradient is produced by applying a direct current source between the reinforcing steel and an electrode contained in an electrolyte above the concrete cover. (Fajardo et al., 2006; Ihekwaba et al., 1996) An ion-exchange resin in the electrolyte captures the chloride ions before they reach the anode, thus preventing the evolution of chloride gas and minimizing corrosion of the anode. As an anode material, a titanium mesh is used embedded in cellulose material which is soaked with water or another electrolyte. The negatively charged ions such as chloride or hydroxide migrate to the anode, and the positively charged ions like sodium or calcium to the reinforcement. In this

way, the chloride concentration near the reinforcement can be reduced drastically in a relatively short period, usually about a few weeks. After the treatment, the anode and embedding electrolyte material are removed. (Tritthart & Baumgartner, 2007)
The following reactions take place on the Cathode:

$$H_2O + \frac{1}{2}O_2 + 2e^- \rightarrow 2OH^- \quad 2.15$$

$$H_2O + e^- \rightarrow OH^- + H; 2H \rightarrow H_2 \uparrow \quad 2.16$$

Because of the limited amount of oxygen available in the concrete Eq 2.15 is negligible. The dominant reaction is water decomposition in the surrounding of the reinforcement the concentration of OH^-ions increases. On the anode, pollution of water takes place too.
The Cl^- ions are uncharged under the production of chlorine gas.

$$H_2O \rightarrow \frac{1}{2}O_2 + 2H^+ + 2e^- \quad 2.17$$

$$2Cl^- \rightarrow Cl_2 + 2e^- \quad 2.18$$

The chloride ions are transported along the flow lines of the direct voltage field. With an anode arrangement usually used for chloride extraction, the following picture occurs (Tritthart & Baumgartner, 2007):

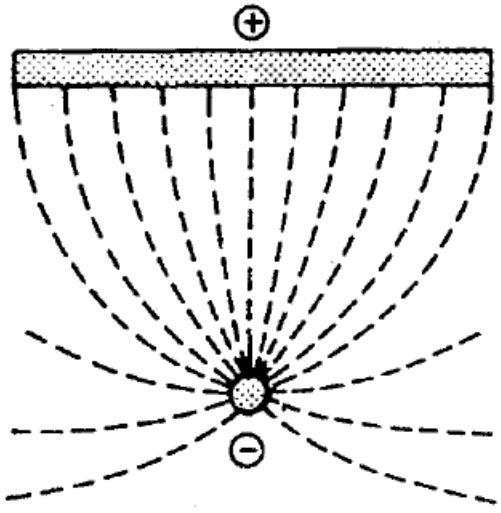

Figure 2.4 exemplarily flow lines during electrochemical chloride extraction (Elsener, 1990; Tritthart & Baumgartner, 2007)

The shorter the flow line, the greater the field strength and thus the migration velocity. The chloride extraction is low behind and in the middle between two reinforcement bars. Therefore, not the entire chloride is removed, and the risk exists that the remaining chloride reaches the

steels again after a while, and new corrosion is initiated. (Tritthart & Baumgartner, 2007) So, the electrochemical chloride extraction can remove the cause of corrosion but cannot stop the damage if the deterioration process is already advanced. Thus, this method is strictly speaking, not a rehabilitation method. Once corrosion has begun, chlorides are not necessary to continue corrosion, and ECE is not capable of repassivating highly corroded steel surfaces. (Miranda et al., 2007)

2.4 Concrete Resistivity

Concerning electrical conductivity, one has to distinguish between the conductivity of electrons, for example in metals, and the conductivity of ions in fluids. In the case of concrete or mortar, the charge transport goes through the electrolyte in the pore system. The electrical conductivity is the reciprocal of the electrical resistivity:

$$\sigma = \frac{1}{\rho} \qquad 2.19$$

Although concrete is not a homogeneous electrolyte contrarily to aqueous solutions, the concrete resistivity is usually assumed to be isotropic and homogeneous within the examined areas. The concrete resistivity ρ is always a material property and the product of the absolute resistance R of the concrete and the cell constant k:

$$\rho = R \cdot k \qquad 2.20$$

With:

- σ : Electrical conductivity [1/Ωm]
- ρ: Resistivity [Ωm]
- R: Resistance [Ω]
- k: Cell constant [m]

The resistivity of the concrete is highly influenced by the electrolyte, the water saturation of the concrete, and the pore structure. The more pore water and larger pores with a high degree of connectivity and lower tortuosity, the lower the resistivity. The resistivity increases by longer curing times (hydration) or by adding reactive minerals such as blast furnace slag, fly ash, and silica fume. Also, drying the concrete and carbonation increases resistivity values because carbonation reduces the number of ions available for carrying the current and may densify the concrete. In the case of non-carbonated concrete, the effect of the penetration of chloride ions

on the resistivity is relatively small. (R. B. Polder, 2001) Further information can be found in (Reichling & DAfStb, 2015).

For all sorts of conductivity, Ohm´s law is applicable. The electrical resistance describes the relation between applied voltage and resulting current.

$$R = \frac{U}{I} \qquad 2.21$$

With:

R: Resistance in Ω
U: Applied voltage in V
I: Current in A

2.4.1 Influence of the Moisture Content

The conductivity of concrete exists only because of the water in the pore structure and the ions (Na+, K+, Mg2+, Ca2+, OH-, Cl-, SO42-) solved in it. A completely dry mortar is nearly an isolator with resistivity values of about 10^6 Ωm. In contrast, a water-saturated mortar has a resistivity of over 100 Ωm. (Raupach et al., 2003b)

In civil engineering, the relation between resistivity and water content is often described by an empirical e-function, respectively logarithm function, s. e.g. Eq. 2.22 (Reichling & DAfStb, 2015):

$$w = \frac{A}{\ln(B*\rho+C)-D} + E \qquad 2.22$$

With:

w: Water content [M.-%]
ρ: Resistivity [Ωm]
$A-E$: Regression parameters

In fitting the function to experimental data, the aim is to extrapolate the water content for any measured resistivity of the concrete or mortar.

2.4.2 Influence of the Temperature

Besides the moisture content, the temperature highly impacts resistivity. The temperature dependency can be described by the Arrhenius equation (Logan, 1982; Raupach et al., 2003b):

$$R_1 = R_0 * e^{b*(\frac{1}{T_1}-\frac{1}{T_0})} \quad 2.23$$

With:

R_0	Electrolyte resistance at the temperature T_0 [Ω]
R_1	Measured electrolyte resistance at the temperature T_1 [Ω]
b	Temperature coefficient in Kelvin [K]

For parameter b in the literature, values between 3000 and 5000 K are mentioned, depending on the moisture content and other concrete parameters. (Raupach et al., 2003a)

2.4.3 Resistivity Measurement

The resistivity can be measured non-destructively using electrodes placed on the concrete surface. This requires at least two electrodes. A voltage is applied between the electrodes, and the resulting current is measured, or in the opposite direction, a current is applied, and the voltage is measured. In the case of this work, for the calibration curves, the resistivity was examined on core samples. In core samples with two faces cut parallel, the resistivity is calculated by (R. B. Polder, 2001):

$$\rho_{concrete} = R_{measured} * B/L \quad 2.24$$

With:

$\rho_{concrete}$:	Resistivity [Ωm]
$R_{measured}$:	Resistance between the plates [Ω]
B:	Area of the core face [m²]
L:	Length of the core [m]

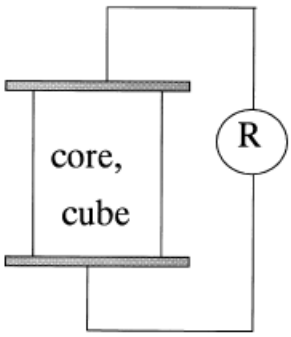

Figure 2.5 Two-electrode set-up (R. B. Polder, 2001)

2.4.4 Impedance Spectroscopy

Electrochemical impedance spectroscopy (EIS) is a method that allows a small amplitude of alternating current (AC) signal to investigate the impedance characteristics of a cell. The AC signal is scanned over various frequencies to receive an impedance spectrum for the electrochemical cell. EIS makes it possible to study the capacitive, inductive, and diffusion processes taking place in the electrochemical cell. The impedance spectroscopy has the advantage that no polarization potential must be considered. Therefore, voltage and current change over time and, with the appearance of capacities, with a phase shift. (Baeckmann et al., 1997; Chang & Park, 2010; Ciucci, 2019)

Ideal resistors induce a linear resistance to electron flow as potential changes. Capacitance C and Inductance L induce a resistance that depends on the frequency. (Brown, 2002)

$$Z = R + j\bar{\omega}L + \frac{1}{j\varpi C} \qquad 2.25$$

With:

$$\omega = 2 * \pi * f \qquad 2.26$$

Where:

- Z: Impedance [Ω]
- R: Resistance [Ω]
- j: Imaginary unit
- ω: Radial frequency [rad/s]
- L: Inductance [H]
- C: Capacitance [F]
- f: Ordinary frequency [Hz]

The impedance resulting from an inductor increases with frequency, in contrast, the impedance due to a capacitor is inversely proportional to frequency. In real electrical circuits, the impedance is often the result of both resistive and reactive components. To simplify expression and computation, impedance data are often subject to vector analysis and converted to complex numbers, such that:

$$Z = \frac{E' + E''j}{I' + I''j} = Z' + Z''j \qquad 2.27$$

With:

$$j = \sqrt{-1} \qquad 2.28$$

Where:

- Z': Real component of impedance [Ω]

Z'': Imaginary component of impedance [Ω]

E': Real component of field strength [V/m]

E'': Imaginary component of field strength [V/m]

I': Real component of magnetic field [Vs/m²]

I'': Imaginary component of magnetic field [Vs/m²]

It can be said that the real component of impedance (Z') represents the resistance, and the imaginary component (Z") represents the reactance. With ac circuits, the current and potential may not be synchronous; instead, the two waveforms are often shifted in time. This temporal offset is named phase (θ). Pure resistive circuits are in phase (θ = 0), while for purely capacitive or inductive circuits, the current is shifted 90° ahead or behind the potential waveform. Circuits exhibiting a limited capacitive behavior would have a phase angle less than 90° but greater than 0°. The absolute magnitude of the impedance (length of the vector) and phase angle can be calculated according to the following equations:

$$|Z| = \sqrt{Z'^2 + Z''^2} \qquad 2.29$$

$$\theta = \arctan\frac{Z''}{Z'} \qquad 2.30$$

Summarizing the results of impedance measurements over a wide range of frequencies and plotting both the log of the modulus of impedance and the phase angle as functions of the log of the frequency results in a Bode diagram. If the real and imaginary components of impedance are plotted on x and y coordinates, the result is named the Nyquist plot. (Brown, 2002)
Further information can be found in (Huang et al., 2011).

2.5 Previous Monitoring Techniques

Sensor systems to monitor the risk of reinforcement corrosion are used worldwide to reduce the risk of undetected corrosion problems, which often cause expensive repair measures when detected in a late stage when cracks and spalling already appear. In areas with difficult access or in cases where lanes have to be closed, the automatic inspection using sensors is more cost-effective than onsite inspections. (Raupach & Schießl, 2003)
For measuring the resistivity of concrete at different depths from the concrete surface, a sensor called multiring-electrode was developed at ibac. A scheme of the electrode is shown in Figure 2.6. The sensor has several stainless-steel rings separated by polymer rings. This allows the determination of the electrolytic resistance between each pair of neighboring stainless-steel rings by impedance measurements. The sensors are embedded into fresh concrete or by mounting them into hardened concrete with a special mortar. (Raupach et al., 2003a) However,

with these sensors, conclusions from the resistivity to the water content of the concrete can only be drawn selectively for the point of installation.

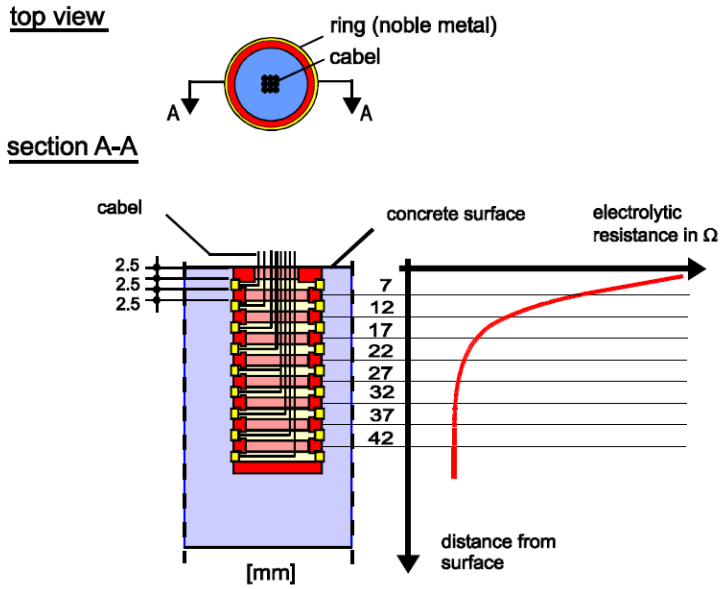

Figure 2.6 Schematic picture of the multiring-electrode (Raupach et al., 2001)

Since 1990 a system for the installation and the reinforcement preceding the concrete placement is available, the so-called Anode-Ladder-System. (Liu et al., 2021) For existing structures, the so-called Expansion-Ring-System exists. This system consists of the Expansion-Ring-Anode and a Cathode Bar, which must be inserted into drilled holes in the concrete cover. The Anode-Ladder-System consists of six bars; the Expansion-Ring-Anode consists of six measuring rings at different distances from the concrete surface. In this way, the ingress of chlorides and/or carbonation from the concrete surface into the structure and the resulting corrosion risk of the reinforcement can be measured automatically. As long as the critical chloride content and the carbonation depth have not reached the surface of the outer anode, all electrical currents are low. Over time the anode-rings will be depassivated one after the other. In measuring the electrical currents and voltages between anodes and cathode, the relationship between the depth of the critical chloride content or carbonation and time can be estimated. The time to corrosion of the actual reinforcement can be estimated by extrapolation using appropriate calculation models. (Raupach & Schießl, 2003; R. Schießl & Raupach, 1999) Another development is a simple “cathode bar” made of a noble metal with a low cathodic polarization resistance, which does not corrode in chloride contaminated concrete. These bars are embedded into the concrete close to the reinforcement, which is likely to corrode. By measuring the electrical macrocell current between the reinforcement and cathode bar, the development of the corrosion rate of the existing reinforcement can be evaluated. Furthermore, reference electrodes can be installed to monitor the electrical potential of the reinforcement, and AC-resistance measurements can be carried out to evaluate the electrical resistivity and the water content after calibration with the concrete. (Raupach et al., 2016) Recently this

measurement principle was improved by using a polymer instead of the alkaline mortar, which has the advantages of a more straightforward application and reliable measuring values directly after application because no water has to be used. Further information can be found in. (Helm, 2021)

2.6 Carbon-textile Reinforced Concrete

2.6.1 Textile Reinforced Concrete

“Textile Reinforced Concrete (TRC) is a high-performance cementitious composite using straight and parallel aligned fibers of suitable materials, e.g., AR glass and carbon, as continuous reinforcement in the form of textiles”. (Brameshuber et al., 2016)

Since the textile reinforcement does not corrode like steel reinforcement, the concrete cover can be held to a minimum, and thus thin concrete elements can be realized. Another area of application for TRC is strengthening layers for concrete structures. (Hegger & Voss, 2008; Peled et al., 2017)

Mainly alkali-resistant (AR-) glass rovings, carbon rovings, and aramid rovings which consist of several filaments produce textiles as reinforcement materials. The number of filaments in one roving can be calculated as a function of the diameter and density by the fineness in g/km (tex, Titer). A 320 tex roving consists of approx. 800 filaments”. (Raupach et al., 2006)

The load-bearing behavior of TRC depends on the interaction between the textile reinforcement and the mortar matrix, especially the load transfer from mortar to textile reinforcement. Textiles are coated to activate the whole roving, including internally located fibers.

Due to the coating, superior load transfer from the concrete to all the fiber filaments is achieved, and additionally, the impact of damage during the concreting process is minimized. (Morales Cruz et al., 2015)

Nowadays, epoxy resin or styrene-butadiene rubber (SBR) is used for coating. (Kulas, 2013)

2.6.2 Carbon Textiles Used for Cathodic Protection

For the use as an anode material in cathodic protection projects, technical carbon textiles are relatively new, and research work is limited. (Asgharzadeh, 2019; Asgharzadeh & Raupach, 2019; Wei et al., 2020)

The most used anode material is titanium because of its high current capacity, lightweight, and low consumption rate. However, it is costly and hinders the broad application of ICCP systems. Therefore, as an alternative, carbon fiber reinforced polymer (CFRP) anodes have gained much interest because of their high conductivity and affordable price, especially in the case of prevention systems when current densities are lower, and so requirements on the anode system are less strict. (Zhang & Tang, 2019)

Considering the Pourbaix diagram of carbon, one could conclude that carbon is unsuitable for an impressive current anode. (Chini et al., 2008) investigated the polarization behavior of carbon through polarization curves from 20 mV to 5000 mV and the effect of chlorides on corrosion. Due to the problem that it is impossible to measure the exact surface area of the exposed fibers for the current density, (Chini et al., 2008) used cross-section corrosion monitoring. “In this method, ten bundles of 24000-filament thread were cast in a non-conductive epoxy. The transparent pipe was used as a mold to monitor the accuracy of the procedure. After molding, the specimen was cut and ground to have a smooth and clear cross-section. This method gives a surface area of around 10 mm^2. (Chini et al., 2008) The investigations were carried out in a simulated pore solution with 1 and 3 % NaCl added. As a result, it was stated that carbon has a passive-active-passive behavior in alkaline solution with passive condition up to 500 mV polarization and then active up to 2500 mV. From that point, it starts the second passive condition. Adding chlorides into the solution increases the corrosion current densities at high polarization values. Still, this effect is slight at low polarization values, and chloride ions do not play a significant role.

Oxygen reduction has been observed from 750 mV polarization which could lead to mechanical damage of the surface of the carbon. (Chini et al., 2008) In (Chini, 2010), it is stated that carbon has a passive-active behavior with passivity up to polarization potentials of 300 mV and active behavior above this potential in the alkaline region. (Bertolini et al., 2004) investigated the behavior of a cementitious conductive overlay anode. The anode consisted of nickel-coated carbon fiber in a cementitious mortar. They conducted tests on concrete specimens with two layers of rebars that simulated reinforced concrete slabs. Therefore, anodic current densities in the range 10–100 mA/m^2 concerning the anode surface were imposed. The cementitious conductive coating turned out to be suitable for CP and showed good behavior when a current density of up to 20 mA/m^2 was applied for two years. However, current densities of over 50 mA/m^2 lead to a damaged cementitious matrix due to the acidity produced by the anodic reaction after just 1–2 months of use. So (Bertolini et al., 2004) suggested a maximum current density of 10–15 mA/m^2, referred to the surface of concrete covered by the anode, and a distance of 1 m between primary anodes for a safe design. (Lambert et al., 2015) used carbon fiber reinforced polymers (CFRP) to provide structural strengthening and electrochemical corrosion protection to reinforced concrete elements suffering from corrosion-related damage. The test program consisted of 12 beams with uncorroded control beams, corroded control beams, beams with only a strengthening function, and beams with the mentioned dual function. Furthermore, different applications were used, namely longitudinal CFRP fabric and U-wrapping fabric. (Lambert et al., 2015) came to the results that CFRP fabric anode can operate at very high current densities of about 128 mA/m^2 of steel area with only a small loss of mechanical bond. Furthermore, they found out that U-wrapping effectively reduces the de-bonding at the CFRP fabric anode and concrete surface interface. If this de-bonding is reduced, the

strength of dual-function beams increases significantly by 111.37 % compared to the corroded control beam. (Lambert et al., 2015)

(Asgharzadeh, 2019) investigated the durability of carbon textile under anodic polarization using a simulated pore solution and mortar. He generated current density-potential curves through a potentiodynamic experiment and used SEM images to detect decomposition of the sizing of the carbon filaments as a result of anodic polarization. He found that impregnated carbon textiles degraded the epoxy and SBR impregnations. Still, the carbon fibers' degradation was not observed for potentials up to 2200 mV vs. NHE. He examined that decomposition of the sizing and epoxy matrix occurs in the transition region of its current density-potential curves at potentials of about 900 mV vs. NHE and 1050-1150 mV vs. NHE. The SBR impregnation is decomposed at potentials of 490 mV vs. NHE. After 240 days of potentiostatic polarization, no visible damage had occurred to the mortar test specimens. (Asgharzadeh, 2019) The carbon meshes used in (Asgharzadeh, 2019) are the same for the experiments in this work.

2.6.3 Smart Deck

In the context of a joint research project, an innovative, multifunctional, and thin (35 mm) interlayer was developed, which provides significant benefits - in comparison to state of the art - for new and existing bridge constructions. This interlayer is based on textile concrete and provides four functions: an all-over real-time humidity monitoring, a chloride barrier, preventive cathodic corrosion protection, which can be adjusted by sections, and a reinforcement of those bridges with insufficient load-bearing capacity. Using the monitoring system early recognition of damages in the sealing layer and combined with the cathodic corrosion protection, preventing traffic obstructions is possible. The renewing of the bridge deck sealing must not be carried out immediately but can be postponed to periods with little traffic. All four functions are realized by textile reinforcement, consisting of carbon and a newly developed mortar. The interlayer is divided into sections arranged transverse to the lane. Each section builds a separate sensor.

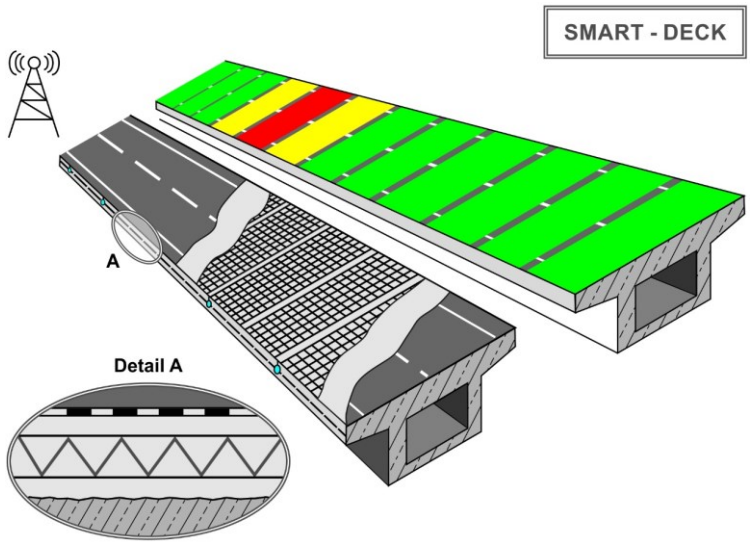

Figure 2.7 : Smart Deck: intelligent, multifunctional interlayer for bridges (Driessen & Raupach, 2015b)

The electrical resistivity between the two carbon layers is measured. When the sealing starts to leak and water permeates into the interlayer, a drop in the measured electrical resistivity is detected. The operator of the bridge construction receives a note about the leakage in real-time. Therefore, all relevant data are transmitted via the internet and are presented in a simple form. When damage in the sealing is detected, the cathodic corrosion protection can be switched on. Thus, the constructional measures of the bridge deck sealing can be postponed to periods with less traffic or to that point of time when a renewal of the sealing is planned anyway. An electrical field is generated between the carbon and the reinforcement with a rectifier, which disables chloride migration into the construction. Thus, the depassivation of the steel is prevented.

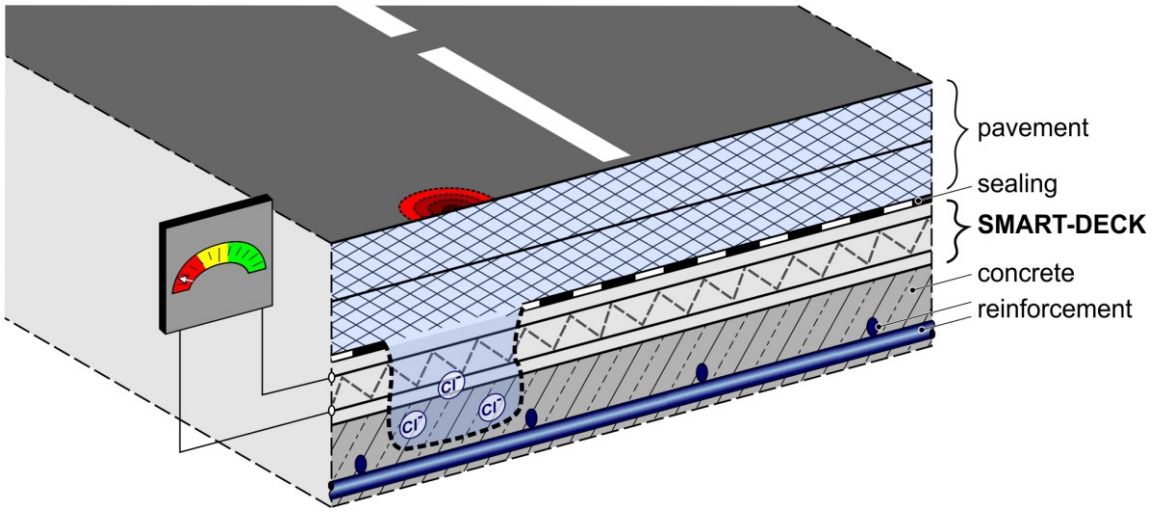

Figure 2.8 Smart Deck: Measurement of the resistivity (Driessen & Raupach, 2015b)

3 Experimental Investigations and Development of the Theoretical Models

3.1 Structure of the Investigations

Figure 3.1 gives an overview of the investigations carried out in the context of this thesis and the papers in which they are discussed.

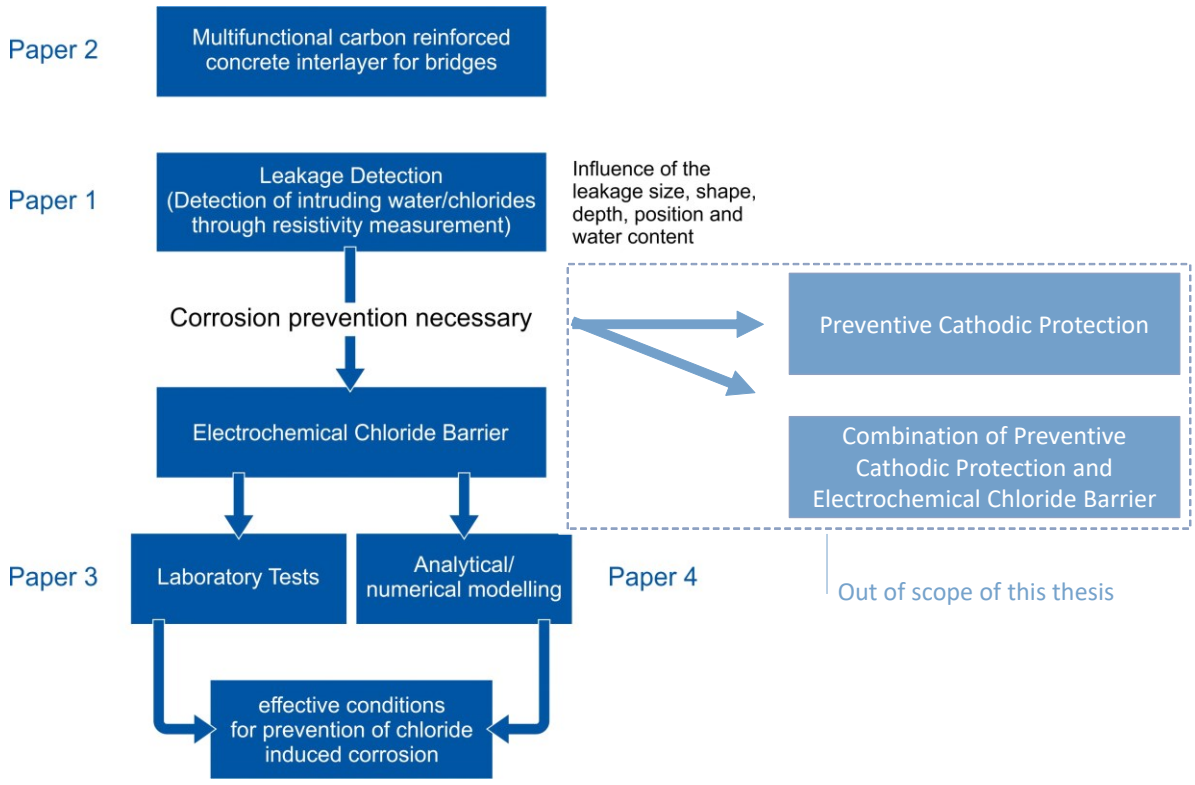

Figure 3.1: Overview of the structure of the thesis

Paper II gives an overview of the functions of SMART-DECK and the laboratory tests, simulations, and outdoor installations carried out to investigate these. For the functionality, two main aspects have to be examined. Firstly, it has to be investigated under which circumstances and extensive leakage detection is possible. Therefore, in paper I, numerical investigations were carried out to quantify the influence of the mortar's leakage size, shape, depth, position, and water content on the detectability. With the knowledge from the investigations shown in papers, I and II one has the tool to determine the point of time when corrosion prevention becomes necessary due to intruding water and chlorides. At this point, the electrochemical chloride barrier and, a bit later, the preventive cathodic protection should be switched on. The difference between both is that the Electrochemical Chloride Barrier leads to a reduced chloride ingress due to the electrical field. In contrast, the Preventive Cathodic Protection leads to a higher critical chloride content because of the cathodic polarization of the steel. To access the

practicability of the electrochemical chloride barrier, laboratory tests (paper III) and analytical and numerical modeling (paper IV) were carried out. So, as a result of this work, it is possible to conclude under which circumstances and to which extent the electrochemical chloride barrier can provide corrosion prevention.

3.2 Supplement to Laboratory Tests

The measuring technique was developed entirely at the Institute of Building Materials Research of RWTH Aachen University. A multichannel measurement device was developed for the main series, which can be seen in Figure 3.2 and Figure 3.3. It was planned to measure with a four-electrode set-up. In this process, the carbon meshes were supposed to be the outer electrodes, and two metal pins in the middle of the carbon layer should work as the inner electrodes. However, the electrical connection between the metal pins and the mortar did not work reliably, so the voltage was applied on the carbon meshes. The instant-off potential was measured to calculate the voltage in the electrolyte, respectively the potential gradient that determines the chloride barrier's effectiveness. Using the externally applied voltage between anode and cathode is improper for investigating the chloride migration because it contains the voltage drops at the electrodes. Therefore, the potential gradient relevant for the chloride migration would be overestimated.

The potential gradient ΔU was calculated by use of formula 3.1:

$$\Delta U = U_{On} - U_{Inst} \qquad 3.1$$

With:

U_{On}: On-Potential [V]

U_{Inst}: Instant-Off-Potential [V]

It is known that the polarization of the electrodes does not change immediately after the system is switched off and that the spreading resistances at the electrodes are negligible due to the parallel arrangement. Thus, the observed potential drop is considered to occur over the mortar of the specimen only and can therefore be seen as the voltage contributing to the migration process.

The current was measured continuously. The measurement instrument can work in a voltage range between 0-10 V and a current range between 0-250 mV.

Figure 3.2: Utilized current sensors (1/2)

Figure 3.3: Utilized current sensors (2/2)

Detailed Information about the laboratory tests is provided in paper III.

4 Multifunctional Carbon-reinforced Concrete Interlayer for Bridges

4.1 SMART-DECK: Multifunctional Carbon-reinforced Concrete Interlayer for Bridges

4.1.1 Abstract

The service life of bridges is often threatened by an insufficient shear force capacity in the transverse direction as well as by leakages in the sealing layer which led to chloride ingress and, therefore, corrosion damages. A thin, multifunctional interlayer of textile reinforced concrete called SMART-DECK was developed to prevent expensive repair work and traffic obstructions. This interlayer provides three functions: full-surface moisture monitoring in real-time, preventive cathodic corrosion protection, and increased shear force capacity. The bridge operator can monitor the condition of the sealer in real-time. The relevant data are transmitted via the internet and show the state of the sealer in a simple color scheme. If leakage occurs, the cathodic corrosion protection can be switched on to protect the reinforcement from corrosion damage. The renewing of the damaged bridge deck sealing must not be carried out immediately but can be postponed over years, e.g., to periods with little traffic. In this paper, the scientific approach for the realization of the system is presented, beginning with laboratory pretests on the materials and numerical simulations. The results are used to test the system's functions in the laboratory and later on two demonstrators. An outlook will present the following research questions.

4.1.2 Introduction

A sustainable and efficient transport infrastructure becomes more and more critical because of the increasing traffic density. Damages on bridges lead to reduced service life and long-term problems: chloride ions can migrate into the concrete, which causes corrosion of the reinforcement and thus threatens the durability of the construction. The corrosion of the reinforcement can only be seen on the bridge's surface when a high degree of impairment is already reached. At that point, comprehensive building operations are necessary, leading to traffic obstructions and thus to economic losses. By now, sensors for monitoring humidity in constructions or sensors that help estimate the probability of corrosion exist, but these sensors work only discretely at the point of installation. (Raupach et al., 2013)

Monitoring a complete construction would need many sensors, which is often not economical. The interlayer will be divided into sections arranged transverse to the lane. Each section builds a separate sensor. Two technical textile layers are arranged with a spacing of 15 mm. The electrical resistivity between the two layers is measured as seen in Figure 4.1.

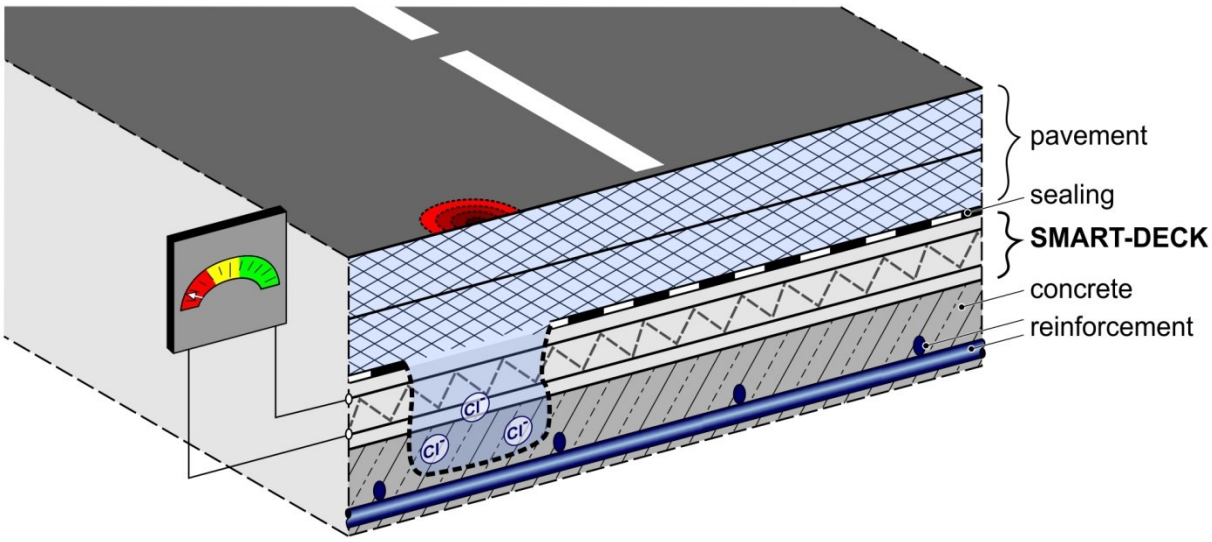

Figure 4.1. Schematic representation of the structure and functioning of SMART-DECK

When the sealing starts to leak and water permeates into the interlayer, a drop in the measured electrical resistivity is detected. The operator of the bridge construction receives a notification about the leakage. It is planned to monitor the condition of the sealing in real-time. Therefore, all relevant data are transmitted via the internet and are presented in a simple form e.g., in a color scheme. When damage in the sealing is detected, the cathodic corrosion protection can be switched on. Thus, the constructional measures of the bridge deck sealing can be postponed to periods with less traffic or to that point of time when a renewal of the sealing is planned anyway. An electrical field is generated between the carbon and the reinforcement with a rectifier, which disables chloride migration into the construction. Thus, the depassivation of the steel is prevented. (Driessen & Raupach, 2015b)

4.1.3 Structure and Materials

SMART-DECK is constructed modularly, meaning that the three functions can be installed in various combinations needed for the particular building. For example, if the load-bearing capacity of the bridge is sufficient, only the monitoring and the function of the preventive cathodic protection will be installed. In this case, the system can be reduced by one carbon layer and becomes even thinner, reducing the carbon needed and costs. The modularity allows the installation of the system in existing constructions as well as in new bridges. The general structure consists of two carbon meshes which are kept at a distance of 15 mm with spacers and placed on the shot-blasted construction concrete. The covering of the mortar above and below the carbon meshes is 10 mm. The interlayer covers the full-bridge superstructure between the cantilevers. Currently, the average measuring field has a width of 1.20 m. The length depends

on the width of the bridge. The measuring fields have a spacing of 20 mm between each other to guarantee electrical disconnection.

4.1.3.1 Textile Carbon Reinforcement

The reinforcement of SMART-DECK is biaxial carbon meshes with a mesh size of 38 mm. These are impregnated with a special epoxy resin. Insulating spacers are preinstalled to guarantee the spacing between the carbon meshes and the spacing to the construction concrete. The carbon meshes are anchored to prevent the floating of the carbon reinforcement during the pouring of the mortar. Figure 4.2 shows the carbon meshes with the spacers before pouring the mortar.

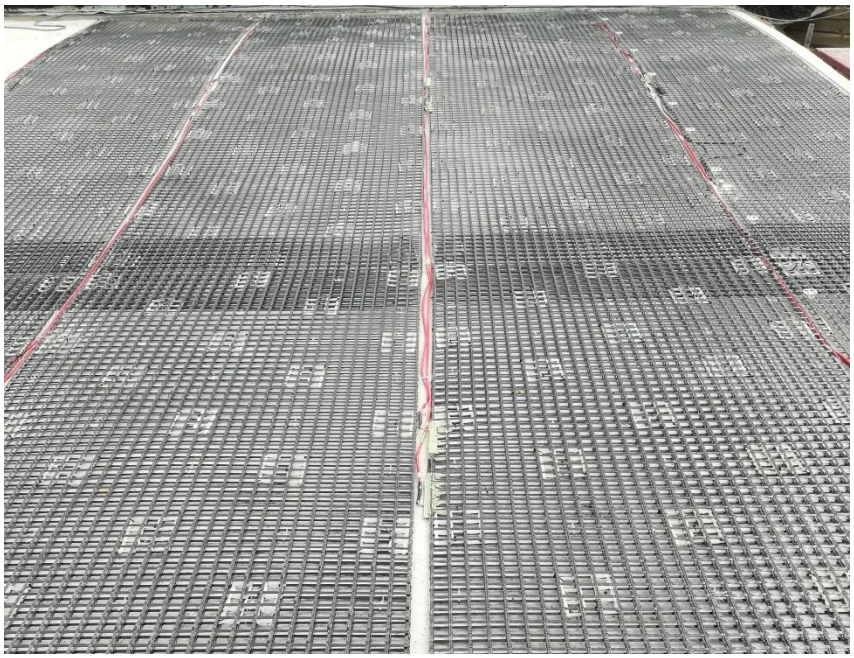

Figure 4.2. Carbon textile reinforcement of some measuring fields before placement of the mortar

4.1.3.2 Mortar

A high-performance mortar specially developed for the project was used. The mortar has a maximum grain size of 4 mm. It meets the competing demands of being flowable enough that the textile reinforcement is fully embedded and stable enough to manufacture a gradient of 2.5 % of the road's inclination.

To receive a finely graduated humidity monitoring, the mortar must have a high sensitivity for humidity. The mortar should have a wide range in resistivity values at different moisture contents. To reach this objective, a suitable pore structure has to be found. In this context, capillary pores with low constrictivity and tortuosity could achieve the intended properties. (Reichling et al., 2012)

Therefore screening of different mortars was conducted by investigating the water content/ resistivity behavior of the mortars. (Driessen & Raupach, 2016)
The procedure is described in the next chapter.

4.1.4 Monitoring

4.1.4.1 Relationship between Water Content and Resistivity

The detection of leakages is based on measuring the resistance between two layers of carbon textiles. Using calibration curves, one can conclude the water content of the mortar from the resistivity values. (Elkey & Sellevold, 1995)
Under an intact sealer after a few years of desiccation, the mortar shows high resistivity values. If leakage occurs, water permeates into the interlayer, and a drop in resistance is measured. Empirically, a frequency of 108 Hz provides good results. At this frequency, no significant polarization of the electrodes occurs, and this frequency guarantees that the cable length does not lead to a falsification of the measured values. For SMART-DECK, a voltage of 2 V was chosen. Impedance tests showed that 108 Hz lays in the acceptable frequency range. Figure 4.3 shows the impedance and phase angle for a frequency range from 10 - 10000 Hz for the SMART-DECK set-up for two different time points.

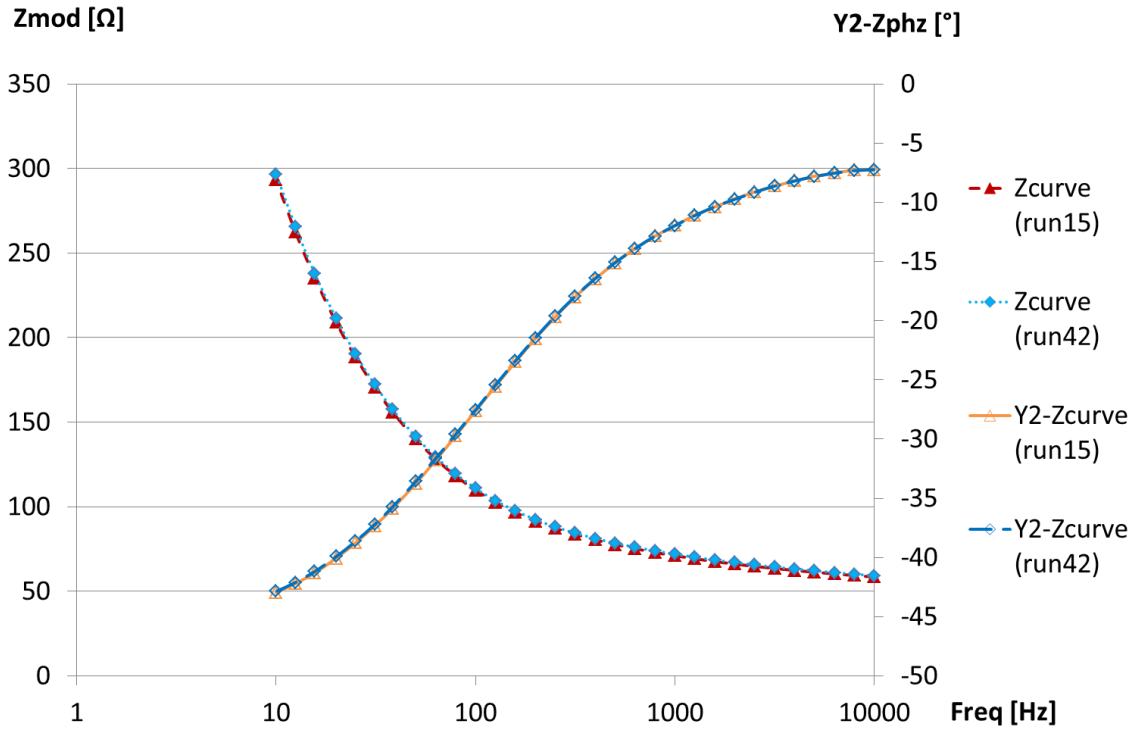

Figure 4.3. Impedance and phase angle for 10-10000 Hz

The calibration curves for the relation between water content and resistivity were prepared in the laboratory using a two-electrode-set-up. An alternating voltage is applied, and the resulting

current is measured. The ratio of these values leads to the alternating current resistance respectively, the electrolyte resistance of the mortar. Using Ohm's law:

$$R = U/I \quad (4.1)$$

With:

R: Electrolyte resistance [Ω]
U: Applied voltage [V]
I: Current [A]

For the investigations, frequencies from 100 Hz to 100 kHz are tested. The resistances depend on the geometry of the specimen. To compensate for this, a geometry factor is used:

$$\rho = R \cdot k \quad (4.2)$$

With:

ρ: Resistivity in Ohm-meters [Ωm]
R: Electrolyte resistance in Ohm [Ω]
k: Geometry factor in meter [m]

Specimens are stored underwater for these measurements until the measured resistivity values stay constant. The measured values and the weight of the specimens are recorded. Afterwards, the specimens are dried to reach low water contents. Starting at these contents, different moisture contents are being adjusted by adding various amounts of water. The specimens are packed in a closed environment to reach a homogenous water distribution. After two weeks, the specimens are being unpacked and weighed. The resistivity is measured before the specimens are dried again up to a constant weight and then weighed again. Based on these data, the relationship between humidity and resistivity values can be calculated.
Having determined the resistivity values with the corresponding moisture contents, a regression analysis using the following regression function is carried out. (Brameshuber et al., 2003; Harnisch, 2003)

$$u = \frac{A}{\ln(B \cdot \rho + C) - D} + E \quad (4.3)$$

With:

u: Moisture content referred to the mass of mortar [M.-%]
ρ: Mortar resistivity [Ωm]
A-E: Regression parameters

The measured values and the according regression curve can be seen in Figure 4.4 for the chosen mortar (M2).

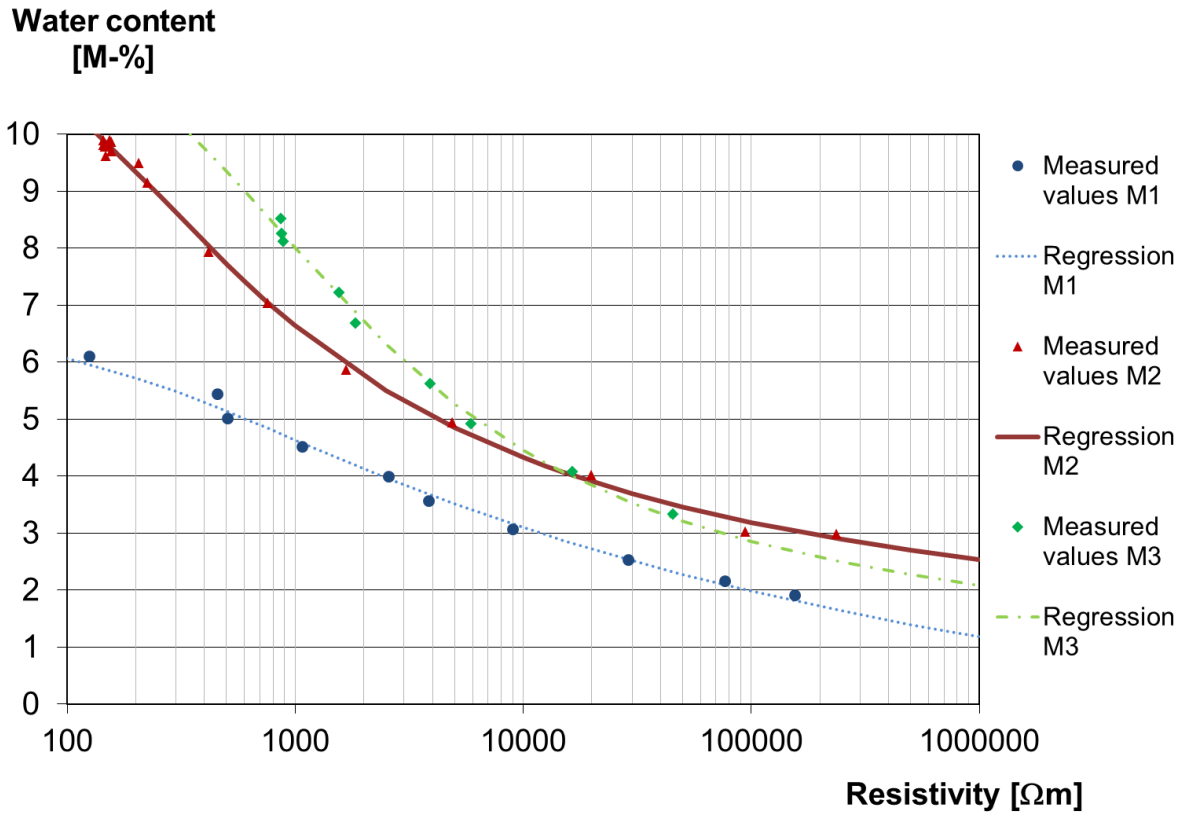

Figure 4.4. Relationship between water content and resistivity of the investigated mortars

As a reference, two other mortars (M1 and M3) which were tested are pictured. However, mortar M3 showed a more disadvantageous rheological behavior than mortar M,2. For mortar M1, the regression curve evolves with a lower gradient and therefore shows a lower sensitivity. Therefore, mortar M2 was chosen and is the base for all subsequent investigations.

4.1.4.2 Numerical Simulations

Numerical simulations were carried out using the calibration curve as an input parameter. As the main question, it should be investigated which leakage size of the sealer is detectable under different boundary conditions, such as the resistivity values of the dry mortar under an intact sealer or the wet mortar in a leakage zone. Other influencing parameters are the position of the leakage in the measuring field and the form of the leakage or the depth up to which water is soaked into the mortar. Based on laboratory tests, resistivity values up to 1000 Ωm represent a wet mortar in a leakage zone, and resistivity values above 1000 Ωm correspond to a dry mortar under the intact sealer. However, these values cannot be interpreted as a sharp threshold. The more significant the difference in resistivity values between a dry and a wet

mortar, the easier is the detection of leakages. Furthermore, detection becomes easier with greater leakage sizes and smaller measuring fields. The numerical simulations showed that even leakages of a few percentages of the total field size are detectable. The other main result is that besides the resistivity values and the leakage size, only the depth of a leakage significantly influences the detectability. (Driessen & Raupach, 2019)

Comparison between one and two Carbon Layers

Simulations were carried out for two different variants of SMART-DECK:

- For the standard set-up where the resistance is measured between the two carbon meshes.
- For the possible set-up with just one carbon layer where the resistance is measured between the carbon layer and the steel reinforcement of the construction concrete.

For the second option, the resistivity values of the construction concrete were presumed to be three times higher than the respective assumed resistivity values of the SMART-DECK mortar because it is expectable that the construction concrete dried up over decades before the first damage of the sealing occurs. The AC DC module of the software COMSOL Multiphysics was used for these simulations. For the electrical potential of an electrolyte in an electrical field, the following equation holds in general: (Krey & Owen, 2007)

$$-\nabla * (\varepsilon_0 * \varepsilon_r * \nabla V) = 0 \qquad 4.4$$

With:

V: Potential [V]

$\boldsymbol{\varepsilon_0}$**:** Electrical field constant [-]

$\boldsymbol{\varepsilon_r}$**:** Relative permittivity [-]

With the assumption of an isotropic material of the electrolyte, a constant frequency, temperature, and a constant magnetic and electrical external field, Eq. 4.4 can be rewritten as: (Lehner, 2006)

$$\Delta V = 0 \qquad 4.5$$

So, the potential in the mortar can be computed under the mentioned assumptions for given boundary conditions, i.e., potentials or voltages of the carbon layers, respectively.
The relationship between potential, current density, and electrolyte resistance is described by Ohm's law, which can be expressed with the following formula assuming isotropic electrolytes: (Jackson et al., 2006, S. 200)

$$i = -\frac{1}{\rho}\nabla V \qquad 4.6$$

With:

i: Current density in A/m²

ρ: Resistivity in Ωm

V: Potential in V

The differential equation system consisting of equations five and six are solved numerically with COMSOL to compute the resistivity ρ as an output parameter.
In this context, the voltage applied can be chosen arbitrarily because the res (cf. Eq. 4.6).

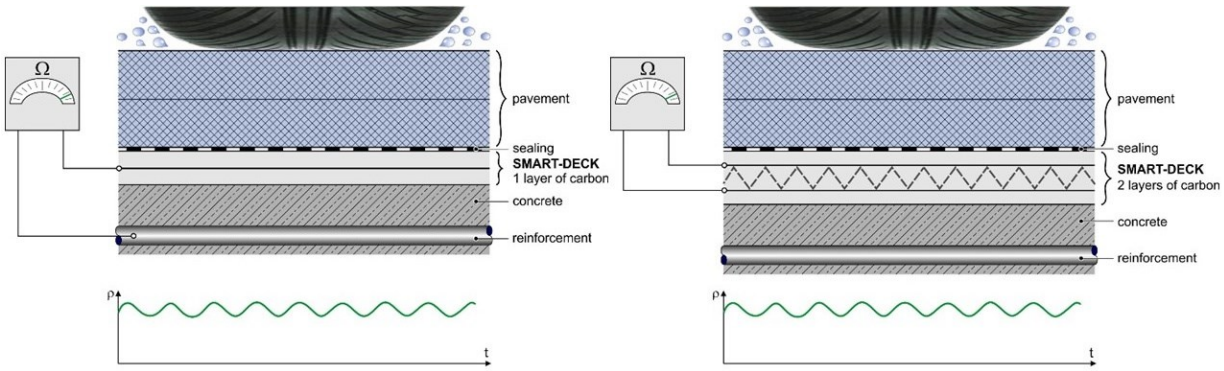

Figure 4.5: Simulated resistivity drops for intruding water for the standard structure and the structure with the measuring field

Figure 4.5 compares the simulated resistivity drops for intruding water for the standard structure on the left side and the structure with the measuring field between one carbon layer and the reinforcement on the right.

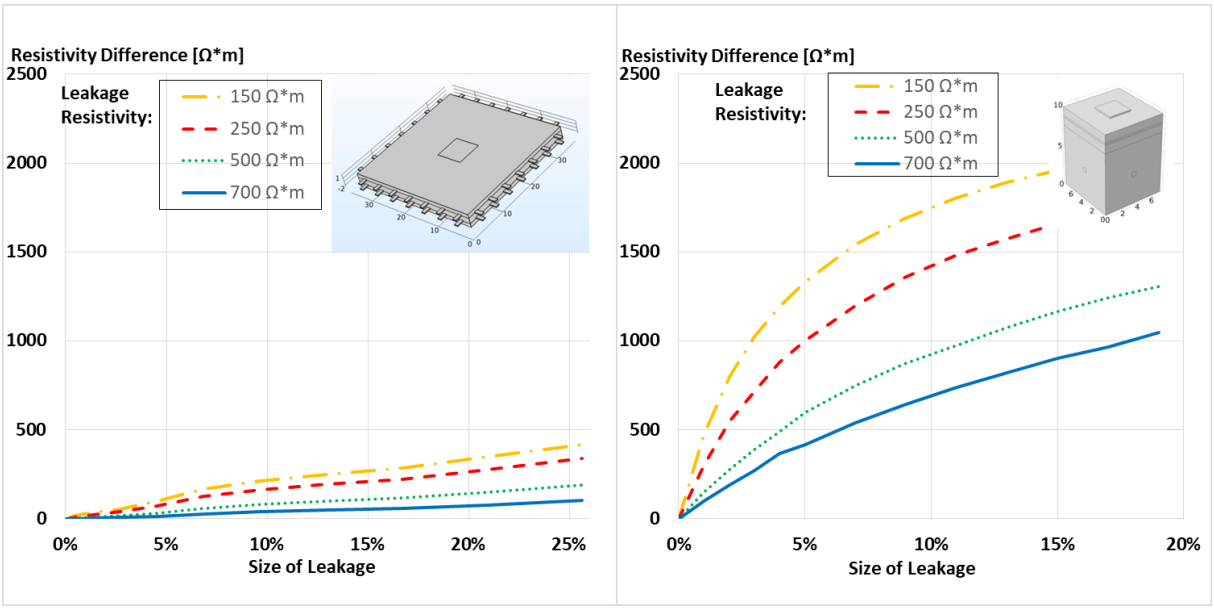

Figure 4.6. Simulated resistivity drops for different structures, different leakage sizes, and various initial resistivities

The resistivity drops caused by leakage and intruding water are greater for the version on the right side due to the greater resistivity value of the construction concrete and, therefore, the greater difference to the values of the wet mortar in the leakage zone. With a measuring resolution up to 0.01 Ωm, leakages of a few percentages of the total field size are detectable for both versions. Nevertheless, one must consider that the original structure with two carbon meshes allows the detection of leakages in the SMART-DECK layer. At t in the second version, the chloride contaminated water has already reached the construction concrete when detection is possible. Of course, the resistivity values decrease with the depth of the leakage. The simulated resistivity values over the depth of the measuring field are compared in Figure 4.7 and Figure 4.8.

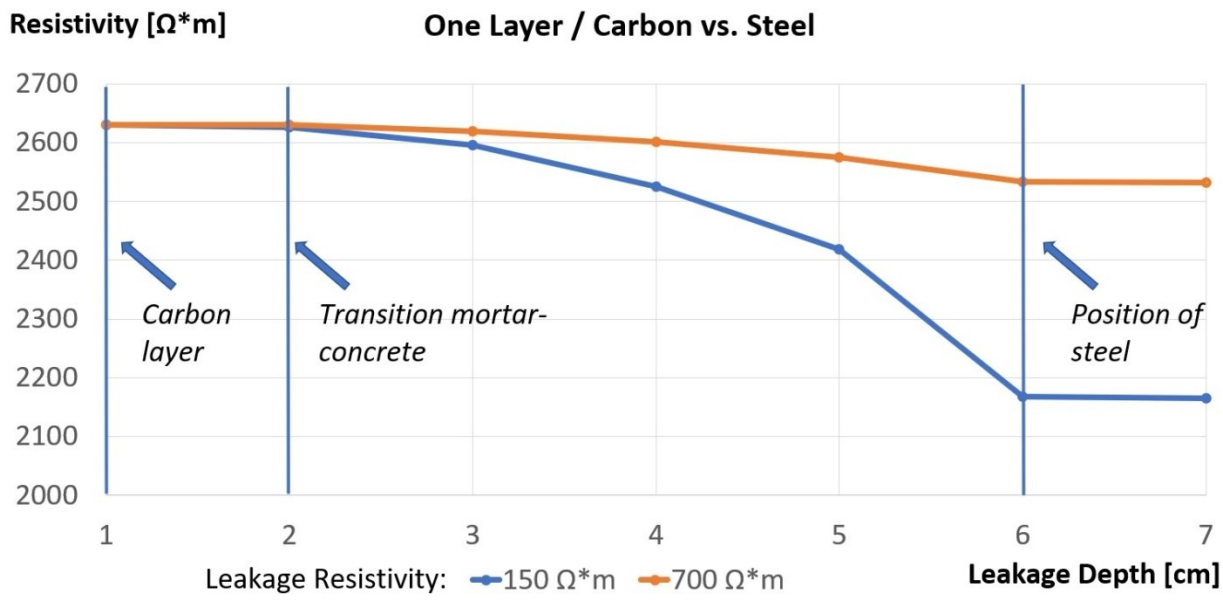

Figure 4.7. Resistivity values as a function of the leakage depth for the one-textile-layer version

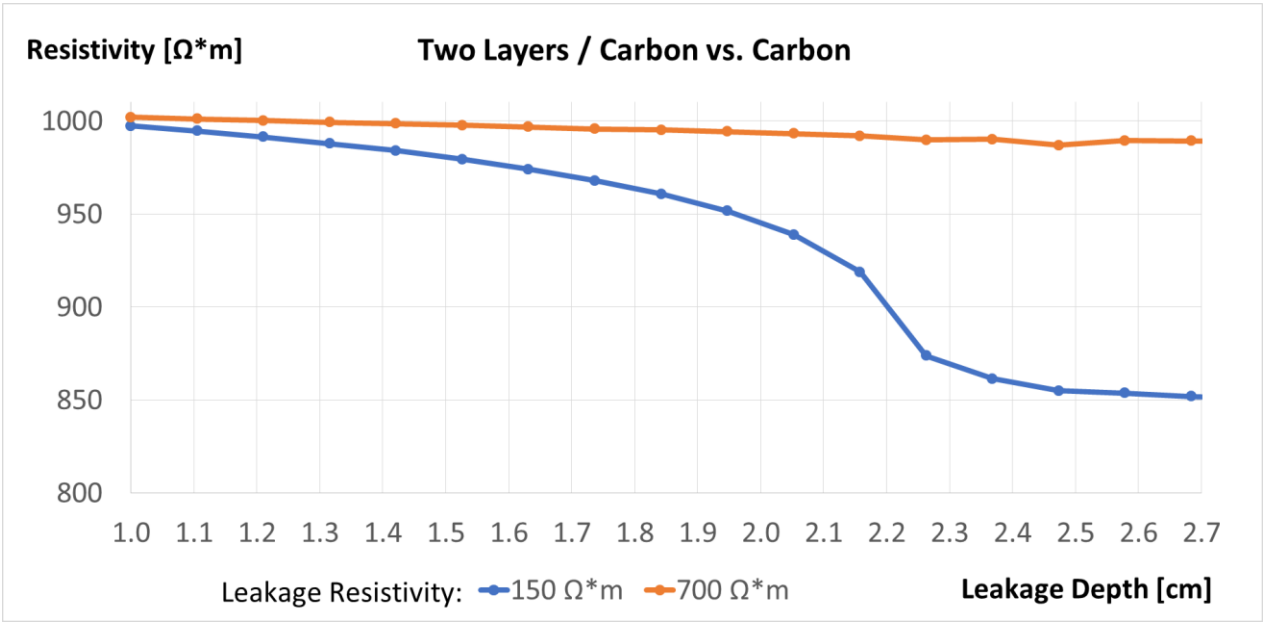

Figure 4.8. Resistivity values as a function of the leakage depth for the two-textile-layer version

In this example, a mortar resistivity of 1000 Ωm and a concrete resistivity of 3000 Ωm were presumed. This leads to a combined resistivity of approximately 2630 Ωm as a reference resistivity in a condition without leakages for the version with one carbon layer. Starting from this reference resistivity, a clear drop in the resistivity values for this version can be seen at first at a depth between three to four centimeters, thus in the area of the construction concrete. So, one has to weigh between the advantages of the one-carbon layer version, which are the reduced costs and the thinner layer thickness, and the disadvantages like the deeper chloride ingress. Furthermore, different possible reinforcement ratios and construction concrete lead to

more varying conditions in the SMART-DECK version with just one carbon layer, making further investigation necessary.

4.1.4.3 Monitoring in Laboratory Tests

To test the detectability of leakages, artificial leakages were produced on top of mortar specimens in the laboratory. Specimens with a size of 440 x 480 x 35 mm³ were cast. The structure with two carbon meshes with a spacing of 15 mm was used. The specimens were sealed with epoxy by leaving out artificial leakages. A different form, size, or position of the leakage was tested on each specimen. Water basins were formed on top of the specimen to guarantee a permanent water admission, as illustrated in Figure 4.9.

Figure 4.9. Specimen for the detectability-test with two artificial leakages

The carbon meshes of the specimens have electrical connections for a continuous resistance measurement during the testing time. The resistance is measured with frequencies between 10 Hz and 10 kHz. Figure 4.10 shows an exemplary plot of a resistance measurement. For two days, the resistance was measured before water was applied.

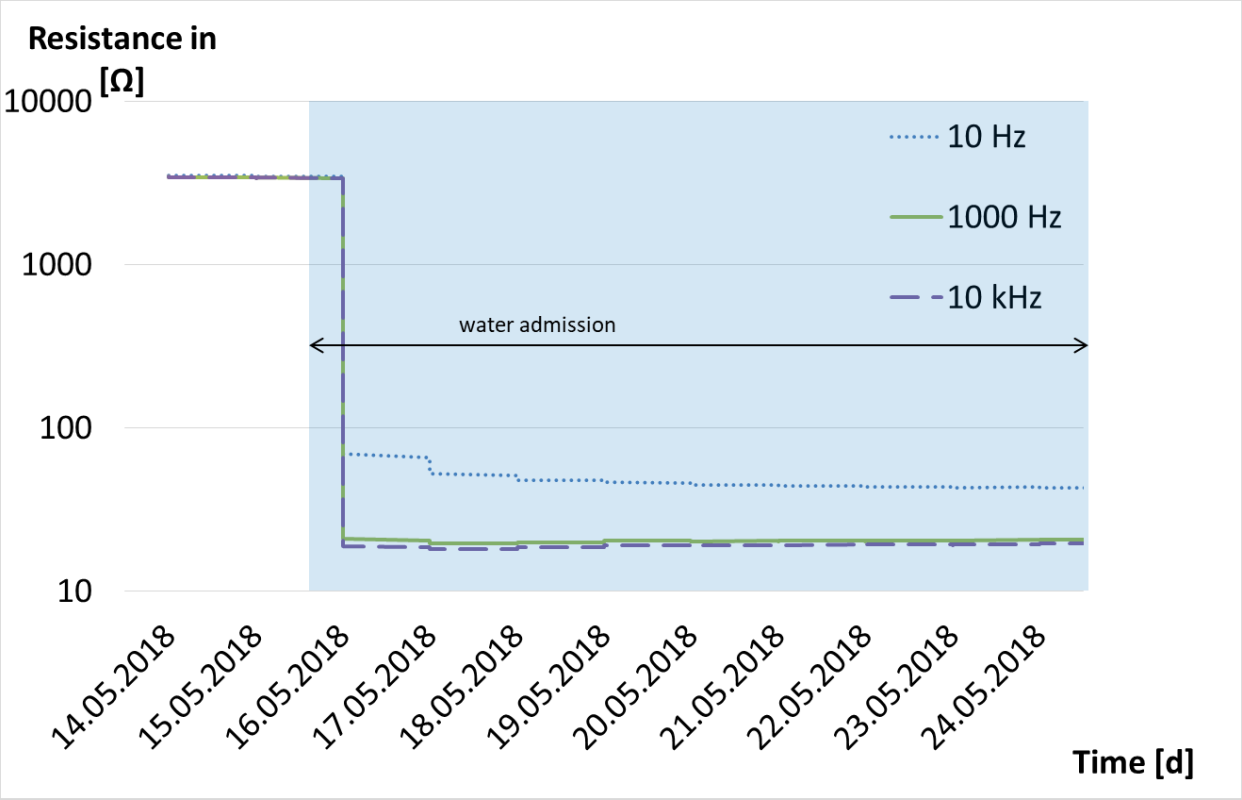

Figure 4.10. Exemplary resistance measurement during water admission

The resistance measurement was pursued without a break during the water admission, so one can see that a few hours after water admission, a significant drop in resistance at all frequencies occurs. The discrepancy of the 10 Hz curve can be explained by a polarization of the electrodes at this frequency.

Besides the moisture content, the temperature dramatically impacts the resistance. With increasing temperatures in the structure, the ion mobility within the electrolyte increases, and the conductivity increases. (Osterminski et al., 2012)

The Arrhenius equation describes the impact of temperature in concrete. (Raupach et al., 2003a)

$$R_1 = R_0 * e^{b*(\frac{1}{T_1}-\frac{1}{T_0})} \qquad 4.7$$

With:

R_0	Electrolyte resistance at the temperature T_0 [Ω]
R_1	Measured electrolyte resistance at the temperature T_1 [Ω]
b	Temperature coefficient in Kelvin [K]

The temperature coefficient should be determined for each mortar or concrete. In literature, a range between 3000-7000 K is mentioned depending on the moisture content and concrete

properties, see for example. (Bürchler, 1996; Raupach, 1992; Raupach et al., 2003a) For a temperature compensation of the resistance values, the temperature coefficient for the SMART-DECK mortar was investigated in the laboratory. Therefore, specimens with a two-electrode-set-up inside, pictured during preparation in Figure 4.11, were partially-saturated (25-30 %: 60-65 %; 85-100 % moisture content).

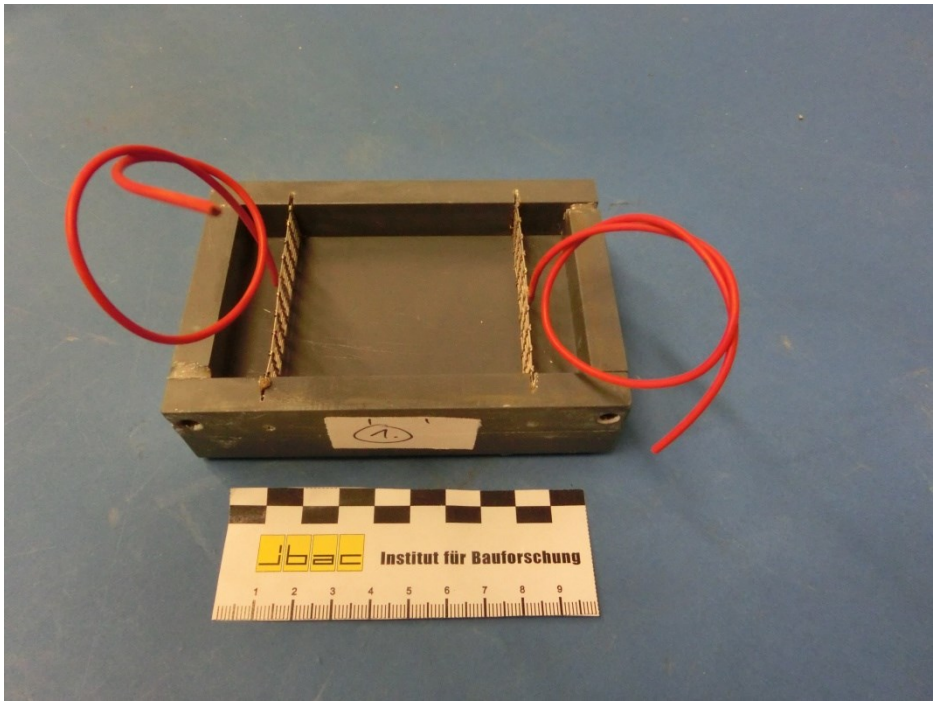

Figure 4.11. Specimen for the investigation of the temperature dependence of the mortar

After adjusting the water content, the specimen was sealed with epoxy and stored under different temperatures (-10; -2; 0; 5; 20; 50 °C). For the SMART-DECK mortar, a temperature coefficient of 4040 K for the estimated initial saturation of the mortar could be validated as appropriate, which can be seen in Figure 4.12.

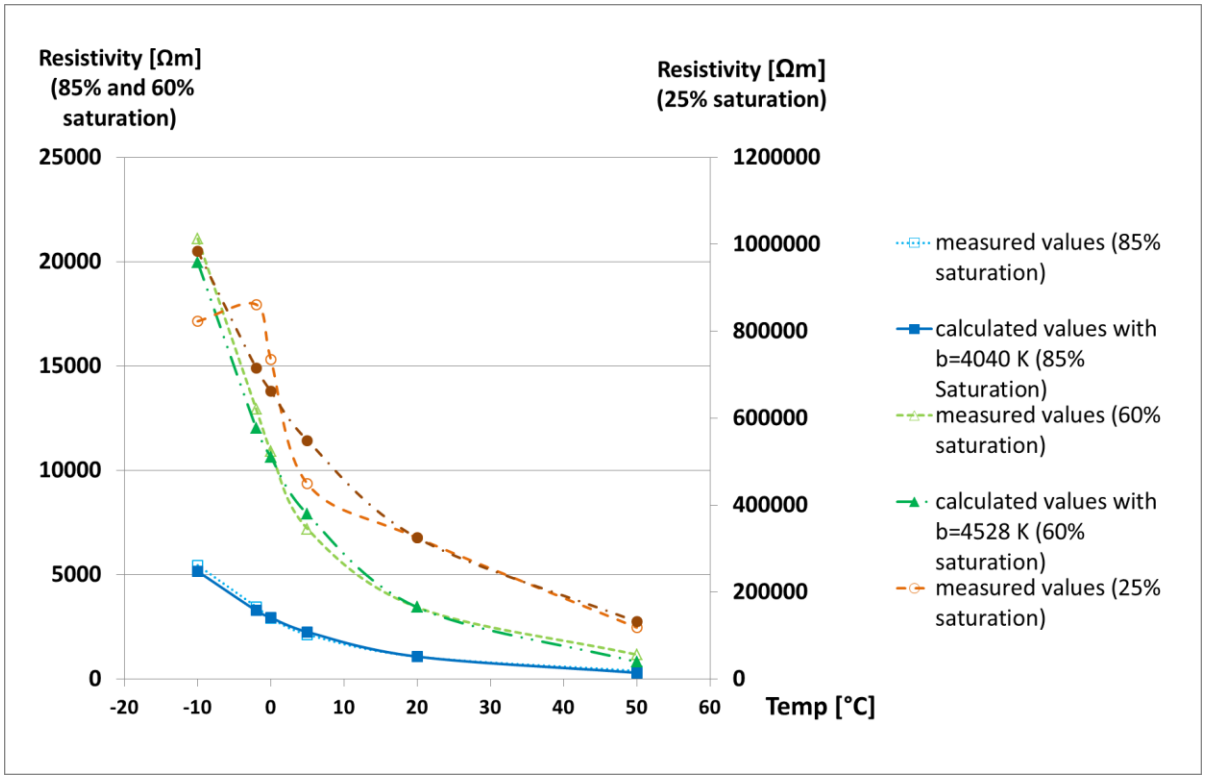

Figure 4.12. Validation of the temperature compensation

As the temperature coefficient depends on the humidity, the appropriate coefficient will change with ongoing desiccation of the mortar

4.1.4.4 Monitoring on Outdoor Demonstrators

Besides the investigations in the laboratory, two outdoor demonstrators were built. The first has a size of 80 m². The aim was to test the detectability of leakages under natural weather conditions. On demonstrator four, electrically disconnected measuring fields were realized. Electrical connections were made, and cables were stored in a control box near the demonstrator. As in the laboratory, artificial leakages were produced by applying water basins on the surface of the demonstrator and sealing the rest of the surface with epoxy. Water basins were used to prevent fast desiccation because it is assumed that if actual leakages occur in the sealing layer, an accumulation of water over the SMART-DECK layer takes place. Figure 4.13 shows the surface with the artificial leakages.

Figure 4.13. Sealed demonstrator with artificial leakages

Again, different forms, sizes, and positions of the leakages were tested. The newly developed full-surface resistance measurement is simultaneously verified via multiring sensors. These sensors usually have nine rings of stainless steel separated by isolating plastic rings. The resistance between neighboring rings can be measured by applying an alternating voltage. That way, one receives a graded profile of the resistance over the depth. (Brameshuber et al., 2003; Raupach, 2005; Raupach et al., 2007)

However, the comparison of these two measuring techniques can only estimate the correctness of the values. The resistance can be measured with a resolution of 0.01 Ω up to values of 20 Ω and with a resolution of 0.1 Ω over this value. Figure 4.14 shows a part of the data transmission of the measuring values of the demonstrator.

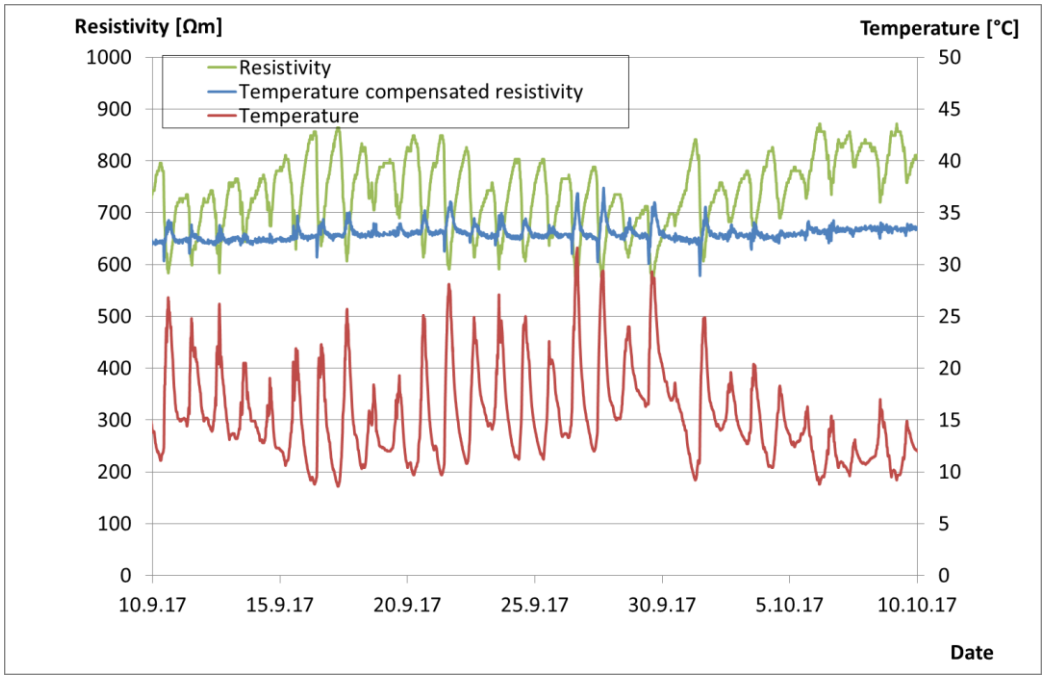

Figure 4.14. Temperature, resistivity, and temperature-compensated resistivity of one measuring field

Recorded are the resistance values, the temperature, and the temperature compensated resistance values. It can be seen that the resistance values follow the temperature fluctuations over the day, which shows a good sensitivity of the measuring technique. Furthermore, this ensures that no exists between the two carbon layers, which could be the case when the two carbon layers are pressed together during the mortar pouring. During the few test months of the demonstrator, only a slow increase in the resistivity values could be observed showing the desiccation of the plate. Due to the high-water content of the fresh mortar a leakage detection was not yet possible.

Therefore, a second demonstrator on a newly constructed bridge was realized in 2019. The resistivity values will be measured over years, and the measuring technique will be tested for the first time under actual traffic conditions. The second modification compared to the first demonstrator is the power supply, which will be ensured with a solar panel placed near the bridge construction. So even on bridges where no electricity grid is available, SMART-DECK can be applied. The cables from the carbon layers are led over a short distance to the solar panel and a measuring box. On the pole of the solar panel, a module is attached, which provides the measuring data from the bridge via LoRa-technique (Long Range Wide Area Network) to a computer placed in a nearby building. From there, the data can be accessed via a remote connection, see Figure 4.15.

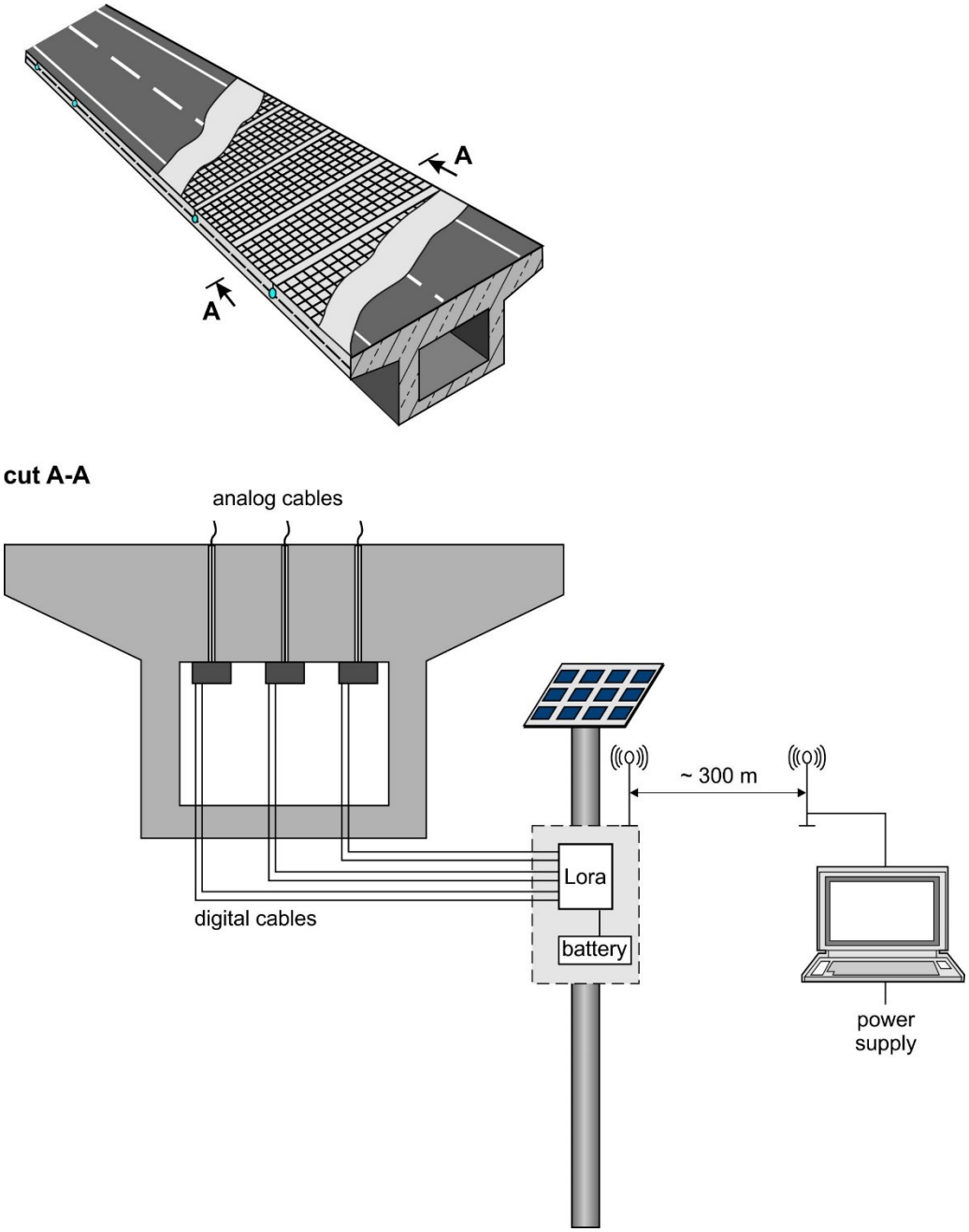

Figure 4.15. Data transmission

As in the first demonstrator, temperature sensors and multiring sensors were installed. The measuring technique, the solar power supply, and the data transmission with LoRa have been tested on the university ground and will be started at the demonstrator bridge in the following weeks.

4.1.4.5 Further Functions of SMART-DECK

Cathodic Prevention

If the monitoring data show a leakage in the bridge deck sealing that cannot be repaired immediately, the cathodic prevention is switched on. In this case, the carbon layers serve as an

impressed current anode. The prevention of chloride-induced steel corrosion in concrete through impressed current is established nowadays. (Baeckmann et al., 1997; *DIN EN ISO 12696*, o. J.; Eichler & Gieler-Breßmer, 2018)

The suitability of carbon textiles as an impressed current anode has been investigated, e.g., by (Asgharzadeh, 2019). Potentiostatic tests showed that carbon textiles deliver a constant current over the investigation period and cathodic protection with carbon textiles is possible without destruction of the carbon as long as a polarization of the anode of more than 2200 mV vs NHE is excluded.

While cathodic protection is used for structures already affected by chloride-induced corrosion, cathodic prevention is used for systems that will presumably be contaminated by chlorides. (Bertolini et al., 2013)

Cathodic prevention relies on the fact that the critical chloride threshold increases as the potential of steel decreases. So even very low current densities (<2 mA/m^2) polarize the reinforcement to values in which steel works under conditions of “imperfect passivity” so that initiation of pitting is prevented even if high levels of chlorides accumulate at the surface of the steel by penetrating through the cover concrete. (Bertolini et al., 2009, 2013)

The cathodic prevention was tested on the first outdoor demonstrator to realize different protection zones with varying reinforcement ratios. In accordance with (Raupach, 1992), the effect of the cathodic prevention was tested in carrying out a depolarization measurement. The anodic potential shift after a 24-hour-disconnection of the power supply was higher than 150 mV, indicating that the carbon textiles embedded in the selected mortar are a suitable anode system. SMART-DECK's first and second outdoor demonstrators are one of the first large-scale testing areas for cathodic protection systems with carbon reinforcement. By now, the functionality of carbon as an impressed current anode in concrete was only tested on small specimens as in (Asgharzadeh, 2019).

Strengthening

The third function was investigated at the Institute for Structural Concrete of the RWTH Aachen University. The strengthening effect was examined concerning its flexural and shear capacity. With tests on small-scale specimens, the load-bearing properties of different combinations of the textiles and mortar were investigated. Therefore, reinforced concrete slab segments were strengthened with a carbon-reinforced concrete layer. The load position and the tensile reinforcement ratio were varied for investigating the bending and shear capacity. The influence of the additional layer on crack formation and capacity was examined. The investigations showed that strengthening bridge deck slabs with SMART-DECK is possible. (Herbrand et al., 2017)

Regarding the bending strength, a duplication of the bearing capacity was achieved, and concerning the shear force capacity, an increase of 23,5 % and 56 % was reached. (Büttner, 2020)

4.1.5 Conclusion and Outlook

The described investigations and results can be summarized as follows:

- The numerical simulations showed that leakages of a few percentages of the total field size are detectable with the single-layer-set-up or the standard structure of SMART-DECK.
- Laboratory tests proved the simulated detectability of artificial leakages through resistance measurement
- The measuring technique and data transmission was tested on the first demonstrator and installed under actual traffic conditions on a natural bridge construction

SMART-DECK will be tested with an alternative power supply in the following months.

On the scientific side, the question of which potential gradients are necessary to prevent chloride ions from migrating into the matured concrete and from damaging the reinforcing steel is investigated. The negatively charged chloride ions will be held on the carbon mesh, which is polarized as an anode by applying an electrical field between the carbon meshes and the steel. It could be possible that the resulting current densities are smaller than they have to be for the standard (preventive) cathodic protection so that an electrochemical chloride barrier is implemented. Therefore, laboratory tests and numerical simulations were carried out for materials with different diffusion resistances and with different potential gradients. The results will be presented in publications in the following months.

5 Simulations for the Detection of Leakages through Resistivity Measurements

5.1 Numerical Simulations for the Detection of Leakages in Bridge Deck Sealers through Resistivity Measurements

5.1.1 Abstract

By measuring the electrolyte resistance between two carbon meshes embedded in a textile-reinforced concrete interlayer on bridges, large-scale humidity monitoring is implemented. The electrolyte resistance is measured using an alternating current. Decreasing values in the measured electrolyte resistance indicate water ingress through leakages in the bridge deck sealer.

The monitoring will positively affect the durability of a bridge structure since defects in the sealer can be detected in an early stage, which allows cost-effective and timely measures to be taken to prevent corrosion initiation of the reinforcing steel.

Through numerical simulations, the theoretical size of a detectable leakage area is calculated, which depends on the geometry of the leakages, the electrolyte resistance of the mortar in wet and dry conditions, the position of the leakage, and other boundary conditions.

5.1.2 Detection of Leakages through Resistivity Measurements

Leakages in sealers applied on concrete bridge decks commonly threaten the structure's durability as water and dissolved chloride ions can easily permeate into the concrete cover, which may eventually lead to corrosion of the steel reinforcement. In practice, leakages often remain largely unnoticed until corrosion damage is observed on the external surfaces. In this stage, it is already costly to repair these damages to the structure. For more proactive maintenance of bridges, the idea of full surface humidity monitoring was developed, which is intended to transmit the relevant data in real-time. Until now, only sensors which measure selectively at the point of installation are available. (Raupach, 2005; Raupach et al., 2013) For a full surface humidity monitoring, the resistance between two carbon meshes having an in-between spacing of 15 mm is measured. The measured resistance can then be converted into a resistivity which allows a quantification of the moisture content to assess the occurrence of leakage. The resistivity of concrete may vary over a wide range with resistivity values of about 106 Ωm for dry concrete, whereas water-saturated concrete is characterized by an electrolyte resistivity of approximately 100 Ωm. (Raupach et al., 2003b)

5.1.2.1 Relationship between Moisture Content and Resistivity

Knowing the exact relationship between moisture content and resistivity values of a specific mortar and detecting a change in the electrolyte resistance, one can estimate the amount of water permeating the structure. The relationship between moisture content and mortar resistivity can be investigated in laboratory tests under well-defined conditions.

Mortar specimens are stored underwater for laboratory investigations until full saturation is achieved. In this condition, the electrical resistance and the weight of the specimens are measured. The resistance is measured with a two-electrode set-up, and the specimens are dried at 70 °C until low moisture contents are obtained. When such a condition has been achieved, a wide variety of moisture contents are being adjusted by adding different amounts of water. Following this treatment, the specimens are packed vapor resistant to reach a homogenous water distribution. After a few weeks-reinforced, the specimens are unpacked and weighed. In addition, the electrolyte resistance is being measured. Eventually, the specimens are dried at 105 °C until a constant weight is achieved, and this dry weight is measured. Based on these data, the relationship between moisture content and resistivity values can be calculated. (Driessen & Raupach, 2015b) This requires the conversion of an AC resistance into a resistivity which is achieved using a cell constant according to Eq. 5.1 (Kaufman, 2000).

$$\rho = \mathrm{R_{el}} \cdot \frac{\mathrm{A}}{\mathrm{l}} \qquad 5.1$$

With:

- ρ: mortar resistivity [Ωm]
- R_{el}: measured resistance [Ω]
- A: cross-sectional area of the mortar specimen [m^2]
- l: distance between the electrodes in m

Having determined the resistivity values with the corresponding moisture contents, a regression analysis is carried out using the following regression function (2) (Harnisch, 2003):

$$u = \frac{A}{\ln(B \cdot \rho + C) - D} + E \qquad 5.2$$

With:

- u: moisture content referred to the mass of mortar [M.-%]
- ρ: mortar resistivity [Ωm]
- A-E: regression parameters

This regression curve is based on an empirical formula derived by (Brameshuber et al., 2003). Figure 5.1 shows the measured values and the calculated regression curve. This regression curve serves as the primary input for the numerical simulations.

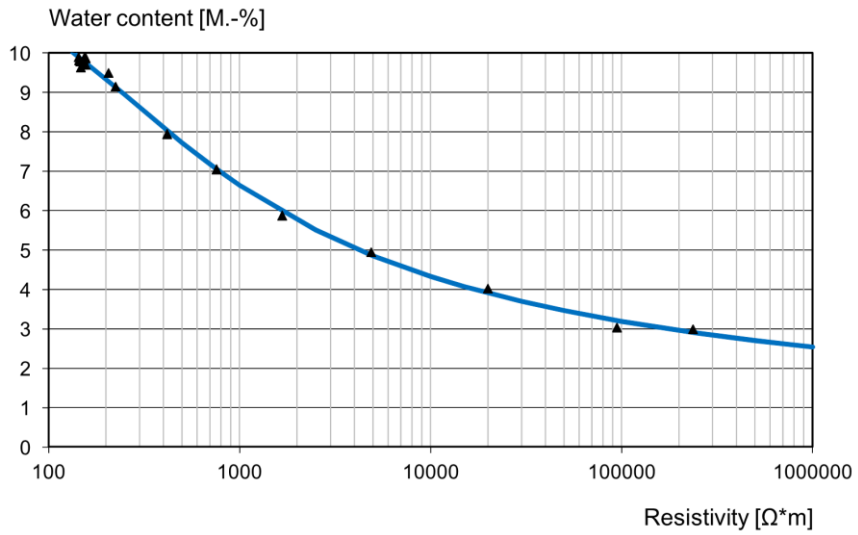

Figure 5.1. Calculated relationship between water content and resistivity

For the numerical simulations, values ranging from zero to 1000 Ωm represent the wet mortar in the leakage zone, and values above 1000 Ωm are representative of the mortar in a dry state under an intact sealer. Of course, there is not a precise threshold level that separates between the wet and dry conditions of a mortar but a gradual transition depending on the conditions for desiccation, such as temperature, humidity, and the presence of a sealer. However, these influencing parameters were not part of the numerical simulations but will be examined in laboratory tests later in the project. Preliminary tests show that after a few months of desiccation, the specimens reach water contents between 6 -7 M. -%, which is demonstrated by resistivity values of about 1000 Ωm.

5.1.3 Numerical Model and Parameter Study

The interlayer arrangement applied on bridge decks was transferred to specimens with a cross-section of 30 by 30 cm2 for laboratory testing. (Driessen & Raupach, 2015b) These specimens serve as the model for the numerical simulations. This downscaled model enables shorter calculation times. Under real conditions, the measurement areas on bridge decks will be about 5-10 m^2. In the following, the results will be given in relative sizes to transfer the results to all possible geometries. The interlayer arrangement is built up of a 10 mm mortar bottom layer, serving as the contact zone to the matured concrete. On this bottom layer, two carbon meshes with an in-between spacing of 15 mm are placed. Each carbon mesh is embedded in a cement-

based mortar. The top layer consists again of 10 mm mortar. Both carbon meshes have a mesh size of 38 mm. The basic model is shown in Figure 2 with a leakage zone in the center.

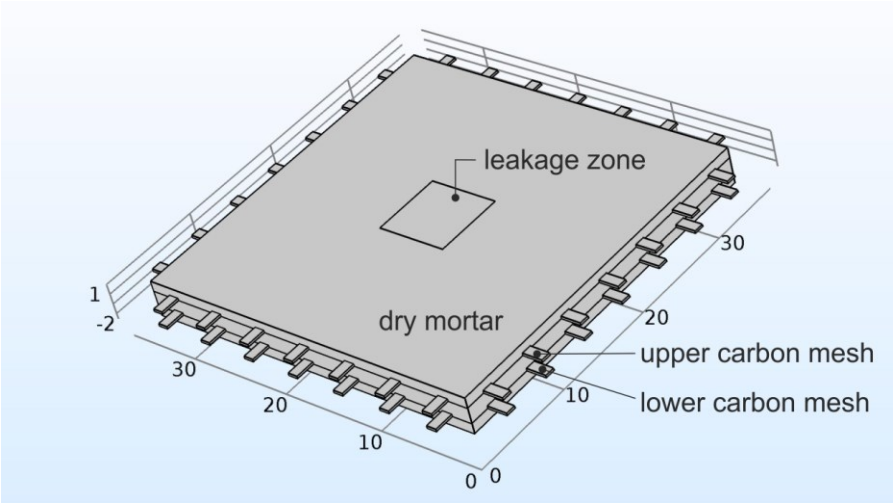

Figure 5.2. Basic model with a leakage zone in the center

Between the upper and bottom carbon mesh, a fixed AC voltage is applied with the lower carbon mesh connected to the ground. In the following, the system of the two carbon meshes is called “anode” to distinguish it from the reinforcement steel in the bridge deck, which acts as the cathode. However, this is not treated in the present paper. The voltage applied can be chosen arbitrarily since various voltages lead to different currents at constant resistance, the parameter of interest, provided that no polarization of the carbon meshes occurs. This assumption is justified because the resistivity will be measured with alternating current. The resistivities for the mortar in wet and dry conditions are the input values for the numerical simulations, resulting in respective values for the conductance as an output. To determine the resistivity, the geometry factor for the system with the mesh anode was first calculated as dependent on both the specimen size and the roving quantity. The resulting regression curve for the geometry factor is depicted in Figure 5.3. This conversion from resistance into resistivity is essential for comparing the numerical results because only the resistivity is corrected for geometry effects.

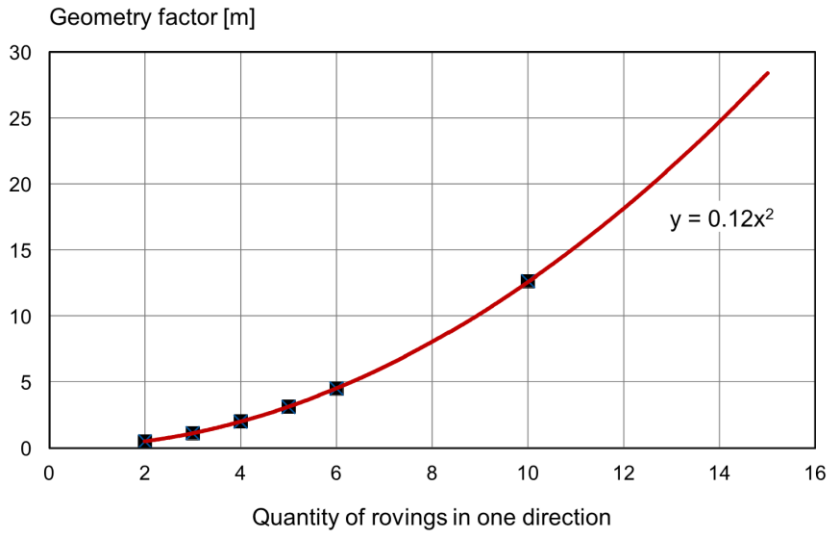

Figure 5.3. The form factor for the numerical model depending on the model size

The majority of the numerical simulations were carried out with the arrangement and geometry of the model shown in Figure 5.2, which corresponds to a roving quantity of seven in each direction and a geometry factor of 6.15 m. Moreover, numerical simulations with a model size of 10 m² were calculated for comparison. The results of both models given in relative sizes matched with a negligible difference of 0.17 %. Thus, the assumption that the results can be transferred to all possible measuring fields seems to be correct.

Investigated Parameters

The main issue to be resolved through numerical simulations is which size of a local defect in a sealer can be detected at which resistivity values of the wet mortar are located in the leakage zone and at which resistivity values of the dry mortar under an intact sealer. Moreover, the shape, dept, and position of the leakage in the measuring field could influence the measured drop in the resistivity values. Another question is whether there is a difference between the situation in which just a single leakage at a time occurs and the situation that numerous smaller leakages occur nearly at the same time, which are distributed over the measuring field. In addition, it was examined if the simplification of the mesh anode to a flat full surface anode is allowed concerning the resulting error. Table 5.1 provides an overview of the varied parameters.

Table 5.1. Varied Parameters

	Dimensions	Range
Size of the leakage zone	% of the total field	1-100

Resistivity of the leakage zone	Ωm	150; 250; 500; 700
Resistivity of the dry mortar	Ωm	1000; 5000; 7000; 100000
Depth of the leakage	cm	1-3
Position of the leakage	-	center; edge
Number of leakages	-	1; 4; 9
The shape of the leakage	-	cubic; cylindrical
Shape of the anode	-	mesh; flat

5.1.4 Results of the Numerical Simulations

First, the spatial distribution of the electrical current was expressed as a current density, and the flow direction of the applied current was plotted. Due to the relatively low resistivity of the leakage zone, it is logical that the current flows in the direction of the leakage zone, as exemplified in Figure 5.4.

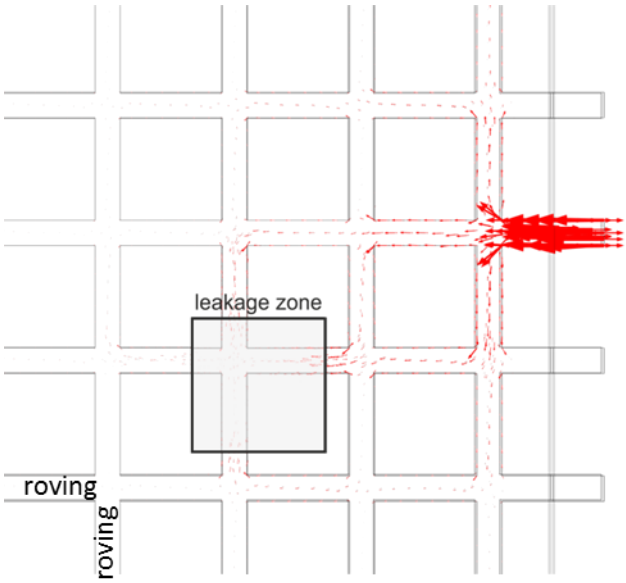

Figure 5.4. The flow of the resulting electrical current

Accordingly, the current densities in areas nearer to the leakage zone are higher. This can be observed in Figure 5.5 on the left side, which shows a view from above. On the right side, one can see a sectional view between the two carbon meshes. Only in the leakage zone increased current densities appear, so the majority of the applied current will flow through the leakage.

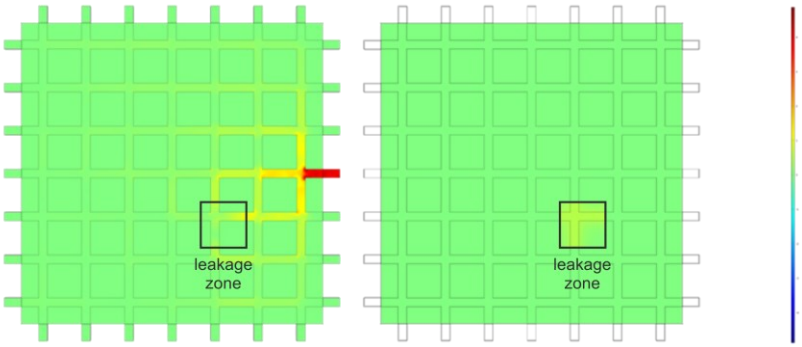

Figure 5.5. Current densities are shown from above (left) and between the carbon meshes (right)

5.1.4.1 Influence of Different Resistivities and Sizes

In the first simulations, the resistivities for wet and dry conditions of the mortar and the size of the leakage were varied. Figure 5.6 shows four combinations of resistivity values, starting with the smallest difference between resistivity values in wet and dry conditions up to the greatest difference shown at the bottom.

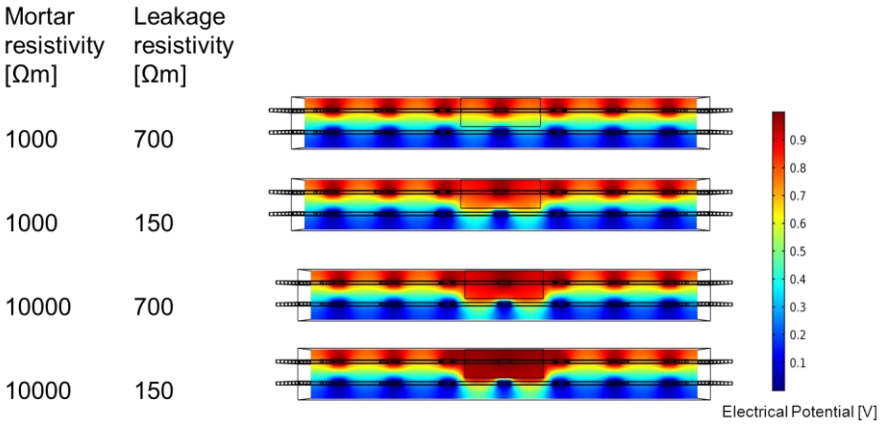

Figure 5.6. Distribution of the potential for different mortar resistivity combinations.

As an example, Figure 5.7 shows the calculated drop in mortar resistivity for various leakage resistivities based on a dry mortar resistivity of 1000 Ωm under an intact sealer. According to the numerical simulations, this is the resistivity that can theoretically be derived with the measuring technique.

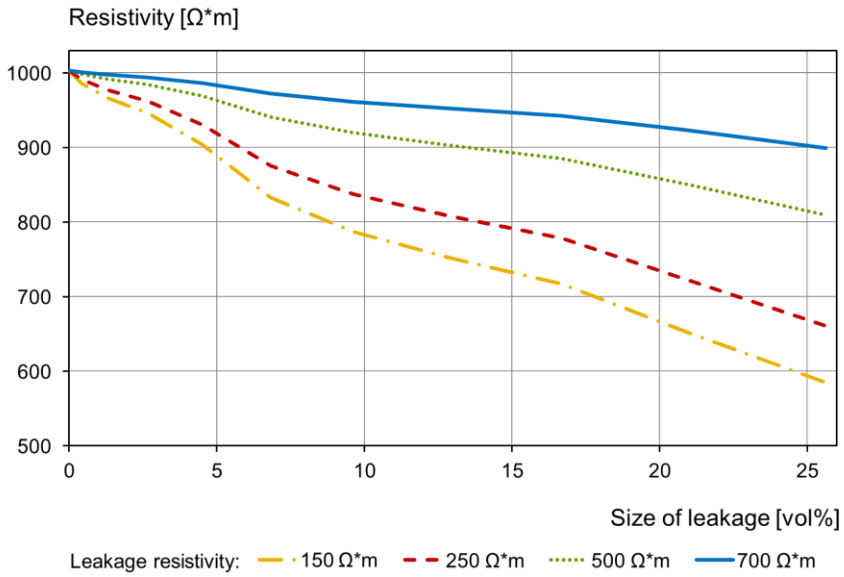

Figure 5.7. Drop-in resistivity values caused by different mortar resistivities in the leakage zone

The larger the leakage, the easier it will be detected by the decrease in resistance. Secondly, the lower the resistivity of the leakage zone, the easier the leakage can be found. From Figure 5.7 it can be deduced that leakages with the size of a few percentages of the total field size are detectable. The depicted case is the one with the harshest conditions for the detection of leakages being investigated. All other cases show higher resistivities of the dry mortar and, therefore, larger drops in resistivity caused by the leakages. For better comparison, the resistivity is shown in Ωm. The resistance in Ω depends on the field size. The smaller the measuring field, the larger are the measured drops, and the easier leakages are detected.

All curves show some bends caused by the mesh structure of the anode.

Figure 5.8 shows the resistivity decrease for different resistivity combinations of wet and dry mortar.

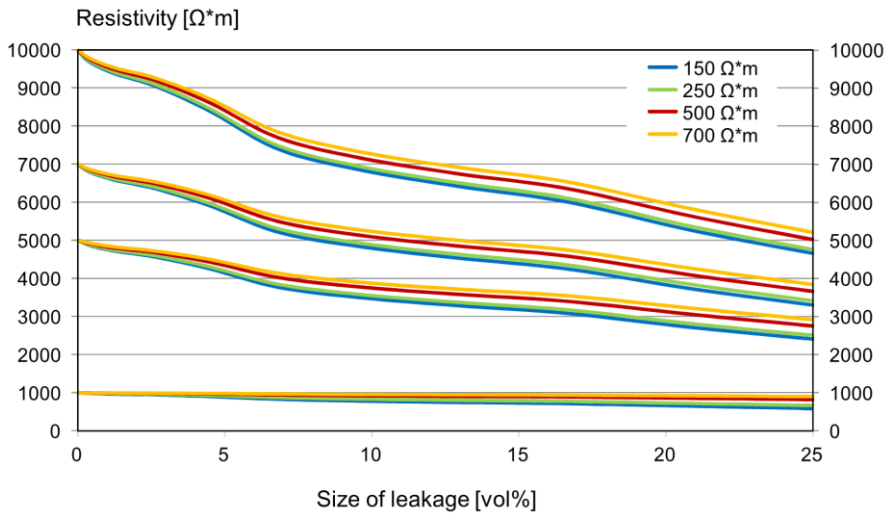

Figure 5.8. Drops in resistivity with 150, 250, 500, and 700 Ωm leakage resistivities and 1000, 5000, 7000, and 10000 Ωm resistivities of the dry zone

It becomes evident that the resistivity of the dry measuring field has a higher impact on the detectability of leakages than the resistivity of the leakage zone. The differences between the different resistivity values of the measuring fields can be recognized, while the differences between the leakage resistivities are very small. Under natural conditions, effects like fluctuations in temperature or humidity could even overlay these. This results from the fact that the regression curve of moisture content versus resistivity follows a logarithmic relationship. There is just a small spectrum in which values representing a wet condition vary however, a large range exists of possible values representing a dry condition. As a consequence, for the application on a bridge deck, it is necessary that a mortar demonstrating high resistivity values in a dry state is used and that the mortar will be given some time to dry out before a reliable detection of leakages is possible. On the other hand, even small amounts of water which permeate into the interlayer can be detected under these circumstances.

5.1.4.2 Influence of the Leakage Depth

Besides the size of the defective sealer and the resistivity of the mortar under the defective sealer, and the resistivity of the remaining field, other parameters could influence the detectability of leakages. The first parameter considered is the depth up to which water has penetrated the interlayer. Figure 5.9 shows resistivity values for a leakage depth of 1 cm to 3 cm. The actual measuring field starts at a depth of 1 cm and ends at a depth of 2.275 cm, which is the space between the two carbon meshes (here shown by the coloured area). As an example, the mortar resistivity of 10000 Ωm and a leakage resistivity of 150 Ωm and 700 Ωm are plotted as a function of the leakage depth.

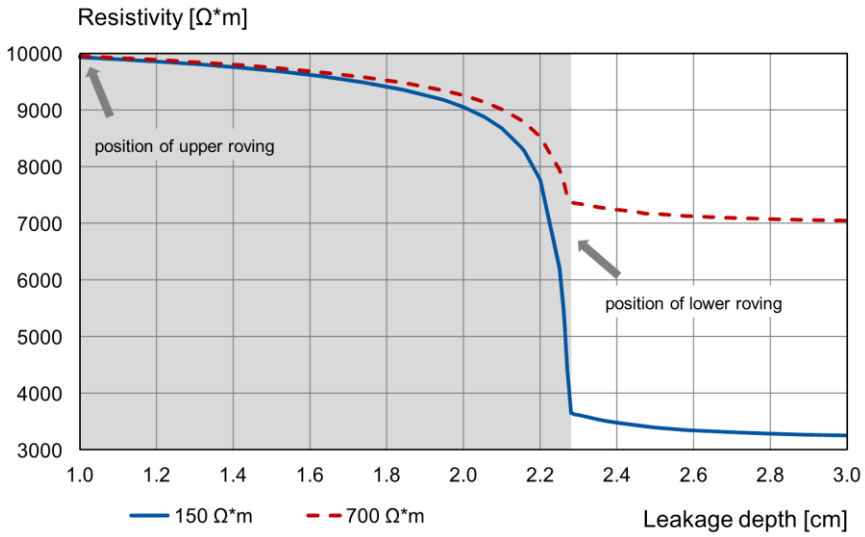

Figure 5.9. Influence of the leakage depth based on calculated results obtained from numerical simulations

The resistivity decreases with the depth of the leakage. Notifiable is the sharp drop in resistivity values when the leakage has nearly reached the lower carbon mesh, however, without touching it. This is probably because almost a low resistance path between the upper and lower carbon mesh is produced in the leakage zone. The zone with higher potentials is not strictly limited to the leakage itself but expands behind the leakage, as shown in Figure 5.6. Consequently, resistivity values drop quickly before the second carbon mesh is reached. The curve flattens as soon as the lower carbon mesh is reached. The flattening graph results from the use of a mesh-type anode. If a continuous flat plate anode would have been modelled, the graph would show constant values after reaching the second carbon mesh. Here, because of the open mesh structure of the anode, the flow lines of the current partly reach the backside of the mesh and lead to slightly decreasing resistivity values behind the extent of the second carbon mesh. For usage on a bridge deck, this means that water which seeps under a sealer but does not penetrate sufficiently deep to enter the mortar will be hard to detect. However, it can be assumed that if the mortar is dried out, the leakage water will be absorbed soon and moisture penetration to greater depth seems likely.

5.1.4.3 Variation of Further Parameters

In the following steps, the remaining parameters shown in Table 5.1 are investigated. It became apparent that the shape of the leakage, e.g., cubic or cylindrical, the position of the leakage in the measuring field, and the number of leakages (compared to a reference leakage with the accumulated size of the variety of smaller leakages) just have a negligible influence

on the detectability. This is exemplified in Figure 5.10 for a dry mortar resistivity of 5000 Ωm and the case that the leakage depth is at a maximum of 3 cm.

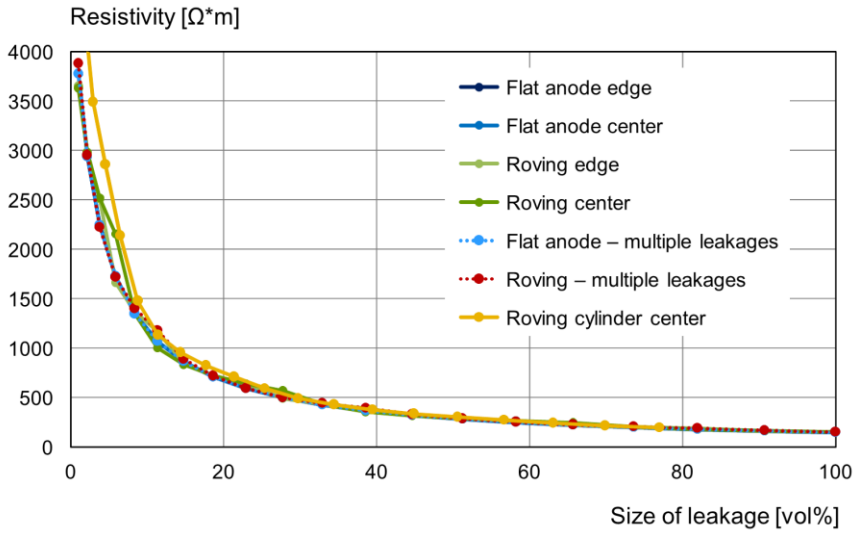

Figure 5.10. Parameters with negligible impact on the detectability of leakages

The differences in resistivity for the smaller leakage sizes result from a different amount of anode material in the leakage zone. Under the condition of very small leakages, the shape of the leakage and the mesh structure of the anode lead to relatively high differences in the amount of anode material touched by the leakage and, therefore, to different resistivities. At higher leakage sizes, this impact becomes smaller.

Only the geometry of the anode affected the drop in resistance values, but merely if the leakage depth has not already reached the second carbon mesh. Figure 5.11 shows this effect. In contrast to Figure 5.10, where all parameters were investigated under the condition that the leakage depth covers the entire measuring depth up to the second carbon electrode, Figure 5.11 shows a leakage depth of 2 cm. In this case, a short circuit is not considered realistic. Here, the geometry of the anode affects the drop in resistivity. While flat anodes lead to low spreading resistances, more discrete anodes generally result in higher resistances. As a consequence, the mesh anode will lead to lower drops in resistivity values. (Raupach, 1992)

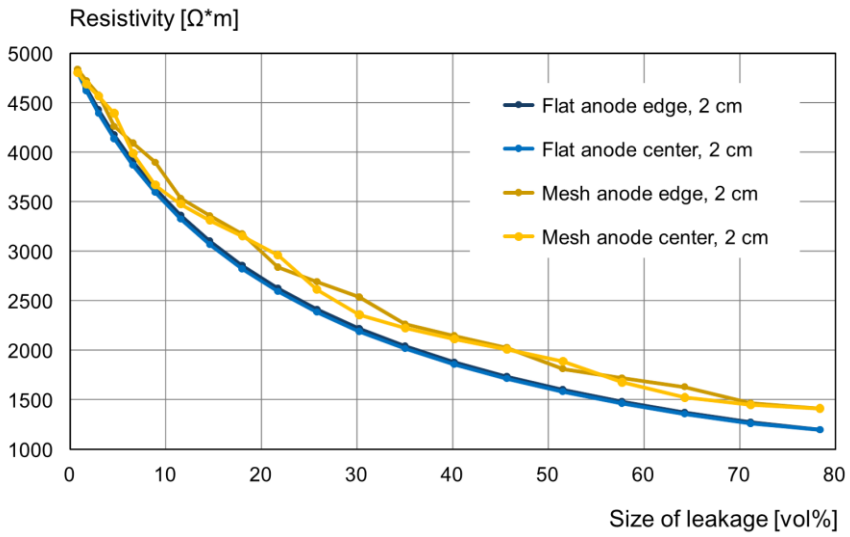

Figure 5.11. Impact of the anode structure in combination with the leakage depth

However, small over-or underestimates of resistivity drops are not critical for detecting leakages. There will always be various measuring fields nearby, so the changes in resistance values can be seen relative to the neighbouring measuring fields. Thus, it is possible to adjust if an actual leakage occurs or if other boundary conditions lead to the measured change in values.

5.1.5 Conclusions and Outlook

Based on the findings of the numerical simulations, the following conclusions can be drawn:

- Leakages having a limited size of a few percentages of the total surface area are detectable
- Resistivity values of a mortar located under an intact sealer in a dry environment must be high compared to the resistivity values obtained for a water-saturated condition which means that leakages can be detected as soon as some desiccation of the mortar proceeded.
- The main impacts of various boundary conditions on the detectability of leakages were demonstrated

This paper focused on the theoretical aspects regarding the detection of leakages. Nevertheless, as mentioned before, parameters like temperature and humidity have an additional effect on the actual detectability of leakages under natural conditions. Therefore, additional laboratory tests will be carried out under different climatic conditions and temperature compensation. Furthermore, the theoretical results will be validated under practical conditions on a demonstration panel with a size of about 100 m² by artificially produced leakages.

6 Experimental and Model-Based Investigations of the Chloride Barrier

6.1 Application of Electrical Fields to Reduce Chloride Ingress into Concrete Structures

6.1.1 Abstract

In the context of a joint research project, a system for monitoring, protecting, and strengthening bridges using a textile-reinforced concrete interlayer has been developed, consisting of two carbon layers with a spacing of 15 mm and a special mortar. This setup led to the idea to build up an electrical field between the carbon meshes, which suppresses the ingress of chlorides into the concrete. This paper focuses on the question of which voltages and electrical field strengths are necessary to prevent critical chloride contents at the reinforcing steel. For this purpose, extensive laboratory tests have been performed, followed by a numerical simulation study.

By applying an electrical field, the negatively charged chloride ions are forced to move to the upper carbon mesh that is polarized as an anode. It has been investigated whether the voltages to implement an electrochemical chloride barrier are smaller than they have to be for the common preventive cathodic protection. One advantage of this chloride barrier is that the anodic polarization of the carbon meshes can be reduced because of the lower current densities. Therefore, different voltages, electrical field strengths, anode materials, and anode arrangements were investigated.

6.1.2 Introduction

Due to de-icing measures, bridges are often threatened by chloride ions which penetrate the concrete and cause corrosion of the reinforcement and thus threaten the durability of the construction. The corrosion of the reinforcement can only be seen visually when a high degree of impairment is already reached. (Cady & Weyers, 1983; P. Schießl & Raupach, 1993)

Comprehensive building operations are necessary, leading to traffic obstructions and thus to economic losses. (R. Polder et al., 2016)

Therefore, in a joint research project, the interlayer SMART-DECK was developed. The interlayer provides three functions: all-over real-time humidity monitoring, preventive cathodic corrosion protection, and strengthening the shear force. When the sealing starts to leak and water permeates into the interlayer, a drop of the measured electrical resistivity is detected, and the operator of the bridge construction receives a note about the leakage. If an event of damage in the seal is being detected, the cathodic corrosion protection can be switched on. Thus, the constructional measures of the bridge deck sealing can be postponed to periods with less

traffic or to that point of time when a renewal of the sealing is planned anyway. An electrical field is generated between the carbon meshes with a rectifier, which reduces chloride diffusion into the construction. Thus, the depassivation of the steel is prevented. (Driessen & Raupach, 2015b; Driessen-Ohlenforst et al., 2020)

This article focuses on using the electrical field as an electrochemical chloride barrier. Figure 6.1 shows the chloride ingress without the electrical field on the left side and the expected qualitative chloride profile with an electrical field on the right side.

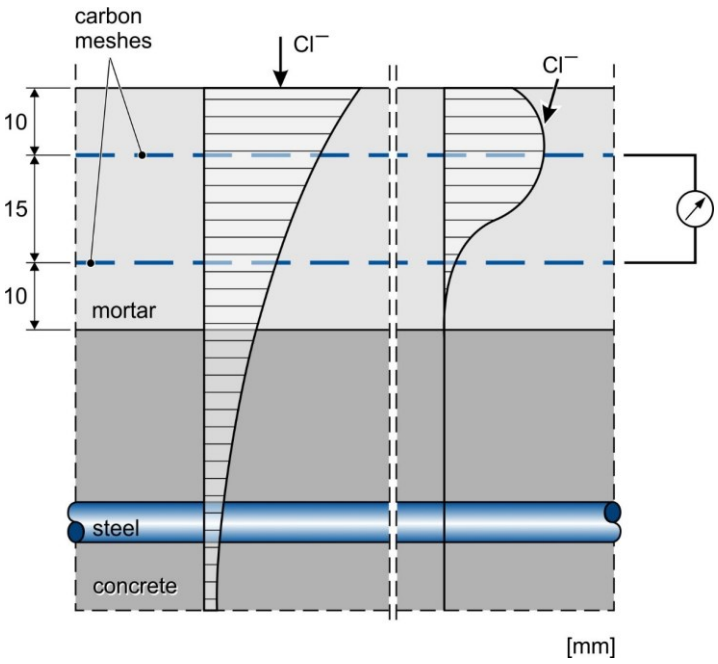

Figure 6.1. Qualitative Schematic diagram of the chloride ingress without (left side) and with (right side) the electrochemical chloride barrier

6.1.3 Theoretical Background

The prevention of chloride-induced steel corrosion in concrete through impressed current is established nowadays. (Baeckmann et al., 1997; *DIN EN ISO 12696*, o. J.; Eichler & Gieler-Breßmer, 2018)

The suitability of epoxy-impregnated carbon textiles as an impressed current anode has been investigated, e.g., by (Asgharzadeh, 2019). Potentiostatic tests showed that the investigated carbon textiles deliver a constant current over the investigation period and cathodic protection with carbon textiles is possible without destroying the carbon for the investigated impregnations as long as a potential of the anode more than 2200 mV vs NHE is excluded.

While cathodic protection is used for structures already affected by chloride-induced corrosion, cathodic prevention is used for structures that will presumably be contaminated by chlorides. (Bertolini et al., 2013)

Cathodic prevention relies on the fact that the critical chloride threshold increases as the potential of steel decreases. Even current densities which are lower than the current densities usually used for cathodic protection (< 2 mA/m^2) polarize the reinforcement to values in which steel is under conditions of “imperfect passivity” so that initiation of pitting is prevented even if high levels of chlorides accumulate at the surface of the steel by penetrating through the cover concrete. (Bertolini et al., 2009, 2013)

The method described in this paper goes a step further and refers to the question of whether common voltages for the cathodic prevention are sufficient or can even be reduced if it is the aim to prevent chloride ingress from the beginning so that an electrochemical chloride barrier is implemented. A similar term, namely “cathodic protection barrier”, was used before in another project (Bruns & Raupach, 2009), but was instead used to describe a form of cathodic prevention where the corrosion potential of the passive reinforcement is polarized in such a way, that the reinforcement cannot form the cathode of the macro-element anymore. In contrast, due to the full-surface real-time monitoring, in this work, the opportunity exists to apply an electrical field that works against the diffusion and convection of the chlorides right from the beginning to prevent chloride ingress. By now, other scientific investigations focus on the question of protecting the steel despite the presence of chlorides or removing chlorides that are already in the concrete. (Eichler et al., 2010) Therefore, usually, voltages of a minimum of 2 Volts are used. Other literature focuses on the question of using chloride migration to pull chlorides through a specimen to conclude other concrete parameters such as diffusion coefficients. (Luping & Nilsson, 1993; Tang, 1996; Tang & Nilsson, 1997)

The electrochemical chloride barrier can be applied in two different variants. By default, the interlayer includes two carbon layers, see Figure 6.1. In between those, the resistivity is measured, and in case of occurring leakages, the voltage is applied. Though, if no structural strengthening is needed, it is also possible to use only one carbon mesh to gain a thinner layer and reduce costs. In this case, the resistivity is measured between the one-carbon mesh and the reinforcement. Here, the electrical field is applied between the carbon mesh and the reinforcement, which is usually done for cathodic prevention or protection.

Despite different focuses in other research works, the transport processes of the chlorides are naturally the same, namely diffusion, convection, and migration. Here, diffusion refers to the movement of chloride ions from higher concentration regions to lower concentration regions. Migration or electro-migration means the movement of chloride ions due to an electrical field. Convection occurs due to the chloride ions being carried along with the fluid. The latter can be neglected if the specimens are water-saturated. These transport mechanisms can be described by the Nernst-Planck-equation. (Atkins & De Paula, 2013)

In the present case, the structure of the specimens makes it necessary to distinguish two areas of the specimen, see Figure 6.2.

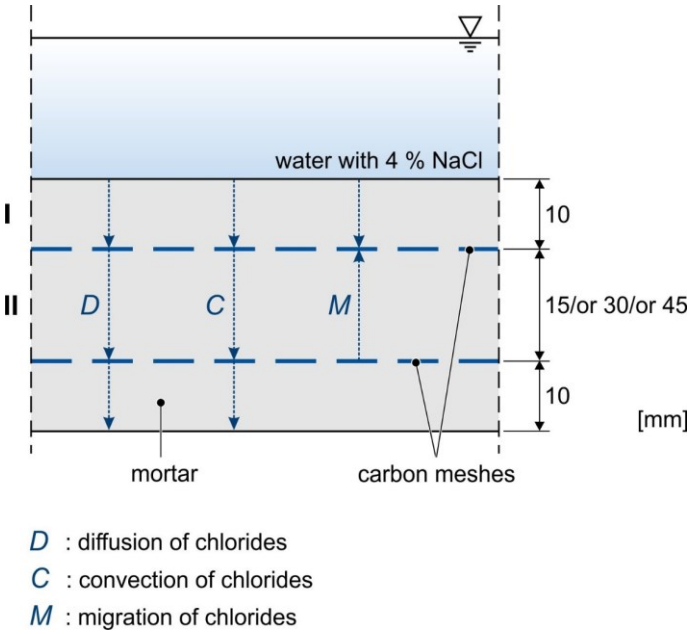

Figure 6.2. Transport processes of chlorides in the specimens used within this work

In area I, all transport processes work in the same direction, while in area II, the actual chloride barrier appears with the migration working against the diffusion and convection of the chlorides into the mortar. This leads to Eq. 6.1 for area I and Eq. 6.2 for area II.

$$J = -D_{eff} \cdot \frac{\partial c}{\partial x} + v \cdot c + u_m \cdot c \qquad 6.1$$

$$J = -D_{eff} \cdot \frac{\partial c}{\partial x} - v \cdot c + u_m \cdot c \qquad 6.2$$

With:

J: Molecular flow [mol/(m²s)]

D_{eff}: Diffusion coefficient [m^2/s]

v: Mean migration speed in the electrical field [m/s]

u_m: Mean mass velocity [m/s]

c: Concentration of chloride ions [mol/m^3]

6.1.4 Experimental Investigation

6.1.4.1 Testing Procedure

The test procedure is divided into two main series. One series of mortar specimens was water-saturated before starting the measurements, and the other series was dried. Thus, the dried specimens allow an additional view of convection apart from the mechanisms of diffusion and migration. In each series, the applied voltages to generate an electrical field and the distances in between the electrodes were varied, resulting in different electrical field strengths. By

doubling the voltages while simultaneously doubling the anode distance, the electrical field strength can be held arithmetically constant, and the question of whether effects depend on absolute voltages or electrical field strengths can be investigated. The aim was to test voltages that are not harmful to the structure of the carbon meshes, which is why 2V was applied as the maximum external voltage. As mentioned before, previous research showed that this voltage leaves the carbon meshes unaffected. In addition, 1 V and 0.5 V were applied as external voltages. The external voltage consists of voltage drops at the surface of the carbon electrodes and the voltage drop within the concrete (IR), which is referred to as “electrolyte voltage” in the following. In the following diagrams, the electrolyte voltages will be mentioned instead of the externally applied voltages because these determine the actual electrical field.
The focus lies on carbon meshes as an anode material. Nevertheless, some reference tests with titanium meshes were carried out. Table 6.1 gives an overview of the varied parameters.

Table 6.1. Test Program

Series	Anode Material	External voltages in V	Anode distance in mm	Amount	Total amount	Reference specimens (with 0 V)
Water-saturated specimens	Carbon	0.5	15	3	27	12 (4 for each anode distance)
			30	3		
			45	3		
		1	15	3		
			30	3		
			45	3		
		2	15	3		
			30	3		
			45	3		
	Titanium	2	15	3	9	
			30	3		
			45	3		
Dried specimens	Carbon	0.5	15	3	27	12 (4 for each anode distance)
			30	3		
			45	3		
		1	15	3		
			30	3		
			45	3		

		2	15	3		
			30	3		
			45	3		
	Titanium	2	15	3	9	
			45	3		
			45	3		

6.1.4.2 Materials and Test Set-up of the Specimens

For the experiments, specimens with a surface area of 20 cm × 20 cm or 10 cm × 10 cm for the reference specimens were cast. The heights of the specimens varied with the distance between the anodes. Above and below the anodes, a mortar covering of 10 mm was produced. Figure 6.3 shows the anode meshes with spacers and electrical connections before embedding them in mortar.

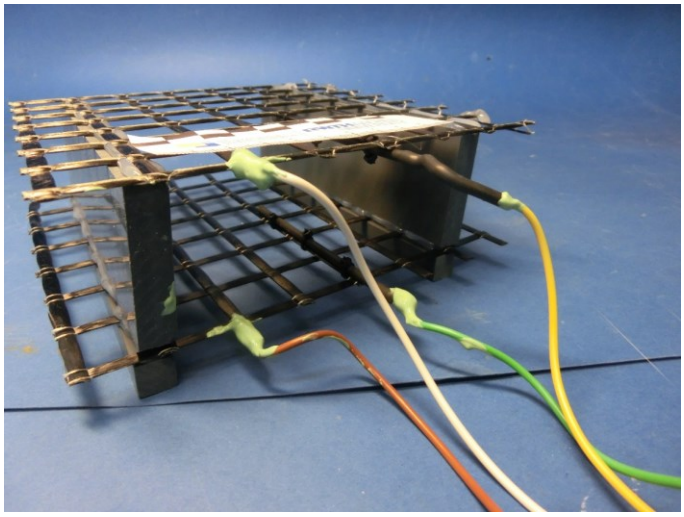

Figure 6.3. Carbon meshes with spacers and electrical connections

A porous composition was used for the mortar to ensure feasible testing times. Because the laboratory tests aimed to investigate the effect of the chloride barrier and not the material testing, results and insights are transferable to other mortar compositions. Table 6.2 shows the composition and other characteristics of the mortar in the experiments. A Polymer-modified Cement Concrete with a maximum aggregate size of 4 mm is used for the actual application on a bridge.

Table 6.2. Composition and characteristics of the mortar

Material	Kg/m^3	Resulting parameters
Cement CEM1	363	Flow spread: 146 mm

Water	254	Density: 2.169 kg/l Air void content: 3.5 % w/c-ratio: 0.7
Sand 0.1-0.5	706	
Sand 0.5-1.0	403	
Sand 1.0-2.0	443	
Total	2169	

After curing the specimens, water basins were applied on top of the specimens containing a homogeneous solution of 4 % NaCl (0.7 mol/l) that was refilled regularly throughout the measurements. All specimens were coated with epoxy on the sides to prevent inhomogeneous conditions. The final test specimen can be seen in Figure 6.4.

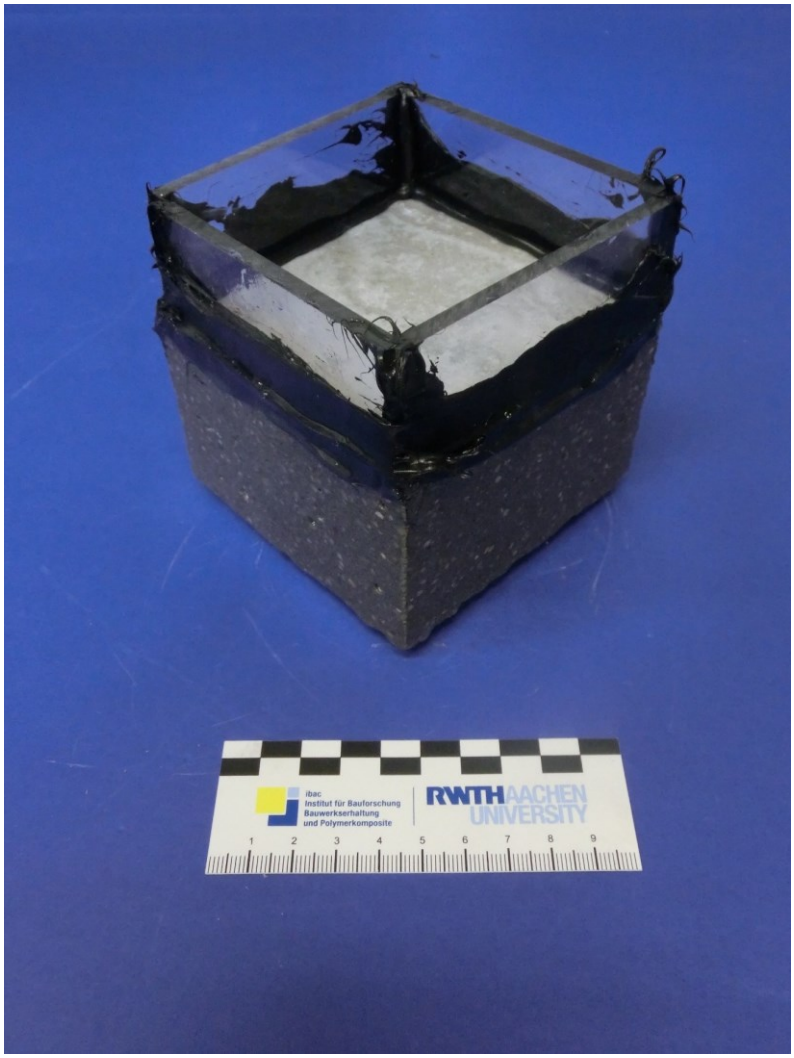

Figure 6.4. Final specimen with water basin on top

6.1.4.3 Measurements

After filling the 4 % NaCl solution into the water basins and covering the basins with a lid, the measurements were started. The respective voltage was applied between the carbon meshes

with specifically developed equipment. Each day, the instant-off potential was measured for 5 seconds, recording 250 potential values. The currents were measured continuously. The chloride ingress was determined by analysing the depth profile of the chlorides by grinding some additional specimens every few weeks, drying the grinded mortar, and carrying out a potentiometric titration in the chemical laboratory. These specimens were stored and the test specimens under laboratory climate (20°C/ 65 % rel. humidity). All measurements were stopped after approx. 110 days when the chlorides reached the specimen bottom of the dried series, respectively, as soon as the reference probes showed increased chloride values in the lowest layer. Afterwards, the inner square of all specimens was resected, which can be seen in Figure 6.5, grinded, and the chloride depth profile was analysed by titration.

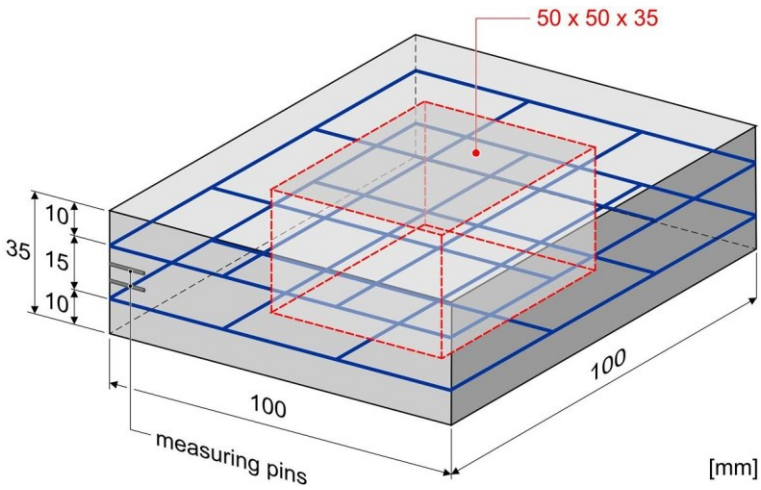

Figure 6.5. Dimensions and area for the chloride sampling

6.1.5 Results and Discussion

6.1.5.1 Water-saturated Series

For a better overview, the chloride values were plotted over the depth of the specimens for the specimens with the same geometry or the same anode distances, respectively. Figure 6.6 shows the percentage of chloride concentration over the depth of the water-saturated specimens, exemplarily for the middle anode distance of 30 mm after 110 days.

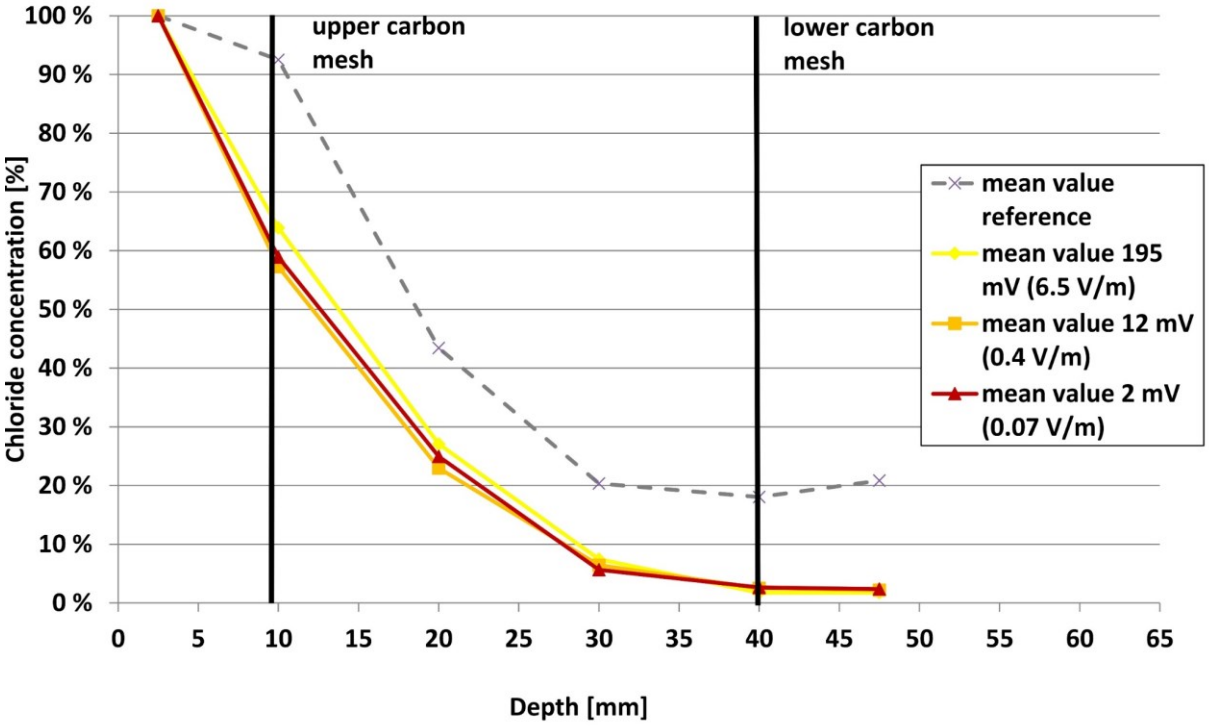

Figure 6.6. Relative chloride concentration of the water-saturated specimens under different voltages (duration: 110 days)

It can be seen that all applied voltages lead to a reduction of chlorides in contrast to the current-less reference. At the bottom of the specimens, approx. 20 % fewer chlorides were detected for the applied voltages compared to the reference. No differences in the curves of the measured values for the different voltages can be seen when all measurement points are referred to the first measurement point (individual initial concentration). By looking at the absolute chloride values in M-% referred to concrete mass, the results can be investigated in more detail. Figure 6.7 shows these absolute values for the same specimens as before, complemented by the standard deviations.

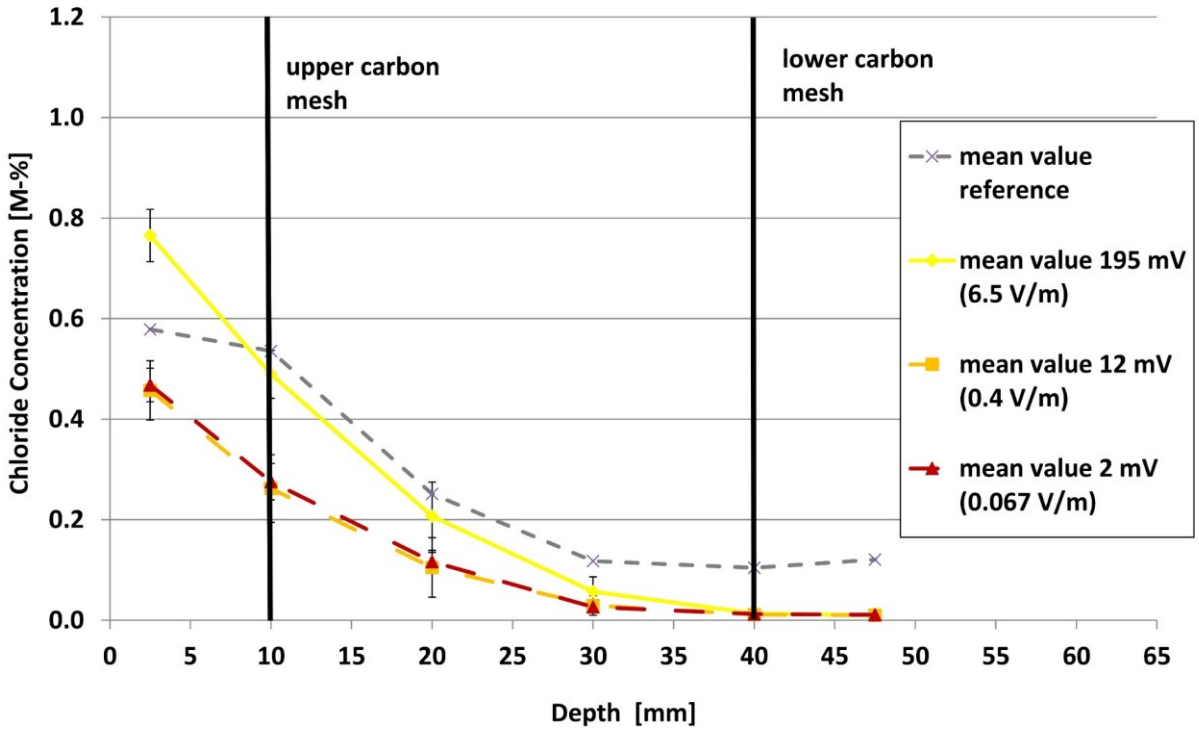

Figure 6.7. Absolute chloride concentrations of the water-saturated specimens under different voltages

It can be seen that above the first carbon mesh, the application of the highest voltage even leads to higher chloride concentrations than the reference. Between the two carbon meshes, the 195 mV line crosses the reference line but still shows higher chloride concentrations than the 12 mV and 2 mV lines. Only on the bottom of the specimens the 195 mV line shows the same chloride concentration as the lower voltage specimens. This indicates that in these experiments, higher voltages are not generally able to prevent chloride ingress better than lower voltages because of the higher chloride contents above the first carbon mesh. By determining the electrolyte voltages, it can be shown that higher externally applied voltages lead to higher voltages in the electrolyte. One can exclude those higher voltages only lead to higher consumption of current at the electrodes. Table 6.3 shows the voltages in the electrolyte, and the measured currents for the corresponding externally applied voltages for the previous diagrams.

Table 6.3. Voltages with resulting voltages in the electrolyte and measured currents

Voltages in V	IR-Drop/ voltages in the electrolyte in mV	Currents in µA
0.5	2	6
1	12	21
2	195	1150

Although the voltages in the electrolyte and the measured currents are comparatively small, they are measurable and can work against diffusion.

All in all, the results show that all investigated voltages lead to a reduction of chloride concentration compared to the reference if the effects of diffusion and migration are investigated. This observation also seems to be independent of the used anode material. A reduction of the chloride concentration by the same magnitude was achieved by using titanium meshes as a reference, which can be seen in Figure 6.8.

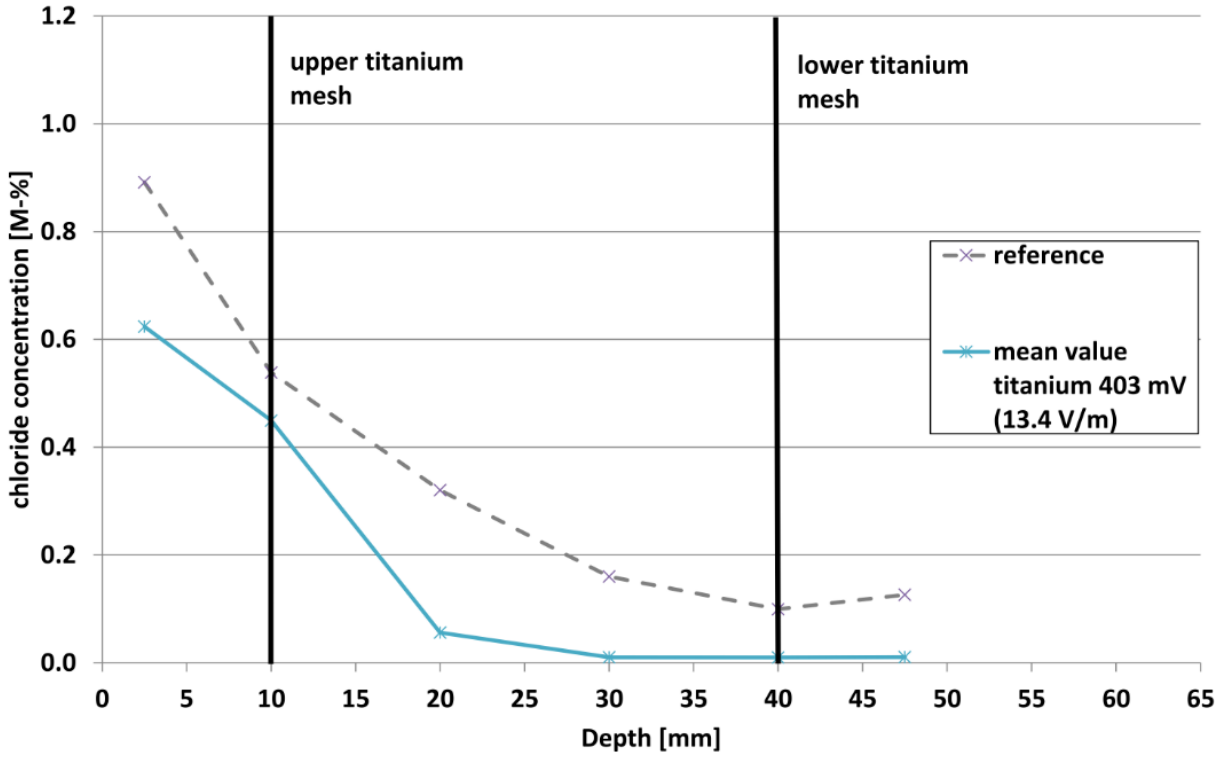

Figure 6.8. Absolute chloride concentrations of the water-saturated specimens with titanium meshes

It has to be mentioned that the same external applied voltage of 2 V leads to higher electrolyte voltages if titanium meshes are used instead of carbon meshes. This can probably be explained by the higher voltage drop on the carbon meshes impregnated with epoxy resin.

6.1.5.2 Dried Series

The picture changes if convection is occurring, too. Figure 6.9 shows the absolute chloride concentration in M-% for dried specimens for the same exemplary geometry.

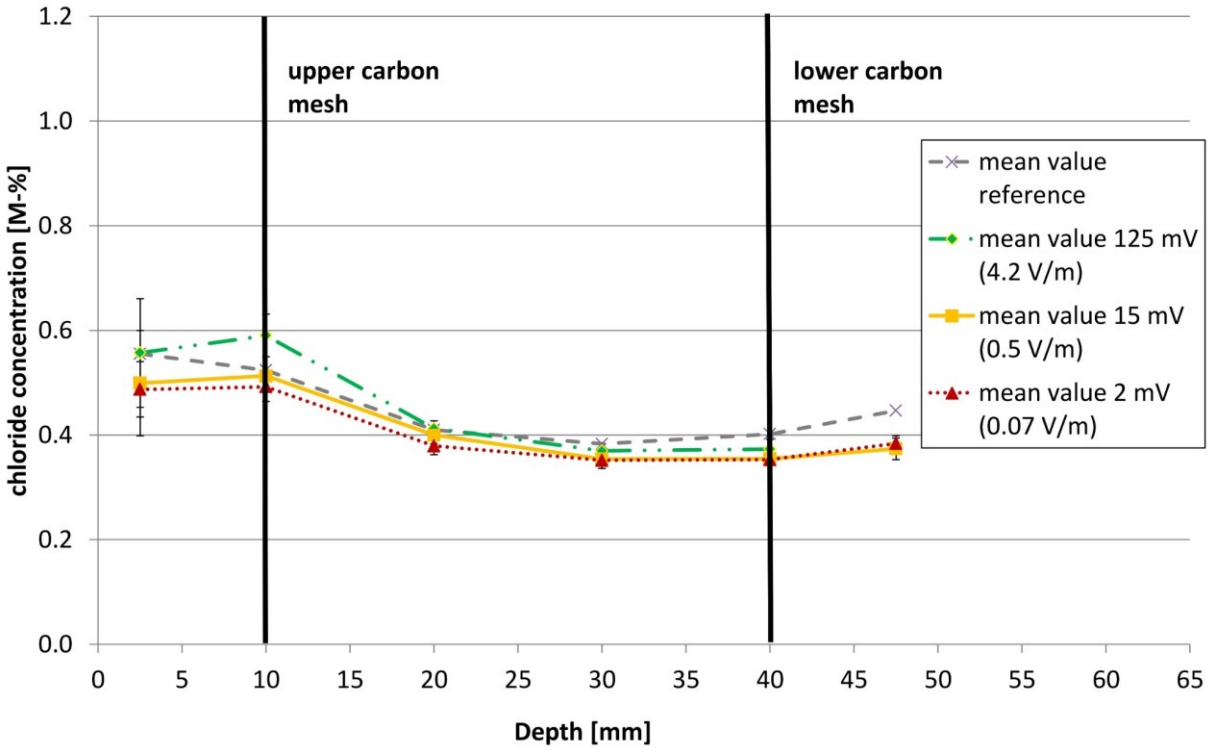

Figure 6.9. Absolute Chloride concentrations of the dried specimens under different voltages

It can be seen that the applied electrical field induces nearly no reduction in chloride concentration. A small reduction in comparison to the reference at the bottom of the specimens is achieved for all voltages. It seems that the convection in the dried specimens in combination with the diffusion overweighs the effect of migration concerning the prevention of chloride ingress.

To take a look at the other geometries apart from the one with an anode distance of 30 mm and to investigate the effect of the resulting different electrical field strengths, Figure 6.10 shows the mean values of the chloride concentrations for all specimens with 1 V as external voltage summed up in the various electrical field strengths.

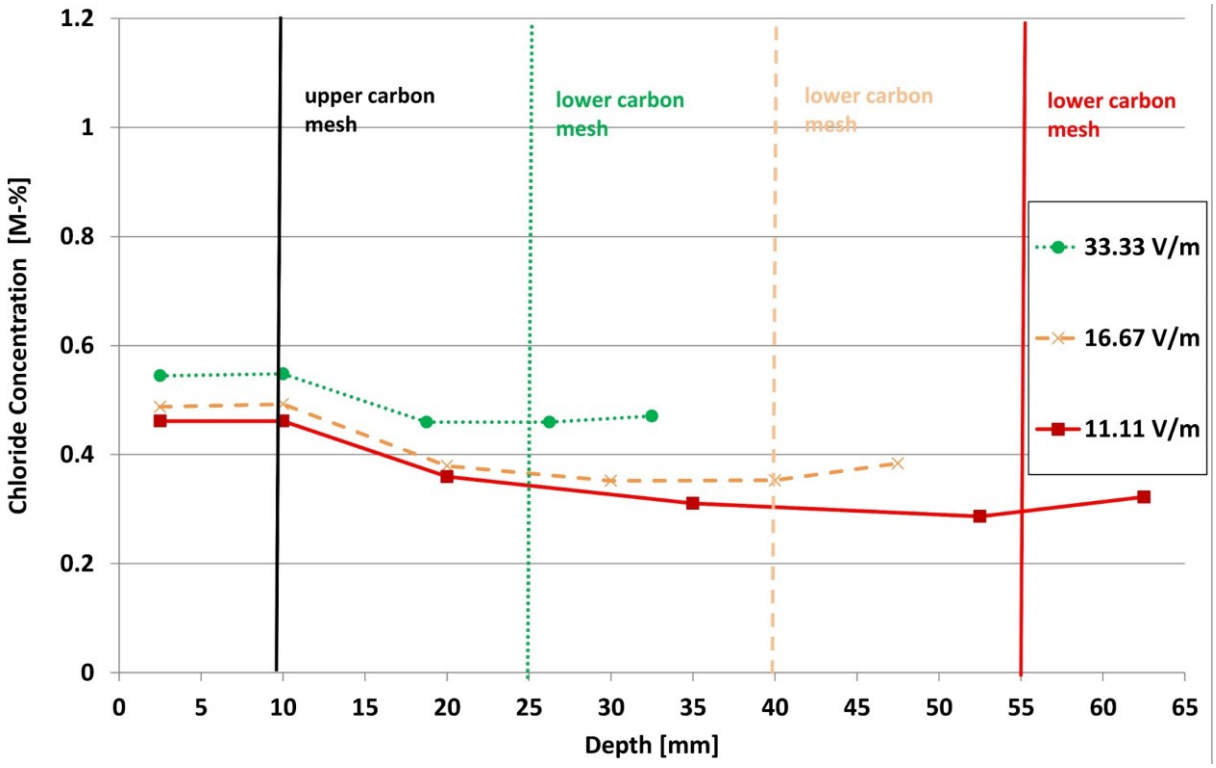

Figure 6.10. Chloride concentrations of the dried specimens depending on the electrical field strengths

Here again, the chloride concentration in the dried specimens regarding convection could only be slightly decreased over the specimens´ depths. Secondly, once again, it can be seen that the higher electrical field strengths lead to higher initial chloride concentrations above the upper carbon mesh. This also allows the conclusion that not the absolute voltage determines the effectiveness of the chloride barrier but, as expected according to the theory, the electrical field strengths. Nevertheless, it is reasonable first to consider the applied voltages as long as specimens with the same geometries were compared because, in this case, a doubling of the external voltage leads to a doubling of the arithmetical electrical field strength.

6.1.5.3 Comparison of the Results with Numerical Simulations

For validation of the laboratory results, first numerical simulations of the laboratory tests were performed, followed by a more detailed numerical simulation study. A 3D model was created with the COMSOL Multiphysics software using, amongst others, the modules “Chemical Reaction Engineering Module” and “AC/DC Module”. The structure of the laboratory test specimen was modelled as shown in Figure 6.11.

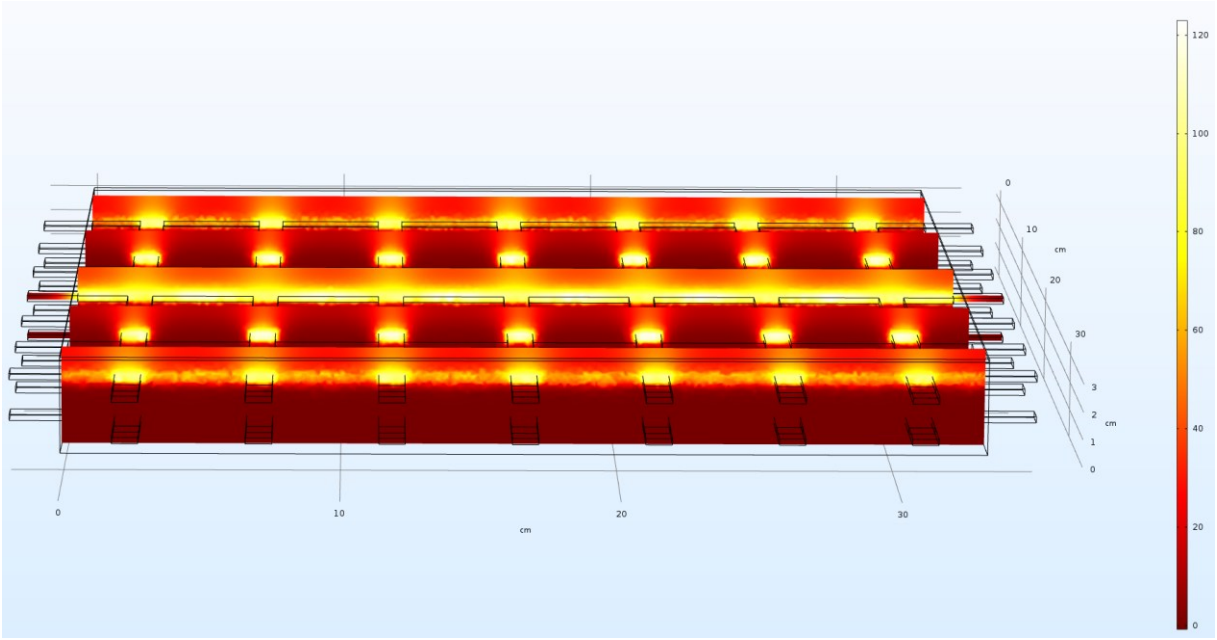

Figure 6.11. Numerical model in COMSOL Multiphysics: distribution of the chloride concentration in mol/m3

More specifically, the middle anode distance of the laboratory specimens was chosen. As in the laboratory, on top of the specimens, a sodium chloride solution was applied, and the chloride ingress over 650 days was simulated for an external electrolyte voltage of 0; 0.1; 0.2; 0.3; 0.4; 0.5; 0.8; 1; 2 and 3 V over the depth of the specimens. According to the described test setup, the electrolyte could be assumed to be homogeneous and isotropic because the laboratory test showed that the chloride barrier worked properly only in at least partly saturated conditions, for the simulations, a resistance of a water-saturated mortar of around 150 Ωm was chosen, and convection was neglected. Figure 6.12 shows the results of the numerical simulations for water-saturated conditions, namely the chloride concentration over the specimen depth for different applied voltages.

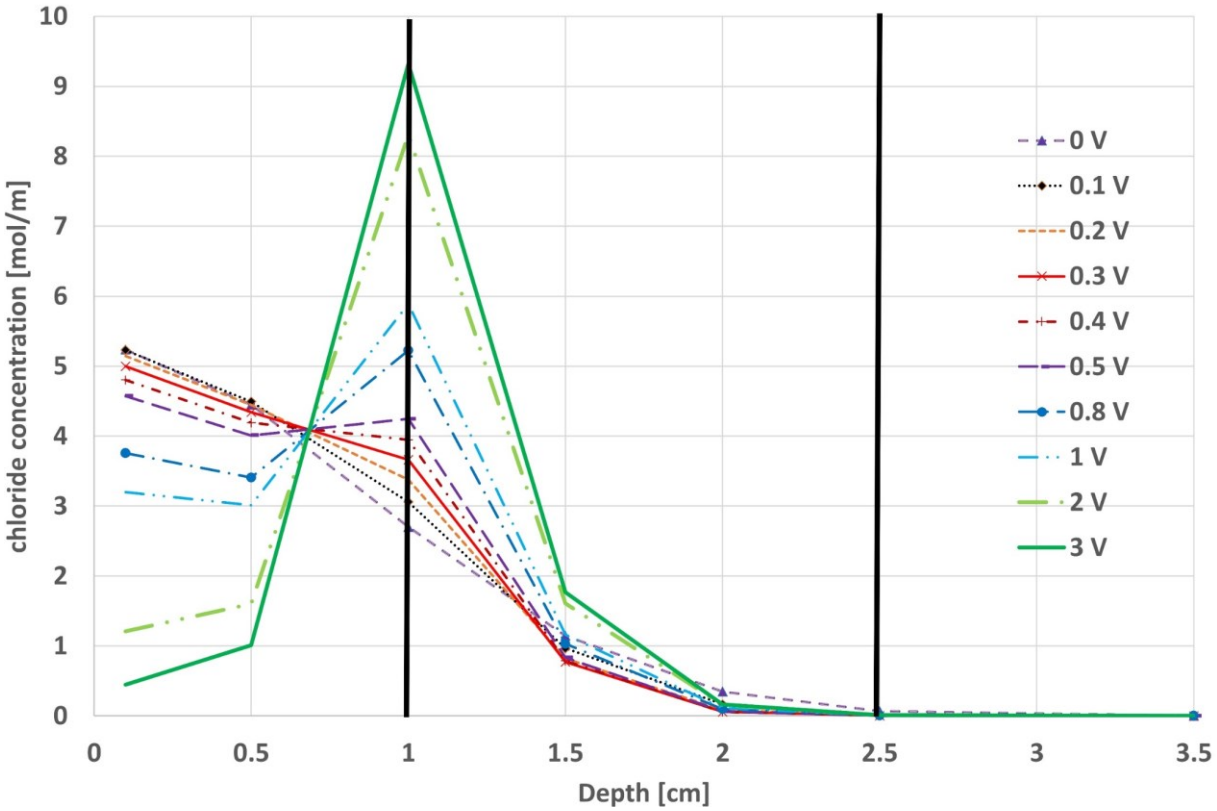

Figure 6.12. Results of the numerical simulations for water-saturated conditions: Chloride concentration over the specimen depth for different voltages

Again, the position of the carbon meshes is highlighted by the black lines. By comparing Figure 6.7 and Figure 6.12, the simulations show the same effect of higher chloride contents for the higher voltages around the upper anode. Only after an individual intersection for each graph with the reference graph of 0 V between the middle of the two meshes, the applied voltages lead to lower chloride concentrations than the reference. To take a closer look at the area behind the lower carbon mesh, which is the area that should be protected against chlorides, one can see that even the smallest applied voltages lead to a reduction in chloride concentration compared to the reference for longer testing times (see Figure 6.13). The time when the chloride barrier starts to take effect depends on parameters like the exact diffusion coefficient and electrical resistance of the mortar.

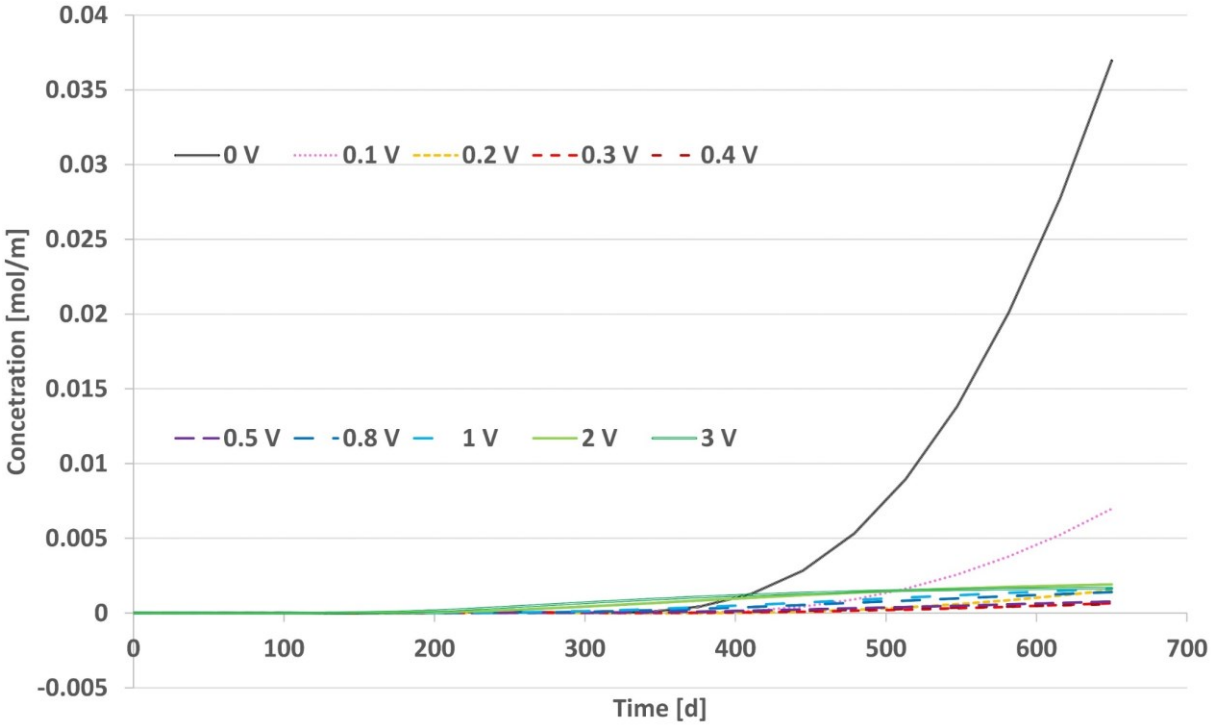

Figure 6.13. Results of the numerical simulation for water-saturated conditions: Chloride concentration behind the lower carbon mesh at depth 3.5 cm for different voltages

6.1.6 Conclusions & Outlook

All in all, the following conclusions can be drawn from the laboratory test and numerical simulations:

- In laboratory tests, the effect of a chloride barrier with electrolyte voltages between 2 mV – 400 mV corresponding to the electrical field strength of 0.07 V/m – 13.33 V/m compared to a current-less reference was proven for water-saturated specimens regardless of the anode material.
- The effect of the chloride barrier for these voltages in the viewed testing time of 110 days was not high enough to overweigh diffusion and convection. Furthermore, it will probably not work for wholly dried mortar conditions. However, for an actual structure, wholly dried conditions of the mortar are unlikely anyway.
- Numerical simulations showed the same effect of an effective chloride barrier for water-saturated specimens. After a certain period, all applied voltages lead to reduced chloride concentrations below the lower carbon mesh.

Future investigations will focus on further numerical simulations to investigate the question of which applied voltages at a given depth led to the best effectiveness of the chloride barrier. Furthermore, the question of whether just a balance of forces between diffusion, convection, and migration leads to the described effects or if other aspects such as decomposition voltage

or geometry effects influence the results. Finally, an analytical solution of the equation for the specific boundary conditions of the described situation will be investigated.

6.2 Analytical and Numerical Investigation of an Electrochemical Chloride Barrier for Reinforced Concrete Structures

6.2.1 Abstract

During the development of a carbon-reinforced mortar interlayer for bridges, the idea of an electrochemical chloride barrier arose. An electrical field is generated between two carbon meshes, and the negatively charged chloride ions are held on the polarized upper carbon mesh to prevent chloride-induced corrosion in the reinforcement. Laboratory tests unexpectedly showed that higher voltages lead to an increase in chloride ions for certain depths of the reference probes. This paper discusses the implementation of analytical and numerical models that finally explain the effect only by the acting diffusion and migration with the help of a finite differences model and FEM simulations. The effect of the local minimum is limited to positions above the depth of the first carbon layer of the test specimens. It is caused by the lines of the electrical field between the first and second carbon layers. According to the experimental and FEM simulation results, higher voltages lead to lower chloride concentrations for all positions below the first carbon layer only after sufficient time duration. Therefore, the intended effect of an electrochemical chloride barrier can, in general, only be observed and confirmed after a certain time, depending on position, conditions, and parameters.

6.2.2 Introduction

In the course of a research project, an interlayer for bridges was developed to be used for multiple purposes. The 35 mm thin interlayer consisted of two carbon meshes with a spacing of 15 mm, each embedded in a newly developed mortar. By measuring the resistivity between the carbon meshes, leakages in the sealing layer of the bridge were detected by decreasing resistivity values due to intruding water. When a leak was detected, an external voltage between the two carbon layers was supposed to reduce the chloride ingress and, therefore, prevent corrosion damage in the reinforcement. Furthermore, the textile reinforcement led to greater shear force strength. (Adam et al., 2020; Driessen-Ohlenforst et al., 2020) The function of chloride ingress prevention was named the “electrochemical chloride barrier”. It aims to reduce or even eliminate the necessity of expensive maintenance and repair measures due to chloride-induced corrosion of the reinforcement. Thus, traffic obstructions can be prevented, which often lead to economic losses.

To investigate and confirm the effectiveness of chloride ingress prevention, laboratory tests were performed. In (Driessen-Ohlenforst & Raupach, 2021), it was demonstrated that voltages between 0.5 and 2 Volts reduce chloride concentration behind the anodic polarized mesh for water-saturated specimens and carbon, as well as titanium as an anode material. Due to the destructive testing method of chloride titration on the grinded probes, no time effect was investigated in the laboratory. Analytical and numerical investigations were performed to take any time-dependent effects into account, which will be described in this paper. Furthermore, the laboratory test results showed that higher voltages do not generally lead to lower chloride concentrations in all specimen depths at the investigated testing time but that certain local minima exist, up to which the concentration decreases and the voltage increases, to increase again when a certain voltage value is passed. An investigation of this effect over time and space is focused on throughout the investigations detailed in this paper to clear out potential doubts about the effectiveness of the electrochemical chloride barrier.

To date, various research works have focused on the question of electrochemical chloride extraction (ECE). (de Almeida Souza et al., 2017; H. Y. T. Nguyen et al., 2018; Tissier et al., 2019) In these studies, simulations have also been used to investigate the effect of chloride movement through concrete; however, in comparison with this work, major differences exist (Chen et al., 2021; Xu et al., 2021; Xu & Li, 2019) - Firstly, for electrochemical chloride extraction, much higher voltages are standard and lower voltage ranges are not usually examined. Secondly, the chloride ions are already in the concrete. Finally, due to the anode system, which is placed on top of the structure, the migration is unidirectional from the steel to the anode system, whereas, in the case of the electrochemical barrier, the flux direction changes in the structure depending on which area is observed. The latter is the starting point for the discussion in the following. Figure 6.14 provides a schematic comparison of the above-mentioned differences between previous work and this paper.

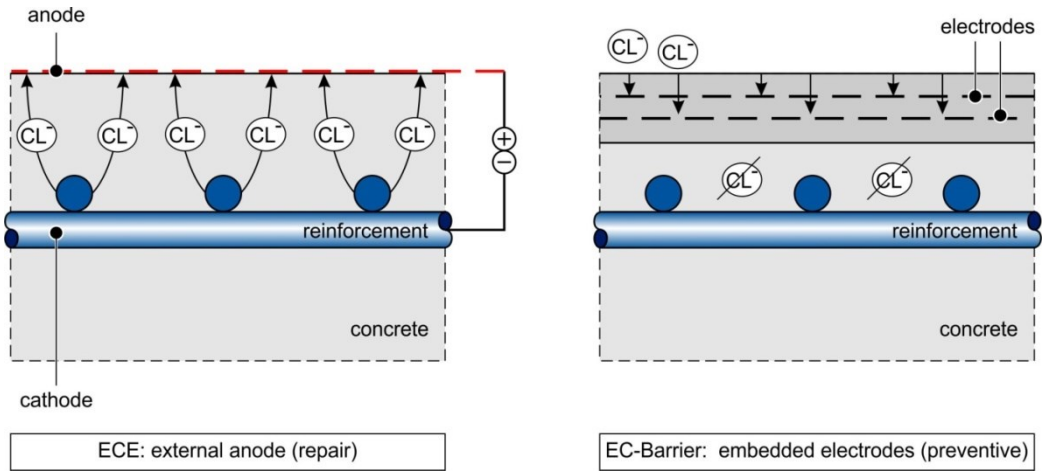

Figure 6.14. Comparison ECE vs. EC-Barrier

6.2.3 Materials and Methods

To start any numerical and analytical investigations of the time- and space-dependent behaviour of the chloride ions in an EC-barrier, s. Figure 6.14, it must be described as a mathematical-physical problem, which is to be solved. A reasonable simplification of the problem and the boundary, as well as initial condition, is targeted to also allow for the derivation of analytical and efficient numerical solution approaches to explain the experimentally observed phenomenon.

6.2.3.1 Simplified Mathematical–physical Problem

The flow of the particles in the probe can be described in the two areas - first, from the top of the specimen to the first carbon layer (I) (s. Eq. 6.3) and, second, from the first to the second carbon layer (II) (s. Eq. 6.4), which can be seen in Figure 6.15.

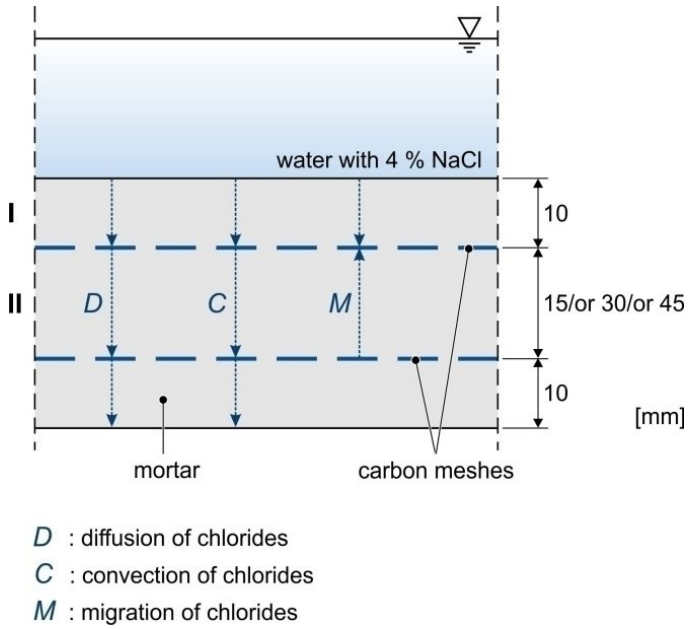

Figure 6.15. Schematic picture of the investigated structure and ion movement

There is a diffusion term, which results from Fick's first law, as well as a convection and migration term originating from the direction of the electrical field and the water flow into the probe, respectively. The latter is assumed here as constant in time and space. This results from the considerations that the height of the bath with the 4% NaCl solution that was applied to the top of the probes, and thus the value of the hydrostatic pressure, is constant over time, as well as from the incompressibility of the fluid and a constant electrical field in between the layers.

$$(\mathrm{I}) \quad \mathrm{J} = -\mathrm{D}_{\mathrm{eff}} \cdot \frac{\partial \mathrm{c}}{\partial \mathrm{x}} + \mathrm{v} \cdot \mathrm{c} + \mathrm{u}_{\mathrm{m}} \cdot \mathrm{c} \qquad 6.3$$

$$(II)\quad J = -D_{eff} \cdot \frac{\partial c}{\partial x} - v \cdot c + u_m \cdot c \qquad 6.4$$

With:

J: Molar flow of the NaCl ions [mol/(m²*s)]

D_{eff}: Diffusion coefficient of NaCl ions in mortar [m²/s)]

c: Concentration of NaCl ion in mortar [mol/m³)]

x: Position along the depth of the probe [m]

v: Average speed of NaCl ions in electrical field [m/s]

u_m: Average mass-related speed [m/s]

The continuity equation describes the relationship between the change in concentration in volume over time and the flow:

$$\frac{\partial c}{\partial t} + \frac{\partial J}{\partial x} = 0 \qquad 6.5$$

After substituting Eq. 6.3 and 6.4 into Eq. 6.5, we obtain:

$$(I)\quad \frac{\partial c}{\partial t} = D_{eff} \cdot \frac{\partial^2 c}{\partial x^2} - [v + u_m] \cdot \frac{\partial c}{\partial x} \qquad 6.6$$

$$(II)\quad \frac{\partial c}{\partial t} = D_{eff} \cdot \frac{\partial^2 c}{\partial x^2} - [u_m - v] \cdot \frac{\partial c}{\partial x} \qquad 6.7$$

By combining the constants, v and u_m, both equations can be represented in the familiar form of the one-dimensional unsteady convection–diffusion equation:

$$\frac{\partial c}{\partial t} = D_{eff} \cdot \frac{\partial^2 c}{\partial x^2} - v_{eff} \cdot \frac{\partial c}{\partial x} \qquad 6.8$$

Where:

$$(I)\quad v_{eff} = v + u_m \qquad 6.9$$

$$(II)\quad v_{eff} = u_m - v \qquad 6.10$$

With:

v_{eff}: Effective speed of the NaCl ions [m/s]

In addition, the following initial and boundary conditions apply:

$$\text{For } t = 0, 0 \le x \le L:\ c = 0 \qquad 6.11$$

$$\text{For } t \geq 0, x = 0: \; - \; D_{eff} \cdot \frac{\partial c}{\partial x} = v_{eff} * (c_0 - c) \tag{6.12}$$

$$\text{For } t \geq 0, x = L: \frac{\partial c}{\partial x} = 0 \tag{6.13}$$

With:

c_0: Concentration of the NaCl ions in the NaCl solution [mol/m³]

L: Length / Depth of the probe [m]

Different approaches for obtaining analytical and numerical solutions to the problem were derived, each with different advantages and disadvantages, e.g., regarding the simplification of the problem, the complexity of implementing the solution, and the computational load. They are discussed in the following sub-sections.

While sub-section 2.2 and 2.3 refer to an analytical and efficient numerical solution approach of the simplified 1D-problem assuming one material only, section 2.4 deals with a more complex numerical solution approach for the problem in 3D assuming a multi-material geometry.

6.2.3.2 2.2. Analytical Solution of the Simplified 1D-Problem

(Bastian & Lapidus, 1956) provide the basis for an approach to analytically solve the system of equations. First, the variables are changed as follows:

$$c - c_0 = w * e^{\frac{v_{eff} * x}{2 * D_{eff}} - \frac{v_{eff}^2 * t}{4 * D_{eff}}} \tag{6.14}$$

With this, as well as with

$$h = \frac{v_{eff}}{2 * D_{eff}} \tag{6.15}$$

With:

h: Film coefficient [m]

Eq. 6.8, 6.11, 6.12 and 6.13 can be simplified according to (Danckwerts, 1995):

$$D_{eff} \cdot \frac{\partial^2 w}{\partial x^2} = \frac{\partial w}{\partial t} \tag{6.16}$$

$$\text{For } t = 0, 0 \leq x \leq L: w = -c_0 * e^{-h * x} \tag{6.17}$$

$$\text{For } t \geq 0, x = 0: \frac{\partial w}{\partial x} = h * w \tag{6.18}$$

$$\text{For } t \geq 0, x = L: \frac{\partial w}{\partial x} = -h * w \tag{6.19}$$

According to (Carslaw & Jaeger, 1959), the transformed solution then looks like:

$$w = 2 * \sum_{n=1}^{\infty} e^{-D_{eff} * \alpha_n^2 * t} * \frac{\alpha_n * \cos \alpha_n * x + h * \sin \alpha_n * x}{(\alpha_n^2 + h^2) * L + 2 * h} * I \tag{6.20}$$

Where:

$$I = \int_0^L -c_0 * e^{-h*x} * (\alpha_n * \cos \alpha_n * x + h * \sin \alpha_n * x) dx \tag{6.21}$$

Based upon Eq. 6.20 and 6.21, (Bastian & Lapidus, 1956) formulated the solution for the concentration at x=L, and (Mohsen & Baluch, 1983) formulated the solution for different boundary conditions. The integral in Eq. 6.21 is solved to give for 0<x≤L considering Eq. 6.17 to 6.19:

$$-\frac{I}{c_0} = \alpha_n * \left[\frac{e^{-h*x}}{\alpha_n^2 + h^2} * (-h * \cos \alpha_n * x + \alpha_n * \sin \alpha_n * x)\right]_0^L \tag{6.22}$$

This finally results in:

$$-\frac{I}{c_0} = \frac{e^{-h*L}}{\alpha_n^2 + h^2} * (-2 * \alpha_n * h * \cos \alpha_n * L + (\alpha_n^2 - h^2) * \sin \alpha_n * L) + \frac{2 * \alpha_n * h}{\alpha_n^2 + h^2} \tag{6.23}$$

where, according to (Carslaw & Jaeger, 1959), α_n represents the roots of:

$$\tan \alpha_n * L = \frac{2 * \alpha_n * h}{\alpha_n^2 - h^2} \tag{6.24}$$

Eq. 6.24 can be transformed to:

$$\frac{2 * h}{\tan \alpha_n * L} = \alpha_n - \frac{h^2}{\alpha_n} \tag{6.25}$$

With the substitution

$$\alpha_n * L = r_n \tag{6.26}$$

Eq. 6.25 finally becomes:

$$2 * \cot r_n = \frac{r_n}{h * L} - \frac{h * L}{r_n} \quad 6.27$$

According to (Carslaw & Jaeger, 1959), the positive roots can be found in any interval [n*π,(n+1)*π] for n∈N. This allows us to calculate w according to Eq. 6.20 and, finally, taking into account the change in variables according to Eq. 6.14, to calculate the time- and depth-dependent solution for the concentration c. In Eq. 6.20, the infinite sum is approximated by a finite sum using the first n terms.

6.2.3.3 Numerical Solution with Finite Differences of the Simplified 1D-Problem

The finite difference method is an established method for solving differential equations based on the discretization of derivatives. (Doubova et al., 2018; Li, 2020; Meister & Sonar, 2019) Using the finite difference method, Eq. 6.8 can be discretized for the numerical solution on grid points in a two-dimensional time-space grid and is represented as follows:

$$\frac{c_i^{j+1} - c_i^j}{dt} = D_{eff} * \frac{\left(c_i^j - 2 * c_i^j + c_{i-1}^j\right)}{dx^2} - v_{eff} * \frac{\left(c_{i+1}^j - c_{i-1}^j\right)}{2 * dx} \quad 6.28$$

Where:

$$c_i^j = c(t = j * dt, x = i * dx) \quad 6.29$$

With:

- c_i^j: Discretized solution for the concentration [mol/m³]
- j: Time index in solution grid, $j \in N_0$, $j = 0..\ n_t$
- i: Spatial index in solution grid, $i \in N_0$, $i = 0..\ n_x$
- n_x: Maximum spatial index in solution grid, $n_x \in N$
- n_t: Maximum time index in solution grid, $n_t \in N$
- dt: Time increment in solution grid [t]
- dx: Spatial increment in solution grids [m]

For the initial and boundary conditions, the following holds:

$$\text{For } j = 0, i = 0..\ n_x:\ c_i = 0 \quad 6.30$$

$$\text{For } j = 0..n_t: -D_{eff} * \frac{\left(c_1^j - c_0^j\right)}{dx} = v_{eff} * \left(c_0 - c_0^j\right) \quad 6.31$$

$$\text{For } j = 0..n_t, i = n_x: \frac{c_{i+1} - c_i}{dx} = 0 \quad 6.32$$

Eq. 6.28 is transformed to determine the concentration. For area I, the result for the water-saturated case with convection due to migration only and after introducing a fitting factor for the migration speed is:

$$c_i^{j+1} = c_i^j + D_{eff} * \frac{dt}{dx^2} * \left(c_{i+1}^j - 2 * c_i^j + c_{i-1}^j\right) - f_{net} * v * \frac{dt}{2 * dx} * (c_{i+1}^j - c_{i-1}^j) \quad 6.33$$

With:

f_{net}: Fitting factor for the migration speed [-]

Assuming an electric field exclusively in area II, f_{net}=0 applies in Eq. 6.33. However, the fitting factor can also be used later to model a weakened effect of the electric field in area I. The latter can be observed in the results from the FEM simulations discussed in the following section of this paper. In this context, the area I can be divided into subareas with different fitting factor values to approximate this effect.

For area II, the following applies:

$$c_i^{j+1} = c_i^j + D_{eff} * \frac{dt}{dx^2} * \left(c_{i+1}^j - 2 * c_i^j + c_{i-1}^j\right) + v * \frac{dt}{2 * dx} * (c_{i+1}^j - c_{i-1}^j) \quad 6.34$$

For j=0..n_t,i=n_t, the following applies:

$$c_i^{j+1} = c_i^j + D_{eff} * \frac{dt}{dx^2} * \left(c_i^j - 2 * c_i^j + c_{i-1}^j\right) + v_{eff} * \frac{dt}{dx} * (c_i^j - c_{i-1}^j) \quad 6.35$$

For j=0..n_t, the following applies:

$$c_0^t = \frac{\left(v_{eff} * c_0 + \frac{D_{eff}}{dx} * c_1^t\right)}{v_{eff} + \frac{D_{eff}}{dx}} \quad 6.36$$

Thus, the discretized concentration c_i^t can be determined starting from Eq. 6.33 for t=0 as well as from Eq. 6.34 to 6.36 for all following time steps for all grid points. It is to be iterated over all time and location indices, i.e., c_i^{j+1} is calculated for j=0..(n_t-1) and i=1.. n_x.

6.2.3.4 Solution with the Finite Element Method for the 3D Problem with Multi-material Geometry

Using the finite element method (FEM), modern FEM multiphysics simulation software like COMSOL can solve transient problems arising from differential equations for almost arbitrarily complex geometries in 3D space and potentially consider multiple materials as well as physical phenomena at the same time. COMSOL is proprietary and commercially available. It is provided by COMSOL AB. (*COMSOL - Software for Multiphysics Simulation*, o. J.; Pepper & Heinrich, 2017)

To calculate the ingress of NaCl ions into the probe, the simulation software COMSOL was used. In COMSOL, the problem was not modeled in 1D but 3D, based on a specifically designed multi-material geometry resembling the actual bridge construction as much as possible, as shown in Figure 6.16.

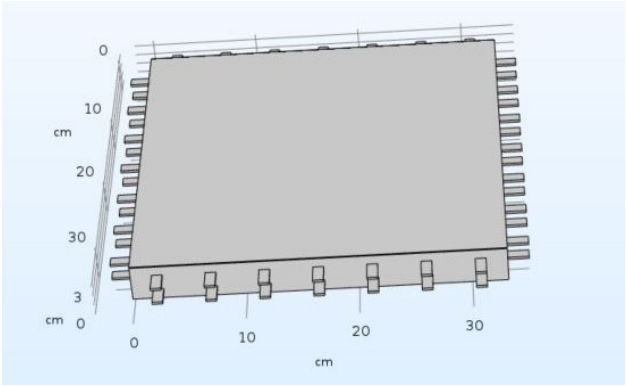

Figure 6.16. 3D model of the multi-material geometry for the FEM simulation with COMSOL

The model was designed as a multi-material 3D geometry of two carbon meshes included in a block of mortar. Within the simulation, in between the two carbon layers, a difference in the electrical potential is defined that automatically leads to the generation of realistic electrical field lines within and around the layers, which influences the flow of chloride ions.

As an initial condition, the concentration of NaCl within the probe was defined to be zero, while, as a boundary condition, a 4% NaCl solution was applied to the top of the probe, leading to a continuous ingress over time.

In COMSOL, the modules “AC/DC” and “Chemical Reaction Engineering” were used to simulate the NaCl ingress into the probe. In this way, the transient and 3-dimensional behavior of the NaCl ions due to diffusion and migration could be considered. Since the probes are

assumed to be water-saturated, convection due to water transport into the probe was neglected. Therefore, the mathematical problem solved with COMSOL, for various distances and different levels of potential in the carbon layers, goes beyond the one described in Eqn. (1)-(11) and more accurately resembles the actual set-up due to the consideration of 3-dimensionality, electrical field lines, and the materialistic existence of the physical carbon layers.

During the modelling, the two problem types, “Electrical Currents” and “Transport of Diluted Species”, were added and configured according to a coupled simulation.
For “Electrical Currents”, the default set of equations for the stationary case was selected with the default value of 50 ohm for the reference impedance, whereas for the “Transport of “Diluted Species” Eqn. (6)-(11) were adopted and given for the 3D case. Only migration in the electrical field was activated as a transport mechanism for which the Nernst-Einstein relationship was selected as an option in COMSOL for modeling.
For both problems, in COMSOL, the physics-controlled meshing option was activated, including free tetrahedron meshes. The size of the elements was configured to be “extra-fine”, resulting in a minimum and maximum element size of 0.0555 cm and 1.29, respectively.
For the solution, quadratic shape functions were chosen for the “Electrical Currents” and linear ones for the “Transport of Diluted Species”. Table 6.4 shows the relevant parameter values configured for the multi-physics simulation.

Table 6.4: Simulation parameters

Parameter	**Value**	**Unit**
Length / Width / Height of mortar specimen	0.3318/0.3318/0.035	m
Spacing of the carbon meshes	0.038	m
Length / Width / Height of carbon layers	0.3318/0.3318/0.00225	m
Depths of the carbon meshes from top	0.01/ 0.025	m
Shape Function “Electrical Currents”	Quadratic	-
Shape Function “Transport of Diluted Species”	Linear	-
Discretization Method	Physics-controlled	-
Mesh Type	Tetrahedron	-
Min. / Max. Element Size	0.0555/1.29	cm
Curvature Factor	0.3	-
Solver (both problems)	Linear iterative	-
Nonlinear method for damping (both problems)	Newton (constant)	-
Termination Technique	Tolerance	-

Termination Tolerance	1	-
Total number of Degrees of Freedom	560989	-

6.2.4 Results - Evaluation and Visualization of the Solutions

Based on the mathematical approaches introduced, a variety of solutions for different parameter configurations were calculated for visualization and comparisons. The comparisons serve two purposes: First, assuring a rough consistency between the solutions for the same parameter configurations as an indicator of valid implementations; second, investigating specific behavior of the NaCl concentration in several solution approaches, i.e., the behavior of NaCl concentrations over different migration configurations at specific depths of the probe. Differences in the various approaches to obtaining a solution are identified and discussed.

The analytical solution was calculated using a symbolic MATLAB script, which was also used to determine the positive roots in (25), for the following parameters over a period of 1 s. Note that the units here refer to parameters integrated over the cross-section area of the specimen due to the assumed 1-dimensionality of the problem.

Table 6.5. Parameter values used for the visualized analytical solution

Parameter	**Value**	**Unit**
c_0	44.44	mol/m
L	1	m
D_{eff}	1	1/s
h	1	m

The parameters chosen here do not yet correspond to realistic values of the observed use-case. In particular, the choice of a significantly increased diffusion coefficient, which leads to correspondingly high ion flux, is intended to reveal irregularities in the calculated solution as well as differences between the analytical and numerical solutions.
Figure 6.17 shows the calculated NaCl concentration along with the depth for different time points.

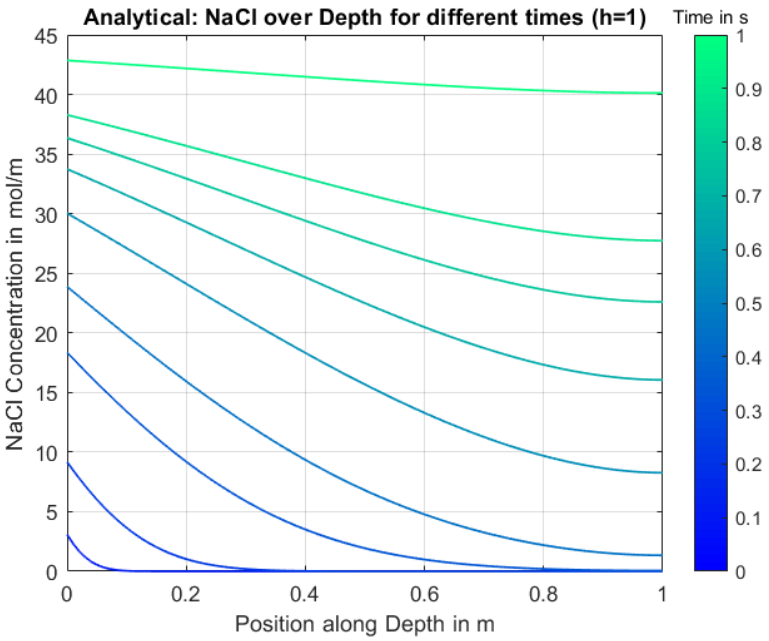

Figure 6.17. Analytical solution results for the concentration over position for different times

Figure 6.18 shows the NaCl concentration calculated and visualized accordingly based on the finite differences solution with only area II being considered for reasons of comparability. Despite the high ion fluxes, there are no significant differences, especially for later time points. Thus, it can be derived that the numerical method generally provides a very well approximated solution with negligible errors for, at least, an equally fine discretization, i.e., identical, or smaller values for dt and dx, for smaller fluxes due to lower, more realistic diffusion coefficients.

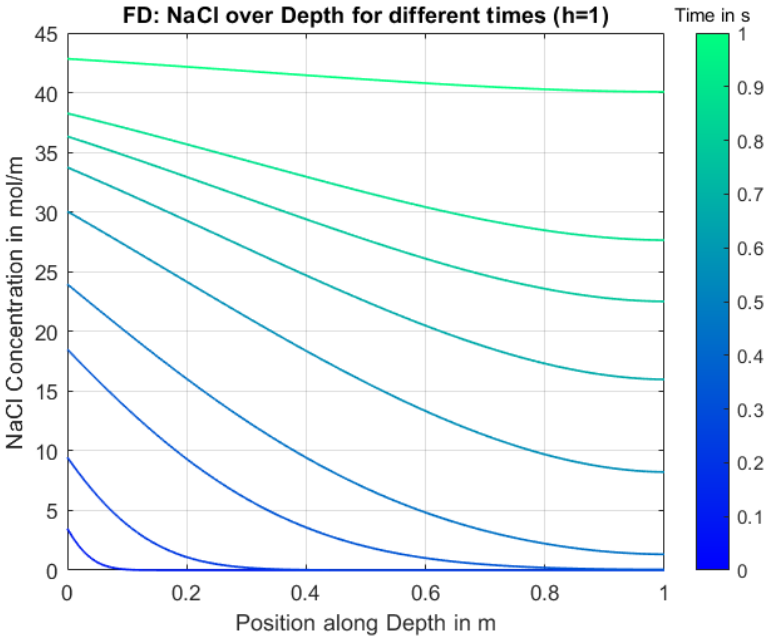

Figure 6.18. Finite differences solution results for the concentration over position for different times

The finite differences solution offers the decisive advantage that, in contrast to the analytical solution, the different migration directions in areas I and II can be considered.
In addition, weakly pronounced field lines, as can be seen later in the results of the FEM simulation, can be considered in area I.
The finite differences solutions were calculated for both areas over a total period of 410 d for the parameter values shown in Table 6.6. A weakened effect of the electrical field in the area I was considered using fitting factors for the migration speed, cf. Eqn. (30).

Table 6.6. Parameter values used for the visualized finite differences solutions

Parameter	**Value**	**Unit**
c_0	63.25	mol/m
L	0.035	m
D_{eff}	1e-12	1/s
h	0, 0.1, 0.2, 0.5, 1, 2, 5, 10, 20, 50, 100, 200, 500, 1000	m
dt	886	s
dx	0.00035	m
L_{net1}	0.01	m
L_{net2}	0.025	m

Where:

L_{net1}: Depth of the first net of the E-field [m]

L_{net2}: Depth of the second net of the E-field [m]

Through the fitting factor in Eq. 6.33, the effect of the electric field at different depth ranges was modeled as follows:

$$f_{net} = \begin{cases} 0.1 * min(h,1)^2 \; für \; x < 0.005\, m \\ 0.2 * min(h,1)^2 \; für \; x < 0.010\, m \\ 0 \; für \; x > 0.025\, m \\ 1, else \end{cases} \quad 6.37$$

Whereas the reasoning for the last two fitting factor values is obvious, the first two values here (x < 0.005 m and x < 0.010 m) are the results of an optimization aiming for maximum similar values of the resulting concentrations as they were observed in the experiments.
Figure 6.19 shows the calculated concentration for different migration velocities along with the depth. Higher migration velocities partly lead to higher concentrations in the initial area and lower concentrations in deeper areas.

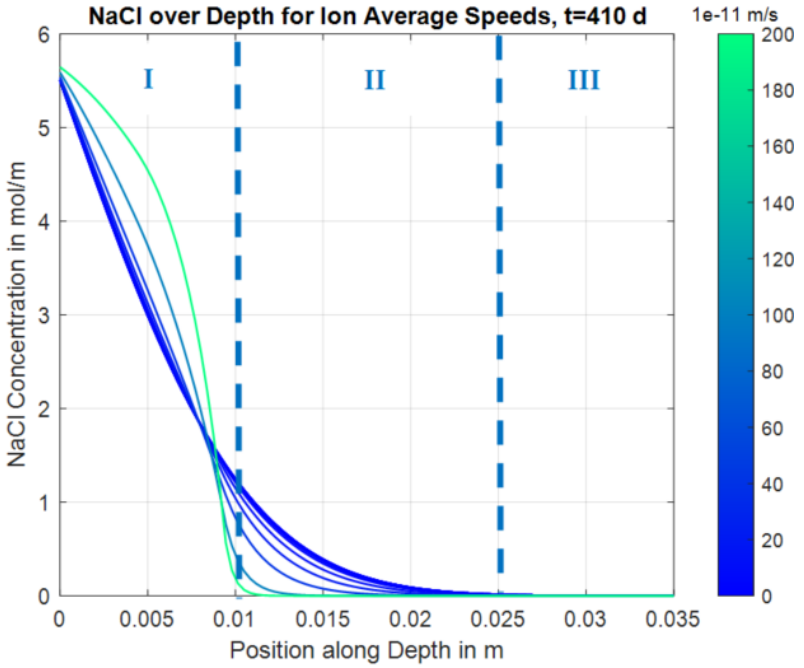

Figure 6.19. Finite differences solutions for concentration over position for different migration velocities (t=410 d)

The effect of the migration speed on the concentration at different depths is clearly shown in the following image for t = 410 d. The trends for higher migration velocities of higher concentrations in the lower depths and lower concentrations in deeper areas, as indicated by the previous figure, are confirmed. Moreover, there is an effect in area I slightly above the first layer where a local minimum is formed. Here, higher migration velocities initially lead to lower concentrations before they lead to higher concentrations again. However, it is also clear that higher migration velocities always lead to lower concentrations in the deeper layers, i.e., at positions in area II below the first carbon layer, which is the expected effect of the chloride barrier. The transition from area I to area II is marked in Figure 6.20.

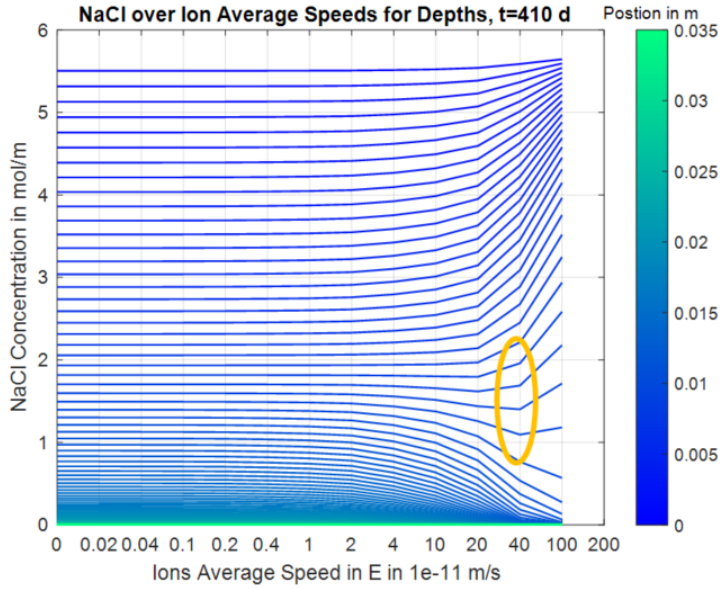

Figure 6.20. Finite differences solution for concentration over migration speed for different positions (t=410 d)

The behavior described can also be seen in the following figures, which consider the dimension of time and thus also consider the time dependency of the concentration versus the migration speed.

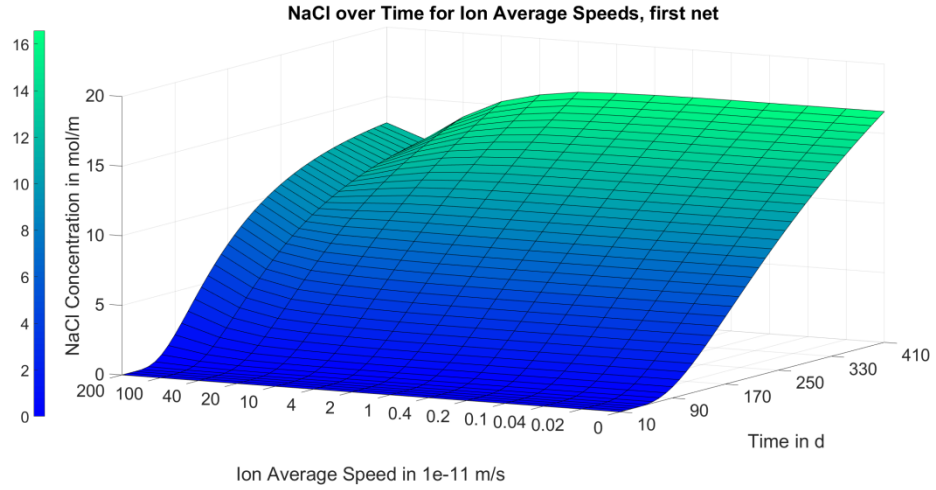

Figure 6.21. Finite differences solution for concentration over migration speed and time (Position = 0.008 m; area I, slightly above the first carbon mesh).

Figure 6.21 illustrates that the local minimum of the concentration over the migration speed slightly above the first carbon layer in area I only forms after a few months. In Figure 6.22, on the other hand, a consistent positive trend can be seen in the concentration over the migration speed in the middle of area I for all time points.

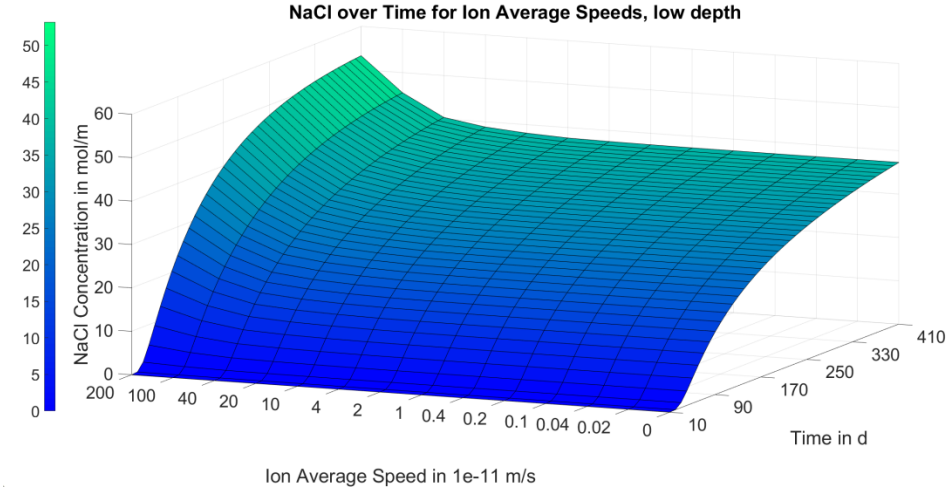

Figure 6.22. Finite differences solution for concentration over migration speed and time (Position = 0.008 m; area I, slightly above the first carbon mesh).

Figure 6.23 shows the concentration curve in area II in the middle of the sample. Here, in contrast to the previous image, the concentration decreases steadily over the migration speed for all the time points.

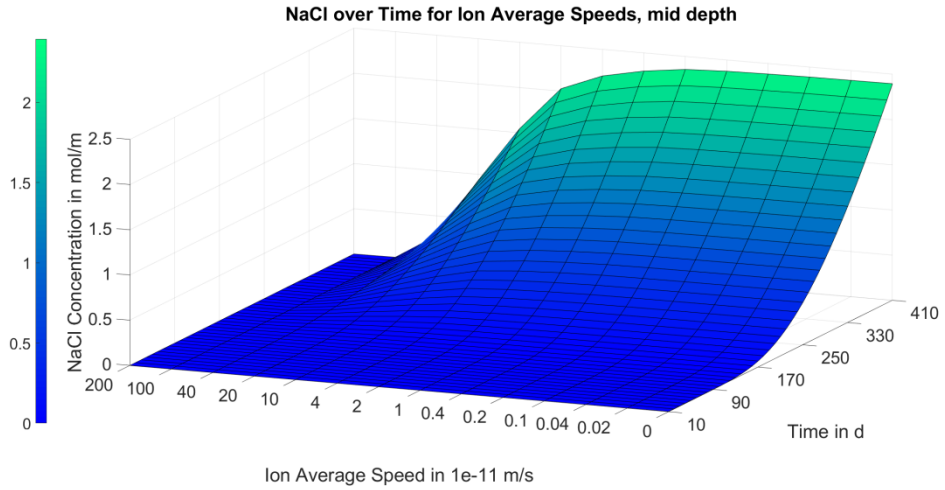

Figure 6.23. Finite differences solution for concentration over migration speed and time.

In Figure 6.24, referring to the bottom of the specimen, it can be seen that the concentration curve predictably also decreases steadily for all time points. After 410 days, the concentration for the two highest migration velocities at the end of the sample is still close to 0.
The temporal gradient of the concentration also increases strongly for the smallest migration velocities, i.e., stationarity is still far from being reached after 410 days.

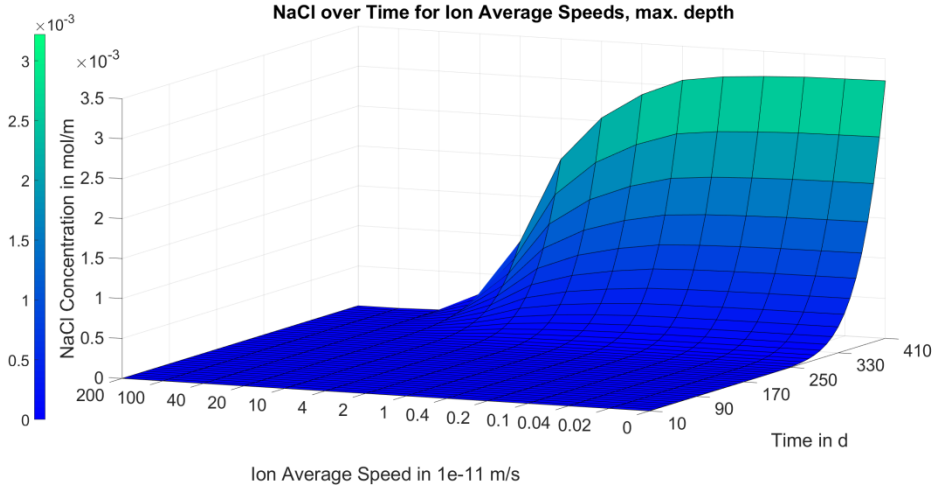

Figure 6.24. Finite differences solution for concentration over migration speed and time (Position = 0.035 m, area III, bottom).

6.2.5 Visualization and Discussion of the FEM Solution

Based on the parameter configuration and the initial and boundary conditions as described above, a variety of simulations was performed for different potential differences between the carbon layers ranging from 0 V to 3 V.

Figure 6.25 shows the distribution of the NaCl concentration along with the depth without an electrical field, a case serving here as a reference for the other non-zero cases. As expected, for t = 650 d, a continuous and smooth change of the NaCl concentration along the depth can be seen, which mainly seems to be 1-dimensional due to the constant distribution at the same depth along with the other directions.

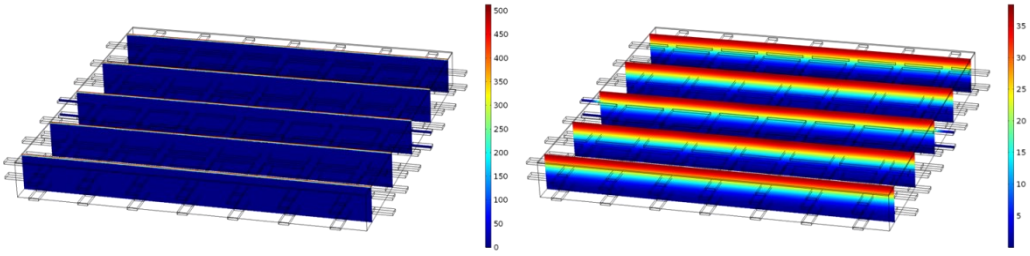

Figure 6.25. A 3D model of the FEM solution for the NaCl concentration for 0 V at t = 0 d (left) and t = 650 d (right)

Compared to Figure 6.25, Figure 6.26 illustrates a significantly different concentration distribution for the same t = 650 d due to the applied potential differences of 0.5 V and 1 V. For both cases, a clear dependency can also be seen on the other directions. The concentration of NaCl is much higher at and around the carbon meshes. A continuous and smooth change of the

NaCl concentration in the case of 0 V cannot be observed anymore. The maximum concentration values even seem to be higher than in Figure 6.25.
Apart from that, for the higher voltage of 1 V, the maximum concentration is higher than for the case of 0.5 V.

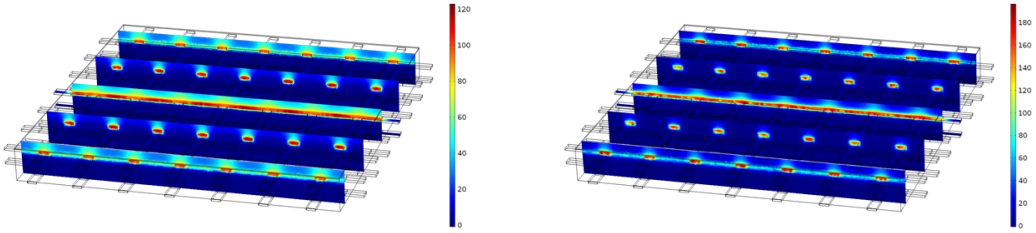

Figure 6.26. A 3D model of FEM solution for the NaCl concentration at t = 650 d for 0.5 V (left) and 1 V (right)

An observation that can be made in Figure 6.26 is an increased concentration above the first carbon layer for both cases, with the case of 1 V showing higher concentrations at these locations than the case of 0.5 V, contradicting the first expectation that the electrical field would exist only between the two carbon layers.
Figure 6.27 provides the reason for this effect; the rounded shape of the potential lines also reaches depths above the first and below the second carbon layer. The qualitative course of the potential lines does not change with changing voltages. Furthermore, a shift in one carbon layer of about half the mesh size does not lead to a significant change in the chloride concentrations.

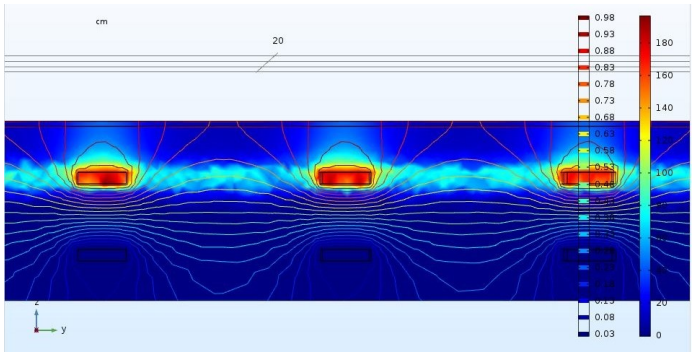

Figure 6.27. A 2D cut of the FEM solution for the NaCl concentration at 1 V and t = 650 d showing potential lines

The resulting concentration over the depth of the probe at t = 410 d is plotted in Figure 6.28.

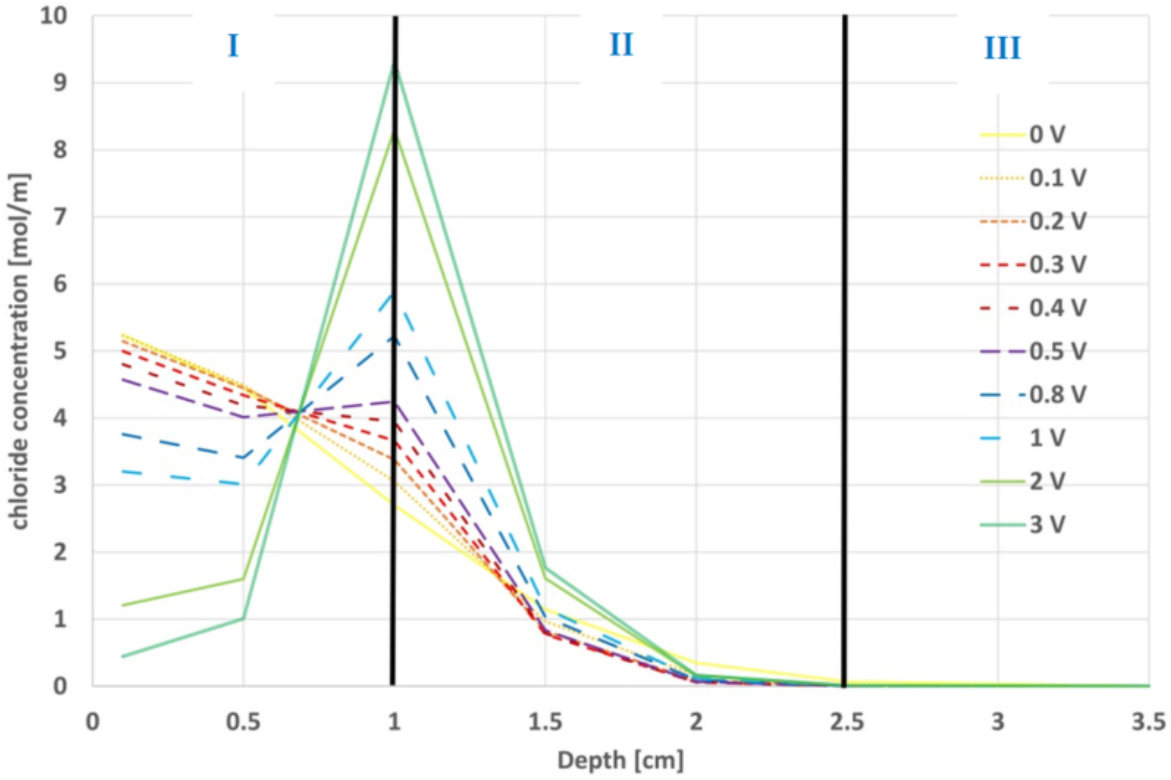

Figure 6.28. FEM solutions for the NaCl concentration over depth for different voltages at t = 410 d

It can be observed that higher voltages lead to higher concentrations at certain positions, especially around the first carbon layer, i.e., the higher the voltage, the higher the concentration. However, this effect is reversed the more you transition from the first carbon layer to the top or the bottom because the chloride ions are either dragged more into the probe from the top or are held back more from diffusing into depth, respectively, the higher the voltage is. It can be seen in Figure 6.28 that from a position slightly above the depth of the second layer, all voltages provide a lower concentration than the reference, which represents the desired chloride barrier effect.

To elucidate this effect and due to the additional time dependency, the NaCl concentration is shown in Figure 6.29 at the bottom of the probe over time up to 650 d. It becomes apparent that t = 410 d approximately marks the time point from which all voltages provide a lower concentration than the reference.
Otherwise, it seems that the curves of lower voltages are based on higher gradients over time than those of higher voltages; i.e., the longer one waits, the lower the concentration at the bottom will be for higher voltages compared to lower voltages. Here, for t = 410 d, the concentrations at 2 V and 3 V are not the lowest; the lowest is the concentration at 0.3 V.

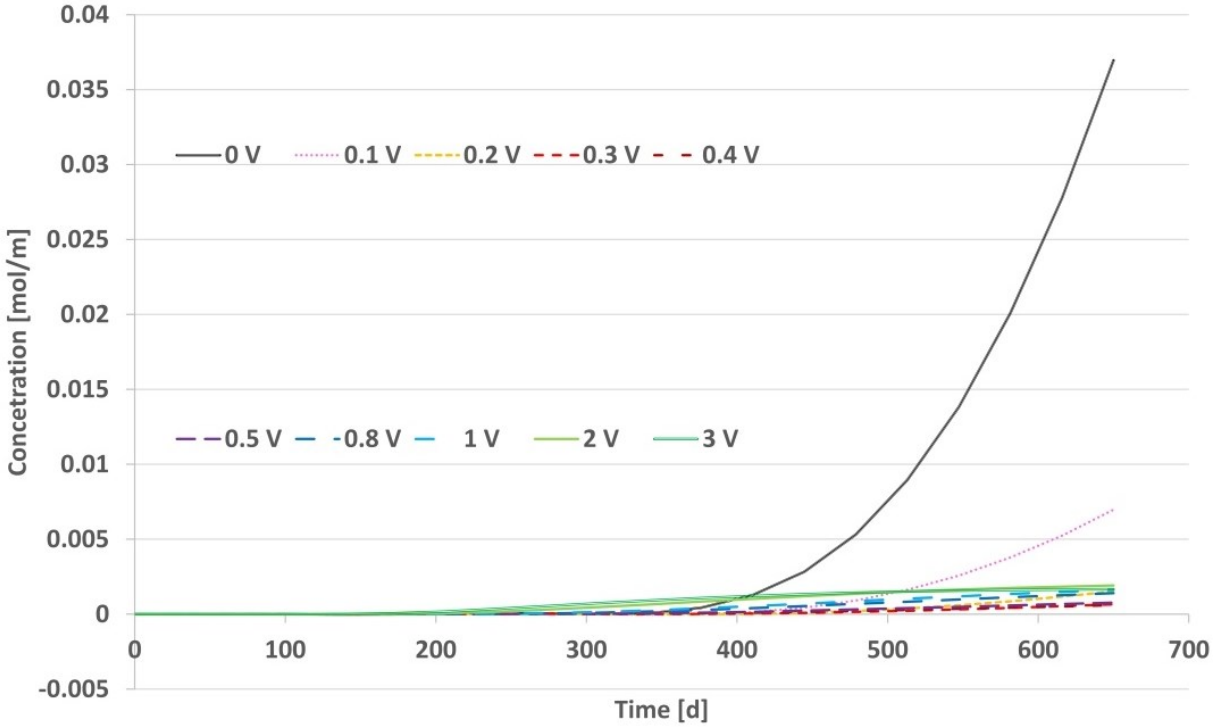

Figure 6.29. FEM solutions for the NaCl concentration over time at x = L (area III bottom)

6.2.6 Discussion – Overall Solution Comparison and Evaluation

To compare the analytical and finite differences solution approach, differences between the solution values were evaluated over time and position along the depth of the specimen by subtracting the analytical solution values from the ones from the finite differences solution. Figure 6.30 shows the differences between the concentration curves for identical parameter values, cf. Table 6.2. Only area II of the specimen was considered.

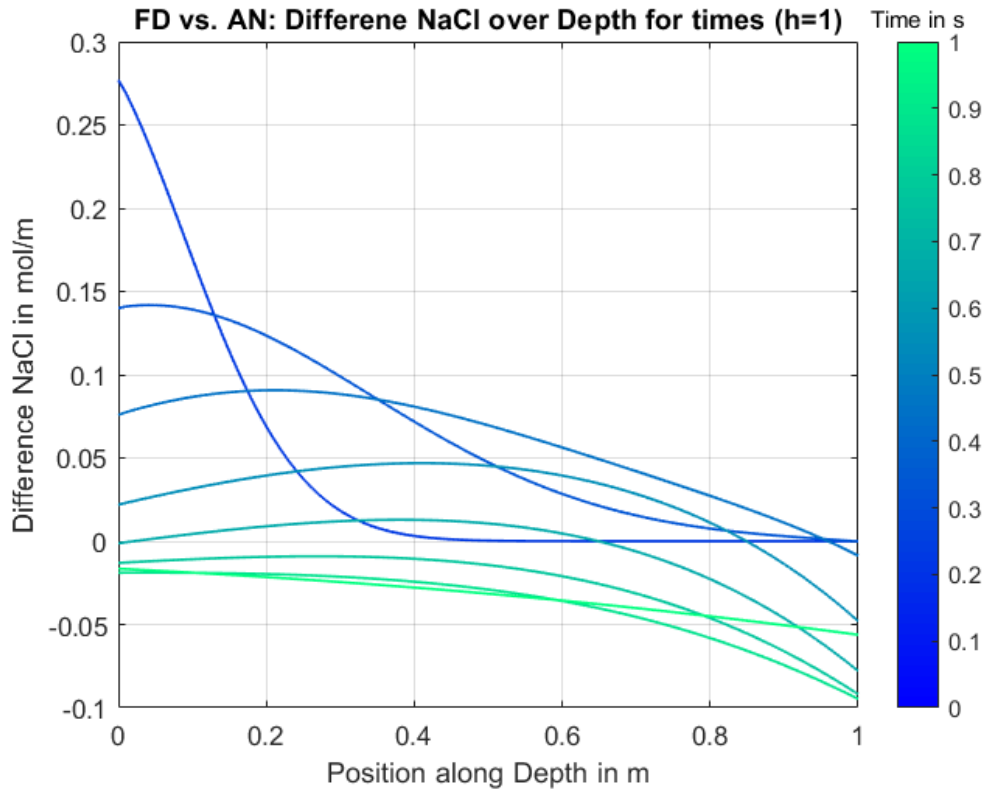

Figure 6.30. Differences between concentrations from analytical and finite differences solution

There are no significant differences, especially for later time points. Thus, it can be derived that the numerical method generally provides a very well approximated solution of the simplified 1D problem for, at least, an equally fine discretization, i.e., identical or smaller values for dt and dx, for equal or smaller fluxes.

However, during the discussion of the analytical and finite differences solution, it became apparent that the results of the analytical solution can primarily only serve for checking the validity of the solution values obtained by the implementation of the finite differences method for a specific set-up without changing migration directions over the depth of the probe. Even though it is possible with the help of the analytical solution to model migration acting against diffusion, the missing change of the migration directions and, therefore, an incorrect boundary condition at the top of the probe renders the analytical solution too simplified and thus unrealistic.

The finite differences model, by contrast, can consider changing migration directions along the depth with the correct boundary condition at the top. A fitting factor was introduced for the finite differences model, s. Eq. 6.33, to consider a weakened effect of the electrical field above the depth of the first carbon layer.

The according solutions were investigated thoroughly over position and time for different migration velocities.

The FEM solution was finally used not only to solve the simplified mathematical–physical problem in 1D but also to obtain a model as close as possible to reality, i.e., considering a multi-material 3D geometry and the exact shapes of the electrical field lines. This led to solutions showing 3D distributions of the NaCl concentrations over time. It could be seen that the application of potential differences leads to dependencies on more than one spatial dimension.

From both the finite differences and the FEM solutions, it could be seen that higher migration velocities or voltages, respectively, lead to higher concentrations in an area slightly above the first carbon layer, whereas lower concentrations appear for higher migration velocities or voltages, respectively, the more you move to the bottom of the probe, which is the intended effect of the electrochemical chloride barrier, see Figure 6.31.

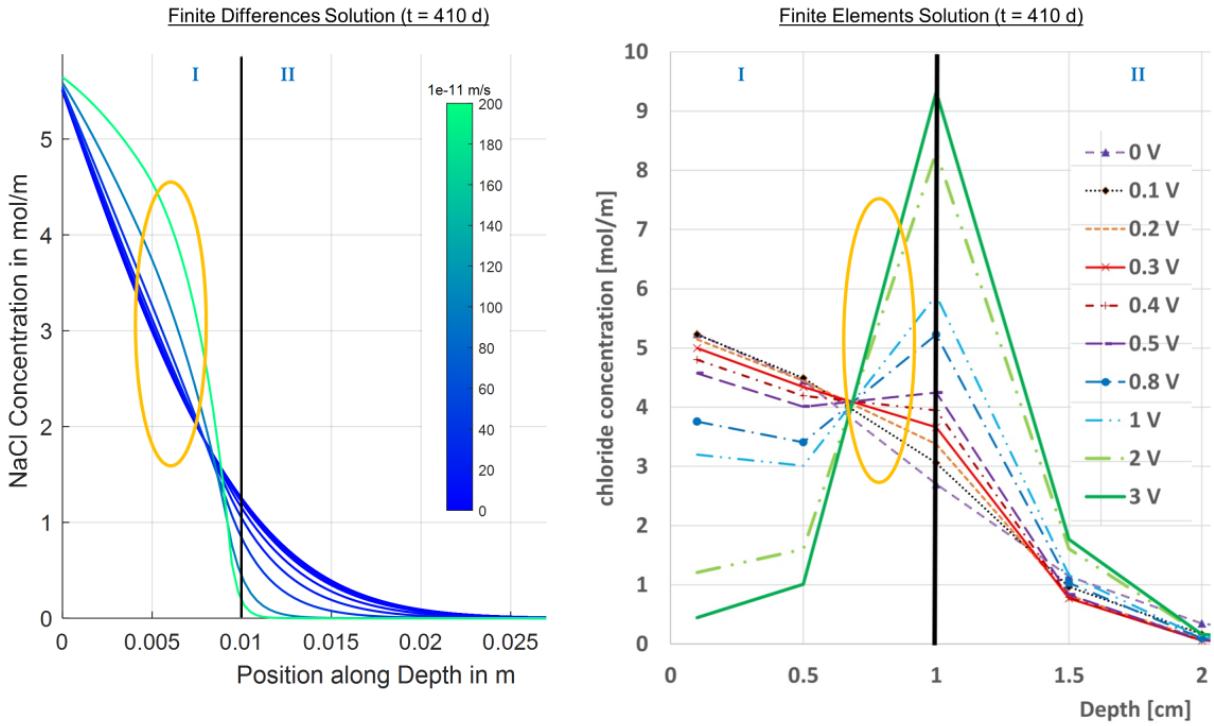

Figure 6.31. Investigated effect in the finite differences and the finite elements solution for t = 410 d

The finite differences solution did not show decreasing concentrations at the very top of the specimen for increasing voltages, in contrast to the FEM solution. Also, for the FEM solution, the curves for the higher voltages cut the curves for the lower voltages below the first carbon layer in area II, in contrast to the finite differences solution, where this takes place above the first carbon layer. The reason for that might be the mathematical limitations of the finite differences method or the underlying simplification of the mathematical-physical problem. However, the experimental investigations showed the cut below the first carbon layer in accordance with the FEM solution (Driessen-Ohlenforst & Raupach, 2021).

The unexpected effect of higher chloride concentrations for higher voltages or electrical fields of the chloride barrier, respectively, which was observed in the course of the experimental investigations, shows slightly above the first carbon layer for both the finite differences and the finite elements solution, cf. Figure 6.31 and Figure 6.32.

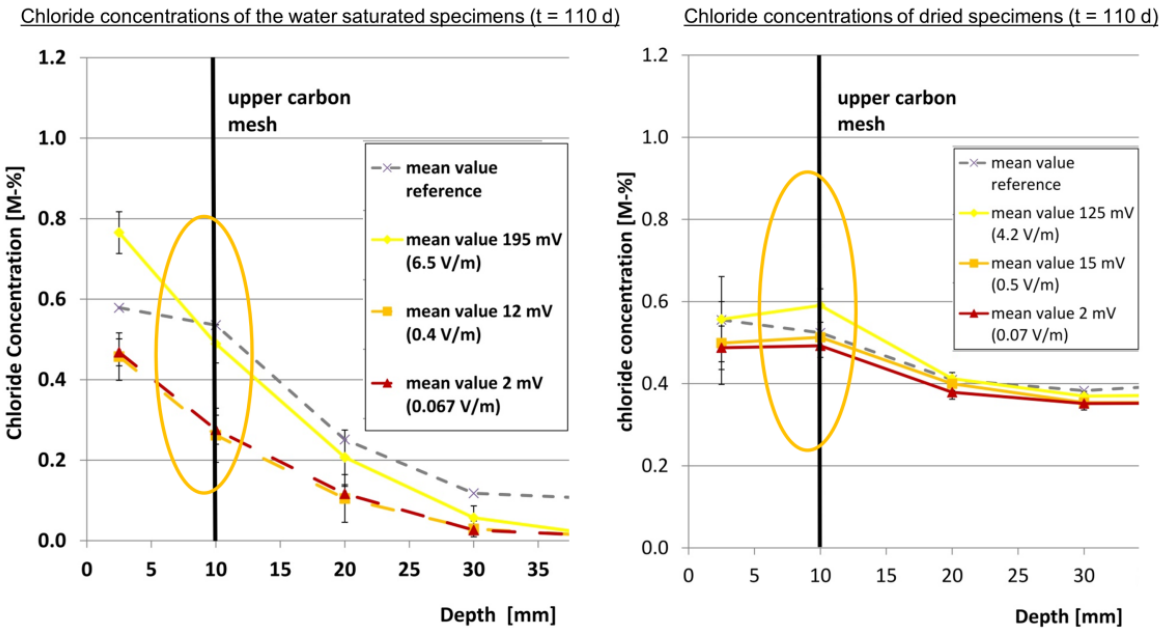

Figure 6.32. Investigated effect in the experimentally determined chloride concentration for t = 110 d

Figure 6.21 shows a local minimum occurring after a certain amount of time, i.e., the chloride concentration decreases with the migration speed up to a certain migration speed before it increases again. This explains the unexpected observation in the experimental and model-based investigations only by acting diffusion and migration.

In summary, the magnitude of the order of the chloride concentration values calculated with the finite differences and FEM solutions, as well as the aforementioned effects, are consistent with the ones observed in experimental investigations that motivated this paper.

6.2.7 Conclusions

Higher chloride concentrations for stronger electrical fields, as well as a local minimum of the chloride concentrations over the strength of the electrical field or the migration speed, respectively, were observed for one duration for certain depths in test specimens with an electrochemical chloride barrier in experiments preceding this work. (Driessen-Ohlenforst & Raupach, 2021) These effects were unexpected, could not be explained in the first place, and were, therefore, investigated in this paper analytically and numerically. The following conclusion points can be derived based upon the results discussed:

- The effects found in the experiments can be confirmed by the developed and presented finite differences model and the performed FEM simulations and are explainable solely by the acting diffusion and migration in the test specimens.
- While the performed FEM simulations modeled the chloride flow the closest to reality and revealed the weakened electrical migration above the first carbon layer, the finite differences model also showed the investigated effects above the first carbon layer.
- The effect of the local minimum is limited to positions above the depth of the first carbon layer of the test specimens. It is caused by the electrical field between the first and second carbon layer, also generating a weakened electrical migration directed into the test specimen slightly above the first carbon layer.
- According to the experimental results and the FEM simulation, higher migration velocities or stronger electrical fields, respectively, lead to lower chloride concentrations for all positions below the first carbon layer only after sufficient time duration. Therefore, the intended effect of an electrochemical chloride barrier can, in general, only be observed and confirmed after a specific time, depending on conditions and material parameters. FEM can help to approximate this change point.

7 Results and Discussion

The investigations presented in paper I-IV deal with the question under which circumstances a leakage detection based on resistivity measurement is possible with the carbon-reinforced interlayer and if an application of an electrochemical chloride barrier is possible.

Paper I focuses on the question under which boundary conditions a leakage detection is possible. Numerical simulations were carried out to quantify the effect of the leakage size, form, position, depth, and the differences in water contents between leakage area and remaining mortar on the detectability. Paper II takes a closer look at leakage detection in laboratory tests and under open weathering.

While the first papers deal with using the two carbon layers as electrodes for the leakage detection, paper III and IV investigate the case that leakage occurred, and the electrochemical chloride barrier is switched on. Here paper III deals with the laboratory investigations on the chloride barrier, and paper IV gives an analytical and numerical validation of the results found in the laboratory.

The main results are summarized in the following.

7.1 Detectability of Leakages

In the parameter study which was carried out in the course of the numerical simulations in paper I, the size of the leakage zone, resistivity of the leakage zone, resistivity of the dry mortar, depth of the leakage, the position of the leakage, number of leakages, shape of the leakage and shape of the anode were varied and their influence on the detectability calculated. It was found that the resistivity of the dry measuring field has a higher impact on the detectability of leakages than the resistivity of the leakage zone itself. The differences in the output caused by different resistivity values of the measuring fields can be recognized, while the differences between the leakage resistivities are very small. Under actual conditions, effects like fluctuations in temperature or humidity could even overlay these. This results from the fact that the regression curve of moisture content versus resistivity follows a logarithmic relationship. There is just a small spectrum in which values representing a wet condition vary, however, a large spectrum of possible values exists, representing a dry condition. Consequently, for the application on a bridge deck, it is necessary that a mortar with high resistivity values in a dry state is used and that the mortar will be given some time to dry out before a reliable detection of leakages is possible. On the other hand, even small amounts of water which permeate into the interlayer can be detected under these circumstances. The only other parameters besides the

moisture content with a considerable effect on the detectability are the leakage size and the depth. Parameters like the position of the leakage, number of leakages, shape of the leakage, and shape of the anode have a negligible impact on the detectability.
In Paper II, the leakage detection of artificially produced leakages in the laboratory could be shown. Therefore, a temperature coefficient of 4,040 K for the estimated initial saturation of the mortar could be validated as appropriate. As the temperature coefficient depends on the moisture content with the ongoing desiccation of the mortar, the appropriate coefficient will change. Furthermore, the resistivity measurement on a large-scale outdoor demonstrator could be proved, however, leakage detection on the outdoor demonstrator was not possible up to that point due to the limited desiccation of the mortar.

7.2 Electrochemical Chloride Barrier

Paper III presents the results of the extensive laboratory tests regarding the electrochemical chloride barrier. The testing program is divided into a series with water-saturated specimens where diffusion and migration are the dominant transport mechanisms and a series with completely dried specimens where convection is investigated.
For the dried series, it is observed that above the first carbon mesh, the application of the highest voltage (195 mV in the electrolyte) even leads to higher chloride concentrations than the reference. The highest investigated voltages between the two carbon meshes lead to lower chloride concentrations than the reference but still show higher chloride concentrations than the 12 mV and 2 mV specimens. Only on the bottom of the specimens, the 195 mV specimen shows the same chloride concentration as the lower voltage specimens. This indicates that in these experiments, higher voltages are not generally able to prevent chloride ingress better than lower voltages because of the higher chloride contents above the first carbon mesh. By using the electrolyte voltages, it can be shown that higher externally applied voltages lead to higher voltages in the electrolyte, and one can exclude that those higher voltages only lead to higher consumption of current at the electrodes. Although the voltages in the electrolyte and the measured currents are comparatively small, they are measurable and can work against diffusion. All in all, the results show that all investigated voltages lead to a reduction of chloride concentration compared to the reference if the effects of diffusion and migration are investigated. This observation also seems to be independent of the used anode material. A reduction of the chloride concentration by the same magnitude was achieved by using titanium meshes as a reference instead of carbon.
In Contrast, for the dried series, nearly no reduction in chloride concentration is induced by the applied electrical field. Just a small reduction in comparison to the reference at the bottom of the specimens is achieved for all voltages. It seems that the convection in the dried specimens in combination with the diffusion overweighs the effect of migration regarding the prevention

of chloride ingress. Paper III also presents the first numerical simulations to verify the laboratory results. The simulations show the same effect of higher chloride contents for the higher voltages around the upper anode. At first, between the middle of the two meshes, the applied voltages lead to lower chloride concentrations than the reference. Having a closer look at the area behind the lower carbon mesh, which is the area that should be protected against chlorides, it is shown that even the smallest applied voltages lead to a reduction in chloride concentration compared to the reference for longer testing times. The time when the chloride barrier starts to take effect depends on parameters like the exact diffusion coefficient and the electrical resistance of the mortar.
Paper IV carries on with the theoretical approach to clarify the observed effects. Therefore, an analytical solution, a numerical solution with finite differences, and a numerical solution with FEM were carried out. During the comparison of the analytical and Finite Differences solution, it got clear that the results of the analytical solution can only serve for checking the validity of the solution values obtained by the Finite Differences method for a specific set-up without changing migration directions over the depth of the probe. Even though it is possible with the help of the analytical solution to model migration acting against diffusion, the missing change of the migration directions and, therefore, an incorrect boundary condition at the top of the probe makes the analytical solution a too simplified unrealistic one.

However, the analytical solution helped to confirm the correct implementation of the Finite Differences model, which, on the contrary, can consider changing migration directions along the depth with the correct boundary condition at the top. A fitting factor was introduced for the Finite Differences model, which considers a weakened effect of the electrical field above the depth of the first carbon layer. The according solutions were investigated thoroughly over position and time for different migration velocities.

The FEM solution was finally used considering a multi-material 3D-geometry with a mesh anode and, therefore, the exact shapes of the electrical field lines. This led to solutions showing 3D-distributions of the NaCl concentrations over time. It could be seen that the application of potential differences leads to dependencies on more than one spatial dimension.

From both the Finite Differences and the FEM solutions, it could be seen that the more you move into the direction of the top of the probe, the more you will experience the effect that higher migration velocities lead to higher concentrations. In contrast, when moving into the direction of the bottom, the solutions show lower concentrations for higher migration velocities, which is the intended effect of the electrochemical chloride barrier. In between the top and the bottom, slightly above the first carbon layer, where turns, a local minimum occurs after a certain

amount of time, i.e., the chloride concentration decreases with the migration velocity up to a specific migration velocity before it increases again.
In contrast to the FEM solution, lower concentrations at the top of the specimen for higher voltages than for lower voltages leading to local maxima of the chloride concentration over depths could not be observed with Finite Differences, which is due to the mathematical limitations of the Finite Differences method.
In summary, the magnitude of order of the chloride concentration values calculated with Finite Differences and FEM and the aforementioned effects are consistent with the ones observed in experimental investigations.

Naturally, the FEM solution is less simplified and helped gain more insights, e.g., into the shapes of the electrical field lines or the dependency of the concentration distribution on the spatial dimensions. However, the Finite Differences solution is much less expensive and potentially able to be developed into a model that supports the real-time monitoring of the set-up on a bridge by continuous approximations of the concentration curve over depth and time, dependent on the current electrical field or migration velocity, respectively.

8 Conclusion and Outlook

8.1 Conclusion

As an overall result of this work, the following conclusions can be summarized:

1) The numerical simulations showed that leakages of a few percentages of the total field size are detectable with the single-layer-set-up or the standard structure of SMART-DECK. The results of the simulations were proved by Laboratory tests, and the measuring technique and data transmission was tested and installed under actual traffic conditions on a real bridge construction
2) Resistivity values of a mortar located under an intact sealer in a dry environment must be high compared to the resistivity values obtained for a water-saturated condition which means that leakages can be detected as soon as some desiccation of the mortar proceeded. If this pre-condition is fulfilled, the main impacts of various boundary conditions on the detectability of leakages were demonstrated
3) In laboratory tests, the effect of a chloride barrier with electrolyte voltages between 2 mV – 400 mV corresponding to the electrical field strength of 0.07 V/m – 13.33 V/m compared to a current-less reference was proven for water-saturated specimens regardless of the anode material. However, for completely dried specimens, the effect of the chloride barrier for these voltages in the viewed testing time of 110 days was not high enough to overweigh diffusion and convection. Therefore, it will probably not work for completely dried mortar conditions. However, on a real structure, completely dried conditions of the mortar are unlikely anyway.
4) Numerical simulations showed the same effect of an effective chloride barrier for water-saturated specimens. After a certain period, all applied voltages lead to reduced chloride concentrations below the lower carbon mesh. The effects found in the experiments can be confirmed by the developed and presented finite differences model and the performed FEM simulations and are explainable solely by the acting diffusion and migration in the test specimens. According to the experimental results and the ones from the FEM simulation, higher migration velocities or stronger electrical fields, respectively, lead to lower chloride concentrations for all positions below the first carbon layer only after sufficient time duration. Therefore, the intended effect of an electrochemical chloride barrier can, in general, only be observed and confirmed after a specific time, depending on conditions and material parameters. FEM can help to approximate this change point.

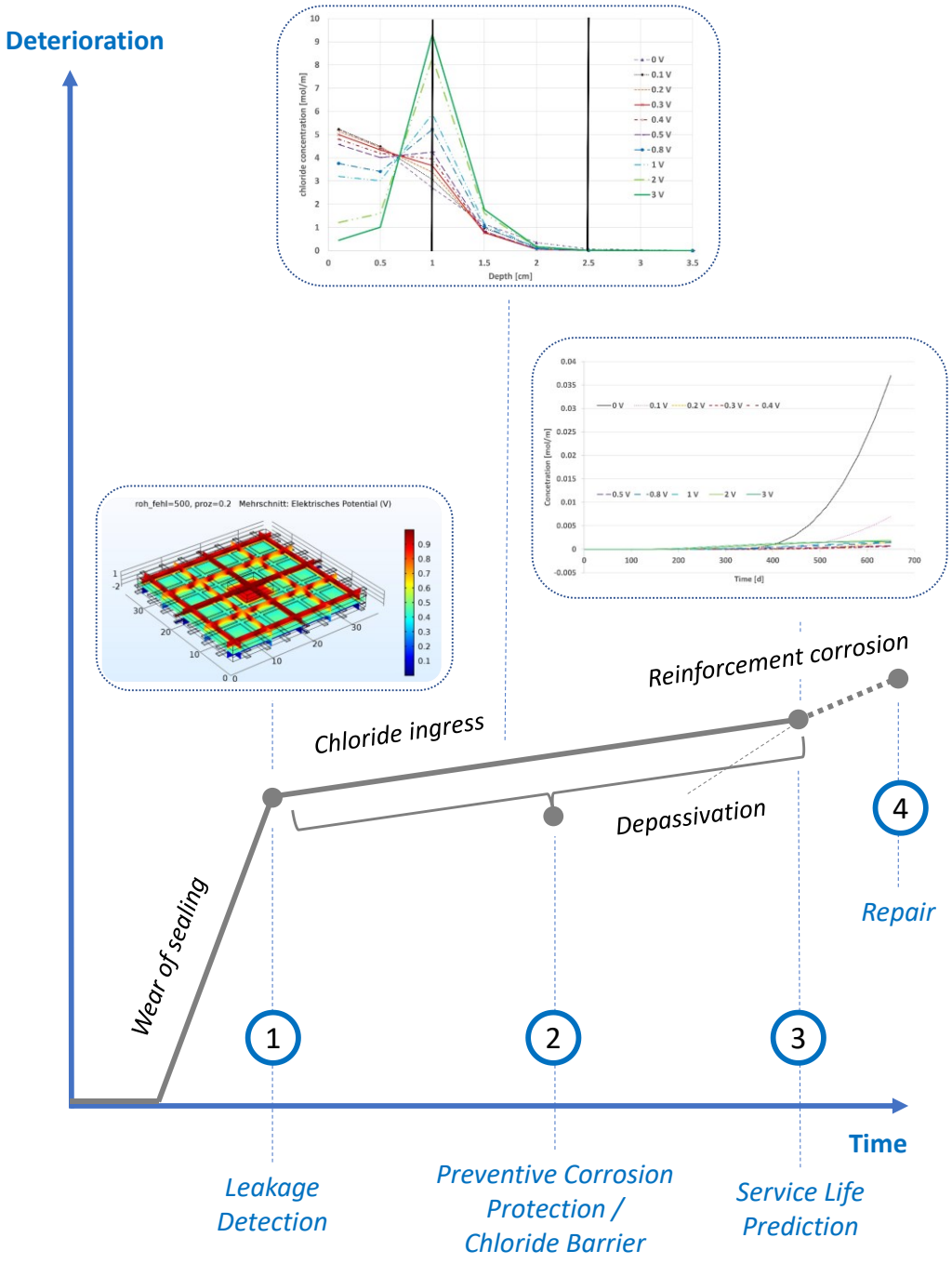

1 *Leakages can be detected.*

2 *Preventive Corrosion Protection / low field strenghts chloride barrier works.*

3 *After sufficient time higher field strengths always lead to less chlorides.*

4 *Chloride ingress can be extrapolated and predicted to optimize repair.*

Figure 8.1: Summary overview of the research results and procedure

8.2 Outlook

An influential parameter in all models is the diffusion coefficient regarding the electrochemical chloride barrier. Therefore, it would be rational to carry out all simulations with a range of common diffusion coefficients to estimate the susceptibility to errors of the models referring to the diffusion coefficient. To apply the electrochemical chloride barrier on real structures, it could be necessary first to investigate the respective diffusion coefficient of the present mortar or concrete. This could also be the first challenge to use the model for an individual adjustment of preventive cathodic protection measures. To meet this challenge, a parameter study with the other main parameters, such as the water content of the mortar, should be carried out. By now, in laboratory tests, only completely dried specimens or completely water-saturated specimens were tested. It would be reasonable to try some intermediate stages. Furthermore, the laboratory tests were already carried out over more than 100 days. To gain more experimental information on the time-dependent chloride ingress, it would be necessary to grain probes, investigate the chloride content at different times, and extend the testing time.

Concerning the leakage detection through resistivity measurements, it has to be said that the system has been applied on a bridge under real traffic since summer 2019. Over the following decades, the functionality will be constantly monitored. Because the first demonstrator had to be removed after the project period, no long-term experience over years with artificial leakages on large scale could be gained until now. To monitor the fluctuations in resistivity measurements during long-term desiccation of the mortar, large-scale specimens could be exposed to the weather over years. Therefore, an artificial leakage on each specimen should be provided but covered initially. At different times the cover could be removed, and the leakage detection could be tested.

V. References

Adam, V., Will, N., & Hegger, J. (2020). Verstärkung für Fahrbahnplatten von Massivbrücken aus Textilbeton: Versuche zur Realisierung eines Demonstrators/Strengthening of Solid Bridge Deck Slabs with Textile Reinforced Concrete: Demonstrator Tests. *Bauingenieur*, *95*(03), 85–95. https://doi.org/10.37544/0005-6650-2020-03-33

Asgharzadeh, A. (2019). Durability of polymer impregnated carbon textiles as CP anode for reinforced concrete [RWTH Aachen University]. In *Dissertation: Bd. Rheinisch-Westfälische Technische Hochschule Aachen* (S. pages 1 Online-Ressource). https://doi.org/10.18154/RWTH-2019-05559

Asgharzadeh, A., & Raupach, M. (2019). Development of a Test Method for the Durability of Carbon Textiles Under Anodic Polarisation. In C. Andrade, J. Gulikers, & E. Marie-Victoire (Hrsg.), *Service Life and Durability of Reinforced Concrete Structures* (Bd. 17, S. 143–158). Springer International Publishing. https://doi.org/10.1007/978-3-319-90236-4_11

Atkins, P. W., & De Paula, J. (Hrsg.). (2013). *Physikalische Chemie. Hauptbd.* (5. Aufl). Wiley-VCH.

Baeckmann, W., Schwenk, W., & Prinz, W. (1997). *Handbook of cathodic corrosion protection*. Elsevier Engineering Information, Incorporated.

Bastian, W. C., & Lapidus, L. (1956). Longitudinal Diffusion In Ion Exchange And Chromatographic Columns. Finite Column. *The Journal of Physical Chemistry*, *60*(6), 816–817. https://doi.org/10.1021/j150540a038

Bastidas-Arteaga, E., Chateauneuf, A., Sánchez-Silva, M., Bressolette, Ph., & Schoefs, F. (2011). A comprehensive probabilistic model of chloride ingress in unsaturated concrete. *Engineering Structures*, *33*(3), 720–730. https://doi.org/10.1016/j.engstruct.2010.11.008

Bertolini, L., Bolzoni, F., Gastaldi, M., Pastore, T., Pedeferri, P., & Redaelli, E. (2009). Effects of cathodic prevention on the chloride threshold for steel corrosion in concrete. *Electrochimica Acta*, *54*(5), 1452–1463. https://doi.org/10.1016/j.electacta.2008.09.033

Bertolini, L., Bolzoni, F., Pastore, T., & Pedeferri, P. (2004). Effectiveness of a conductive cementitious mortar anode for cathodic protection of steel in concrete. *Cement and Concrete Research*, *34*(4), 681–694.

Bertolini, L., Bolzoni, F., Pedeferri, P., Lazzari, L., & Pastore, T. (1998). Cathodic protection and cathodic prevention in concrete: Principles and applications. *Journal of applied Electrochemistry*, *28*(12), 1321–1331.

Bertolini, L., Elsener, B., Pedeferri, P., Redaelli, E., & Polder, R. (Hrsg.). (2013). *Corrosion of steel in concrete: Prevention, diagnosis, repair* (2., completely rev. and enlarged Ed). Wiley-VCH.

Brameshuber, W., Hinzen, M., Dubey, A., Peled, A., Mobasher, B., Bentur, A., Aldea, C., Silva, F., Hegger, J., & Gries, T. (2016). Recommendation of RILEM TC 232-TDT: test methods and design of textile reinforced concrete: Uniaxial tensile test: Test method to determine the load bearing behavior of tensile specimens made of textile reinforced concrete. *Materials and Structures/Materiaux et Constructions*, *49*(12), 4923–4927.

Brameshuber, W., Raupach, M., Schröder, P., & Dauberschmidt, C. (2003). Non-destructive determination of the water-content in the concrete cover using the multiring-electrode. *International Symposium (NDT-CE 2003) Non-Destructive Testing in Civil Engineering*.

Brown, M. C. (2002). *Corrosion protection service life of epoxy coated reinforcing steel in Virginia bridge decks*. Virginia Polytechnic Institute and State University.

Bruns, M., & Raupach, M. (2009). Kathodischer Korrosionsschutz am Eider-Sperrwerk als Barriere gegen Makroelementkorrosion / Cathodic Protection at the Eider-Flood Barrage as Barrier against Macrocell Corrosion. *Restoration of Buildings and Monuments*, *15*(5), 355–366. https://doi.org/10.1515/rbm-2009-6320

Bu, Y., Luo, D., & Weiss, J. (2014). Using Fick's Second Law and Nernst–Planck Approach in Prediction of Chloride Ingress in Concrete Materials. *Advances in Civil Engineering Materials*, *3*(1), 20140018. https://doi.org/10.1520/ACEM20140018

Bürchler, D. (1996). *Der elektrische Widerstand von zementösen Werkstoffen: Modell, Einflussgrössen und Bedeutung für die Dauerhaftigkeit von Stahlbeton* [ETH Zurich; Application/pdf,VI, 142 S.]. https://doi.org/10.3929/ETHZ-A-001687223

Büttner, T. (2020). SMART-DECK: Vom Konzept zum Demonstrator. *Bautechnik*, *97*(1), 48–56. https://doi.org/10.1002/bate.201900090

Cady, P. D., & Weyers, R. E. (1983). Chloride penetration and the deterioration of concrete bridge decks. *Cement, concrete and aggregates*, *5*(2), 81–87.

Carslaw, H. S., & Jaeger, J. C. (1959). *Conduction of heat in solids*. Clarendon Press,.

Chang, B.-Y., & Park, S.-M. (2010). Electrochemical Impedance Spectroscopy. *Annual Review of Analytical Chemistry*, *3*(1), 207–229. https://doi.org/10.1146/annurev.anchem.012809.102211

Cheaitani, A., & Laurila, T. (2012). Latest Trends In Corrosion Control For New Reinforced Concrete Structures And a New Concept For Intelligent Structures. *CORROSION 2012*.

Chen, X., Fu, F., Wang, H., Liang, Q., Yu, A., Qian, K., & Chen, P. (2021). A multi-phase mesoscopic simulation model for the long-term chloride ingress and electrochemical chloride extraction. *Construction and Building Materials*, *270*, 121826. https://doi.org/10.1016/j.conbuildmat.2020.121826

Chini, M. (2010). *Pan-based carbon fiber as anode material in cathodic protection systems for concrete structures*.

Chini, M., Antonsen, R., Vennesland, Ø., Mork, J. H., & Arntsen, B. (2008). Polarization behavior of carbon fiber as an anodic material in cathodic protection. *11th International Conference on Durability of Building Materials and Components, Istanbul*.

Ciucci, F. (2019). Modeling electrochemical impedance spectroscopy. *Current Opinion in Electrochemistry*, *13*, 132–139. https://doi.org/10.1016/j.coelec.2018.12.003

COMSOL - Software for Multiphysics Simulation. (o. J.). Abgerufen 21. November 2021, von https://www.comsol.com/

Danckwerts, P. V. (1995). Continuous flow systems. Distribution of residence times. *Chemical Engineering Science*, *50*(24), 3857–3866. https://doi.org/10.1016/0009-2509(96)81811-2

de Almeida Souza, Luan. R., de Medeiros, M. H. F., Pereira, E., & Capraro, A. P. B. (2017). Electrochemical chloride extraction: Efficiency and impact on concrete containing 1% of NaCl. *Construction and Building Materials*, *145*, 435–444. https://doi.org/10.1016/j.conbuildmat.2017.04.010

Deutscher Ausschuss für Stahlbeton e. V. (2015). Kritischer korrosionsauslösender Chloridgehalt: Positionspapier des DAfStb zum aktuellen Stand der Technik. *Beton- und Stahlbetonbau*, *110*(11), 784–786. https://doi.org/10.1002/best.201500508

DIN EN ISO 12696:2017-05, Kathodischer Korrosionsschutz von Stahl in Beton (ISO_12696:2016); Deutsche Fassung EN_ISO_12696:2016. (o. J.). Beuth Verlag GmbH. https://doi.org/10.31030/2610374

Doubova, A., González-Burgos, M., Guillén-González, F., & Marín Beltrán, M. (Hrsg.). (2018). *Recent Advances in PDEs: Analysis, Numerics and Control: In Honor of Prof. Fernández-Cara's 60th Birthday* (1st ed. 2018). Springer International Publishing : Imprint: Springer. https://doi.org/10.1007/978-3-319-97613-6

Driessen, C., & Raupach, M. (2015a, September 6). Corrosion Protection of Bridges Using a Textile Reinforced Concrete Interlayer: Korrosions-schutz von Brücken durch Zwischenschicht aus Textilbeton. *EUROCORR 2015*. European Corrosion Congress, Graz, Austria.

Driessen, C., & Raupach, M. (2015b). Intelligent, multifunctional textile reinforced concrete interlayer for bridges. In F. Dehn, H.-D. Beushausen, M. G. Alexander, & P. Moyo (Hrsg.), *Concrete Repair, Rehabilitation and Retrofitting IV* (1. Aufl., S. 117–117). CRC Press. https://doi.org/10.1201/b18972-75

Driessen, C., & Raupach, M. (2016). Smart-Deck: All-over realtime humidity-monitoring and preventive cathodic corrosion protection. In *Maintenance, Monitoring, Safety, Risk and Resilience of Bridges and Bridge Networks* (S. 603–603). CRC Press.

Driessen, C., & Raupach, M. (2019). Numerical Simulations for the Detection of Leakages in Bridge Deck Membranes Through Resistivity Measurements. In *Service Life and Durability of Reinforced Concrete Structures* (S. 57–69). Springer.

Driessen-Ohlenforst, C., Faulhaber, A., & Raupach, M. (2020). SMART-DECK: Monitoring des Feuchtegehaltes und kathodischer Korrosionsschutz des Bewehrungsstahles in Brückenfahrbahnen durch Zwischenschicht aus Textilbeton/SMART-DECK: Monitoring and Cathodic Protection of steel in bridge constructions with textile reinforced concrete interlayer. *Bauingenieur*, *95*(03), 96–104. https://doi.org/10.37544/0005-6650-2020-03-44

Driessen-Ohlenforst, C., & Raupach, M. (2021). Application of electrical fields to reduce chloride ingress into concrete structures [accepted for publication]. *Magazine of Concrete Research*.

Eichler, T., & Gieler-Breßmer, S. (2018). Kathodischer Korrosionsschutz im Stahlbetonbau. *Beton Kalender 2019: Parkbauten Geotechnik und Eurocode 7*, *108*, 863–904.

Eichler, T., Isecke, B., Wilsch, G., Goldschmidt, S., & Bruns, M. (2010). Investigations on the chloride migration in consequence of cathodic polarisation. *Materials and corrosion*, *61*(6), 512–517.

Elkey, W., & Sellevold, E. J. (1995). Electrical resistivity of concrete, norwegian road research laboratory. *Publ ication*.

Fajardo, G., Escadeillas, G., & Arliguie, G. (2006). Electrochemical chloride extraction (ECE) from steel-reinforced concrete specimens contaminated by “artificial” sea-water. *Corrosion Science*, *48*(1), 110–125. https://doi.org/10.1016/j.corsci.2004.11.015

Harnisch, J. (2003). *Untersuchungen zum nachträglichen Einbau von Multiring-Elektroden in Beton: Investigations on Subsequently Embedded Multi-Ring-Electrodes in Concrete*. Diplomarbeit, Institut für Bauforschung der TH Aachen (unveröffentlicht). 84 ….

Hegger, J., & Voss, S. (2008). Investigations on the bearing behaviour and application potential of textile reinforced concrete. *Engineering Structures*, *30*(7), 2050–2056. https://doi.org/10.1016/j.engstruct.2008.01.006

Helm, C. (2021, Juli 13). *Überwachung des Korrosionszustandes der Bewehrung an einem Kühlturm im Meerwasserbe-trieb mittels polymerer Zulagekathoden*. 7. Kolloquium Erhaltung von Bauwerken. Fachtagung zur Beurteilung, Instandhaltung und In-standsetzung von Bauwerken, Technische Akademie Esslingen.

Herbrand, M., Adam, V., Classen, M., Kueres, D., & Hegger, J. (2017). Strengthening of Existing Bridge Structures for Shear and Bending with Carbon Textile-Reinforced Mortar. *Materials*, *10*(9), 1099. https://doi.org/10.3390/ma10091099

Huang, V. M., Wu, S.-L., Orazem, M. E., Pébère, N., Tribollet, B., & Vivier, V. (2011). Local electrochemical impedance spectroscopy: A review and some recent developments. *Electrochimica Acta*, *56*(23), 8048–8057.

Ihekwaba, N. M., Hope, B. B., & Hansson, C. M. (1996). Carbonation and electrochemical chloride extraction from concrete. *Cement and Concrete Research*, *26*(7), 1095–1107. https://doi.org/10.1016/0008-8846(96)00076-2

Jackson, J. D., Müller, K., Witte, C., Jackson, J. D., Mueller, K., & Witte, C. (2006). *Klassische Elektrodynamik* (4., überarb. Aufl). de Gruyter.

Jensen, O. M., Hansen, P. F., Coats, A. M., & Glasser, F. P. (1999). Chloride ingress in cement paste and mortar. *Cement and Concrete Research*, *29*(9), 1497–1504. https://doi.org/10.1016/S0008-8846(99)00131-3

Kaesche, H. (o. J.). *Die Korrosion der Metalle: Physikalisch-chemische Prinzipien und aktuelle Probleme* (3., neubearb. und erw. Aufl., Nachdr. in veränd. Ausstattung).

Kaufman, J. G. (2000). *Electrical and magnetic properties of metals*. ASM International.

Kosalla, M. (2018). *Critical chloride content of reinforcing steel in concrete: Influence of anodic polarization, steel/concrete interface quality and sampling accuracy* [Online].

Krey, U., & Owen, A. (2007). *Basic theoretical physics: A concise overview* (1st ed). Springer.

Kulas, C. (2013). *Zum Tragverhalten getränkter textiler Bewehrungselemente für Betonbauteile*. IMB.

Lambert, P., Van Nguyen, C., Mangat, P. S., O'Flaherty, F. J., & Jones, G. (2015). Dual function carbon fibre fabric strengthening and impressed current cathodic protection (ICCP)

anode for reinforced concrete structures. *Materials and Structures*, *48*(7), 2157–2167. https://doi.org/10.1617/s11527-014-0300-0

Lehner, G. 1931-. (2006). *Elektromagnetische Feldtheorie für Ingenieure und Physiker* (5. Aufl.). Springer.

Li, G. (2020). *Introduction to the finite element method and implementation with MATLAB*. Cambridge University Press.

Liu, H., Zhang, B., Liu, H., & Ji, Z. (2021). Analysis of Long-Term Durability Monitoring Data of High-Piled Wharf with Anode-Ladder Sensors Embedded in Concrete. *Frontiers in Materials*, *8*, 703347. https://doi.org/10.3389/fmats.2021.703347

Logan, S. R. (1982). The origin and status of the Arrhenius equation. *Journal of Chemical Education*, *59*(4), 279.

Luping, T., & Nilsson, L.-O. (1993). Rapid determination of the chloride diffusivity in concrete by applying an electric field. *Materials Journal*, *89*(1), 49–53.

Luping, T., Nilsson, L.-O., & Basheer, M. (2012). *Resistance of concrete to chloride ingress: Testing and modelling*. Taylor and Francis.

Martın-Pérez, B. (1999). *Service life modelling of RC higway structures exposed to chlorides*. PhD thesis, university of Toronto.

Meister, A., & Sonar, T. (2019). *Numerik: Eine lebendige und gut verständliche Einführung mit vielen Beispielen*. Springer Spektrum. https://doi.org/10.1007/978-3-662-58358-6

Miranda, J. M., Cobo, A., Otero, E., & González, J. A. (2007). Limitations and advantages of electrochemical chloride removal in corroded reinforced concrete structures. *Cement and Concrete Research*, *37*(4), 596–603. https://doi.org/10.1016/j.cemconres.2007.01.005

Mohsen, M. F. N., & Baluch, M. H. (1983). An analytical solution of the diffusion-convection equation over a finite domain. *Applied mathematical modelling*, *7*(4), 285–287.

Morales Cruz, C., Gohil, U., Quadflieg, T., Raupach, M., & Gries, T. (2015). Improving the bond behavior of textile reinforcement and mortar through surface modification. *3rd ICTR*

International Conference on Textile Reinforced Concrete Brameshuber, W.(ed.) Aachen, Germany, 215–223.

Müller, R. O., & Holtzhauer, K. (1992). *Kathodischer Korrosionsschutz von Bewehrungsstählen: Langzeitbeständigkeit von Anodenmaterialien und Mörteln; Schlußbericht; Forschungsauftrag Nr. 88/89 [auf Antrag der Arbeitsgruppe Brückenunterhaltungsforschung]*. ASB.

Nguyen, H. Y. T., Pansuk, W., & Sancharoen, P. (2018). The Effects of Electro-Chemical Chloride Extraction on the Migration of Ions and the Corrosion State of Embedded Steel in Reinforced Concrete. *KSCE Journal of Civil Engineering*, *22*(8), 2942–2950. https://doi.org/10.1007/s12205-017-2022-7

Nguyen, P. T., Bastidas-Arteaga, E., Amiri, O., & El Soueidy, C.-P. (2017). An Efficient Chloride Ingress Model for Long-Term Lifetime Assessment of Reinforced Concrete Structures Under Realistic Climate and Exposure Conditions. *International Journal of Concrete Structures and Materials*, *11*(2), 199–213. https://doi.org/10.1007/s40069-017-0185-8

Nikonenko, V. V., Lebedev, K. A., & Suleimanov, S. S. (2009). Influence of the convective term in the Nernst-Planck equation on properties of ion transport through a layer of solution or membrane. *Russian Journal of Electrochemistry*, *45*(2), 160–169.

Nilsson, L.-O. (2006). Present limitations of models for predicting chloride ingress into reinforced concrete structures. *Journal de Physique IV (Proceedings)*, *136*, 123–130. https://doi.org/10.1051/jp4:2006136013

Osterminski, K., Polder, R. B., & Schießl, P. (2012). Long term behaviour of the resistivity of concrete. *Heron*, *57*(3), S. 211.

Pedeferri, P. (1996). Cathodic protection and cathodic prevention. *Construction and Building Materials*, *10*(5), 391–402. https://doi.org/10.1016/0950-0618(95)00017-8

Peled, A., Mobasher, B., & Bentur, A. (2017). *Textile Reinforced Concrete* (1. Aufl.). CRC Press. https://doi.org/10.1201/9781315119151

Pepper, D. W., & Heinrich, J. C. (2017). *The finite element method: Basic concepts and applications with MATLAB, MAPLE, and COMSOL* (Third edition). CRC Press, Taylor & Francis Group, CRC Press is an imprint of the Taylor & Francis Group, an informa business.

Polder, R. B. (2001). Test methods for on site measurement of resistivity of concrete—A RILEM TC-154 technical recommendation. *Construction and building materials*, *15*(2–3), 125–131.

Polder, R., Pan, Y., Courage, W., & Peelen, W. H. (2016). Preliminary study of life cycle cost of preventive measures and repair options for corrosion in concrete infrastructurecorrosion in concrete infrastructure. *Heron*, *61*(1), 1–13.

Poursaee, A. (2016). Corrosion of steel in concrete structures. In *Corrosion of Steel in Concrete Structures* (S. 19–33). Elsevier. https://doi.org/10.1016/B978-1-78242-381-2.00002-X

Raupach, M. (1992). Zur chloridinduzierten Makroelementkorrosion von Stahl in Beton. *Deutscher Ausschuss für Stahlbeton*, *433*.

Raupach, M. (2005). Concrete Repair According to the New European Standard EN 1504. *Proceedings of the International Conference on Concrete Repair, Rehabilitation and Retrofit-ting (ICCRRR)*, 6–8.

Raupach, M., Dauberschmidt, C., & Warkus, J. (2003a). Bestimmung der Feuchteverteilung in zementösen Baustoffen mit Einbausensoren; Soil Moisture Group der Universität Karlsruhe. *Innovative Feuchtemessung in Forschung und Praxis, Bauwesen-Geotechnik-Umwelttechnik; Kolloquium mit Workshop*.

Raupach, M., Dauberschmidt, C., & Warkus, J. (2003b, Juli 3). *Indirekte Bestimmung der Feuchteverteilung in zementösen Baustoffen durch Elektrolytwider-standsmessungen*. Kolloquium mit Workshop Innovative Feuchtemessung in Forschung und Praxis, Karlsruhe.

Raupach, M., Dauberschmidt, C., & Wolff, L. (2006). Monitoring the moisture distribution in concrete structures. *Proceedings of the International Conference on Concrete Repair, Rehabilitation and Retrofitting (ICCRRR), Cape Town, South Africa*, 21–23.

Raupach, M., Dauberschmidt, C., Wolff, L., & Harnisch, J. (2007). Monitoring der Feuchteverteilung in Beton. *BETON-DUSSELDORF-*, *57*(1/2), 20.

Raupach, M., Gulikers, J., & Reichling, K. (2013). Condition survey with embedded sensors regarding reinforcement corrosion. *Materials and Corrosion*, *64*(2), 141–146. https://doi.org/10.1002/maco.201206629

Raupach, M., Klinghoffer, O., & Helm, C. (2016, September 11). Integrated Corrosion Monitoring Systems for Steel in Concrete—Concepts and Actual Developments. *EUROCORR 2016*. European Corrosion Congress, Advances in Linking Science to Engineering, Montpellier, France.

Raupach, M., & Schießl, P. (2003). The Expansion-Ring-System for Monitoring the Risk of Reinforcement Corrosion. *Durability Design and Fracture Mechanics of Concrete Structures, Proceedings of the Interna-tional Conference, Construction and Architecture*, 36–37.

Reichling, K., & DAfStb. (2015). *Bestimmung und Bewertung des elektrischen Widerstands von Beton mit geophysikalischen Verfahren*. Beuth Berlin.

Reichling, K., Weichold, O., & Raupach, M. (2012). Was verrät uns der elektrische Widerstand über den Beton? *Restoration of Buildings and Monuments*, *18*(5), 265–274. https://doi.org/10.1515/rbm-2012-6539

Schießl, P., & Raupach, M. (1993). Monitoring of the Corrosion Risk for the Reinforcement at the Bridge Schießbergstraße in Germany. *Journal of Structural Engineering*, *1*, 23–27.

Schießl, R., & Raupach, M. (1999). Zerstörungsfreie permanente Überwachung der Korrosionsgefahr für die Bewehrung von Stahlbetonbauwerken-Sensorsysteme für direkten und nachträglichen Einbau. Berlin: Deutsche Gesellschaft für Zerstörungsfreie Prüfung, 1999. *Bauwerksdiagnose, Praktische Anwendungen zerstörungsfreier Prüfungen, München*, *21*, 22.

Stratfull, R. F. (1957). The Corrosion of Steel In a Reinforced Concrete Bridge. *CORROSION*, *13*(3), 43–48. https://doi.org/10.5006/0010-9312-13.3.43

Stratfull, R. F. (1974). Experimental cathodic protection of a bridge deck. *Transportation Research Record*, *500*, 1–15.

Tang, L. (1996). Chloride transport in concrete-measurement and prediction. *Chalmers University of Technology, Sweden, Doctor Thesis*.

Tang, L., & Nilsson, L. O. (1997). Accelerated tests for chloride diffusivity and their application in prediction of chloride penetration. *Mechanisms of Chemical Degradation of Cement-based Systems*, 387–396.

Tissier, Y., Bouteiller, V., Marie-Victoire, E., Joiret, S., Chaussadent, T., & Tong, Y. (2019). Electrochemical chloride extraction to repair combined carbonated and chloride contaminated reinforced concrete. *Electrochimica Acta*, *317*, 486–493. https://doi.org/10.1016/j.electacta.2019.05.165

Torres-Luque, M., Bastidas-Arteaga, E., Schoefs, F., Sánchez-Silva, M., & Osma, J. F. (2014). Non-destructive methods for measuring chloride ingress into concrete: State-of-the-art and future challenges. *Construction and Building Materials*, *68*, 68–81. https://doi.org/10.1016/j.conbuildmat.2014.06.009

Tritthart, J., & Baumgartner, E. (2007). Zerstörungsfreie Korrosionsschutzmaßnahmen. *SCHRIFTENREIHE STRASSENFORSCHUNG*, *571*.

Wang, Y., Li, L., & Page, C. L. (2005). Modelling of chloride ingress into concrete from a saline environment. *Building and Environment*, *40*(12), 1573–1582. https://doi.org/10.1016/j.buildenv.2005.02.001

Warkus, J., & Raupach, M. (2010). Modelling of reinforcement corrosion–geometrical effects on macrocell corrosion. *Materials and corrosion*, *61*(6), 494–504.

Warkus, J., Raupach, M., & Gulikers, J. (2006). Numerical modelling of corrosion – Theoretical backgrounds –. *Materials and Corrosion*, *57*(8), 614–617. https://doi.org/10.1002/maco.200603992

Wei, L.-L., Zhu, J.-H., Ueda, T., Su, M.-N., Liu, J., Liu, W., Tang, L.-P., & Xing, F. (2020). Tensile behaviour of carbon fabric reinforced cementitious matrix composites as both strengthening and anode materials. *Composite Structures*, *234*, 111675. https://doi.org/10.1016/j.compstruct.2019.111675

Xu, J., & Li, F. (2019). Numerical analysis on efficiency of electrochemical chloride extraction of one side anode in concrete. *Ocean Engineering*, *179*, 38–50. https://doi.org/10.1016/j.oceaneng.2019.03.018

Xu, J., Peng, C., Wang, G., & Wang, P. (2021). A multi-phase scale simulation of electrochemical chloride extraction in crack-self-healing concrete. *Structural Concrete*, suco.202000723. https://doi.org/10.1002/suco.202000723

Zeng, L., & Song, R. (2013). Controlling chloride ions diffusion in concrete. *Scientific Reports*, *3*(1), 3359. https://doi.org/10.1038/srep03359

Zhang, E. Q., & Tang, L. (2019). Application of CFRP as anode in cathodic protection for steel reinforced concrete – a review. *MATEC Web of Conferences*, *289*, 03007. https://doi.org/10.1051/matecconf/201928903007

Zimmermann, L. (2000). *Korrosionsinitiierender Chloridgehalt von Stahl in Beton*. ETH Zurich.